University of New Mexico
UNM Digital Repository

Summer 7-14-2017

Graphite and Graphene-Oxide based PGM-free model catalysts for the Oxygen Reduction Reaction

Joseph Henry Dumont
University of New Mexico

Follow this and additional works at: https://digitalrepository.unm.edu/nsms_etds

Part of the Catalysis and Reaction Engineering Commons, Nanoscience and Nanotechnology Commons, and the Other Materials Science and Engineering Commons

Joseph H. Dumont

Candidate

Nano Science and Microsystems Engineering

Department

This thesis is approved, and it is acceptable in quality and form for publication:

Approved by the Thesis Committee:

Plamen Atanassov , Chairperson

Kateryna Artyushkova

Fernando Garzon

Gautam Gupta

GRAPHITE AND GRAPHENE OXIDE BASED
PGM-FREE MODEL CATALYSTS
FOR THE OXYGEN REDUCTION REACTION

by

JOSEPH H. DUMONT

B.S., Physics/Biology,
Aix-Marseille Université, 2011

M.S., Materials for Renewable Energies,
Université de Poitiers, 2013

DISSERTATION

Submitted in Partial Fulfillment of the
Requirements for the Degree of

Doctor of Philosophy
Engineering

The University of New Mexico
Albuquerque, New Mexico

July, 2017

DEDICATION

I dedicate my dissertation to my family and friends. An immense feeling of gratitude to my loving parents, Patrick and Sylvie Dumont, whose tenacity and courage inspired me to always go further. My sister, Marie, who was always here and whose hard work will pay off very soon. I also dedicate this work in memory of my grandmother, Pierrette Donnette, and my great cousin, Anne-Marie Bouillet who never saw my graduation.

ACKNOWLEDGEMENTS

I would like to express my deep gratitude to my University of New Mexico advisor, Dr. Plamen Atanassov, as well as to my Los Alamos National Laboratory advisor, Dr. Gautam Gupta for their patient guidance, mentorship and the contributions that each of them made to my intellectual growth during my years as a graduate student.

I would like to thank the other members of my dissertation committee, Dr. Kateryna Artyushkova and Dr. Fernando Garzon, who have generously given their time and expertise to better my work. I thank them for their contribution and their good-natured support.

I must acknowledge the many friends, colleagues, students and professors as well who assisted, advised, and supported my research and writing efforts over the years. I need to thank especially Dr. Ulises Martinez who significantly contributed to my technical knowledge and offered his patience and his friendship.

I am grateful to my longtime girlfriend, Adeline Fanni for her patience, love and support throughout these years.

GRAPHITE AND GRAPHENE OXIDE BASED PGM-FREE MODEL CATALYSTS FOR THE OXYGEN REDUCTION REACTION

By

Joseph H. Dumont

**B.S., PHYSICS/BIOLOGY,
AIX-MARSEILLE UNIVERSITE, 2011**

**M.S., MATERIALS FOR RENEWABLE ENERGIES,
UNIVERSITE DE POITIERS, 2013**

**PH.D., ENGINEERING,
THE UNIVERSITY OF NEW MEXICO, 2012**

ABSTRACT

The world currently relies heavily on fossil fuels such as coal, oil, and natural gas for its energy. Fossil fuels are non-renewable, that is, they draw on finite resources that will eventually dwindle, becoming too expensive or too environmentally damaging to retrieve. One alternative source of energy are fuel cells, electrochemical devices that convert chemical energy to cleanly and efficiently produce electricity. They can be used in a wide range of applications, including transportation, stationary, portable and emergency power sources. Their development has been slowed by the high cost of PGM electrocatalysts needed at both electrodes as well as sluggish oxygen reduction reaction (ORR) occurring at the cathode. To replace the costly PGM-based materials, a new generation of PGM-free ORR catalysts has emerged, composed by earth abundant elements such as carbon, nitrogen and transition metals. Current heterogeneous PGM-free

catalysts are exceedingly difficult to study using standard analytical techniques. In the following studies, we use well- defined model systems based on graphitic systems such as graphite and graphene oxide. These extensively characterized materials are relatively simple to model, making them ideal platforms for understanding catalytic active sites.

In the first study, we investigate a green, solvent-free and sustainable synthesis route to synthesize large amounts of active ORR electrocatalysts based on graphite. We show that the simple ball milling of expanded graphite in presence of metal and nitrogen precursors followed by a pyrolysis step can create active and selective catalysts towards the ORR. We report an improved activity of graphite-based electrocatalysts in alkaline medium with an onset potential (E_{onset}) up to ~0.89 V and a half-wave potential ($E_{1/2}$) up to 0.72 V.

In the second study, we demonstrate that removal of intercalated water using simple solvent treatments causes significant structural reorganization substantially impacting the ORR activity and stability of nitrogen-doped graphitic systems (NrGO). Contrasting reports describing ORR activity of NrGO-based catalysts in alkaline electrolytes, we demonstrate superior activity in acidic electrolyte with E_{onset} of ~0.9 V, $E_{1/2}$ of 0.71 V, and selectivity for four-electron reduction >95%. Further, durability testing showed $E_{1/2}$ retention >95% in N_2- and O_2-saturated solutions after 2000 cycles demonstrating highest ORR activity and stability reported to date for NrGO-based electrocatalysts in acidic media.

In the third study, we report that the activity and selectivity (4e-) of NrGO catalysts for ORR is enhanced using simple solvent and electrochemical treatments. The

solvents, which were chosen based on Hansen's solubility parameters, drive a substantial change in the morphology of the functionalized graphene materials either by i) forming microporous holes in the graphitic sheets that lead to edge defects as well as enhanced oxygen transport, or ii) inducing 3D structure in the graphitic sheets that promote ORR. Additionally, the cycling of these catalysts has highlighted the multiplicity of the active sites, with different durability, leading to a more selective catalyst over time with little to no loss in performance. We demonstrate excellent ORR activity in an alkaline electrolyte with an E_{onset} up to ~1.08 V and a $E_{1/2}$ up to 0.84 V. Further, durability testing showed $E_{1/2}$ loss <3% in N_2- and O_2-saturated solutions after 10,000 cycles, demonstrating a high ORR activity and stability while improving the selectivity towards the 4-electron reduction.

The results described in this study will allow for the synthesis of better performing graphitic ORR electrocatalyst with controlled activity and could lead to a better understanding of the active site formation in PGM-free electrocatalysts.

LIST OF FIGURES

LIST OF TABLES

TABLE OF CONTENT

1. Introduction

1.1. Fuel cells

Fuel cells are electrochemical devices that allow the conversion of chemical energy (referred as fuel) to electrical energy. Just like batteries or a variety of electrochemical devices, fuel cells are devices in which two electrodes are in contact with an ionic conductor (electrolyte). At the anode, occurs the oxidation of the fuel that produces electrons that will then react at the cathode and reduce an oxidizing agent. In the schematics shown below (**Figure 1 A-B**), the fuel used is hydrogen (H_2) and the oxidizing agent is oxygen (O_2).
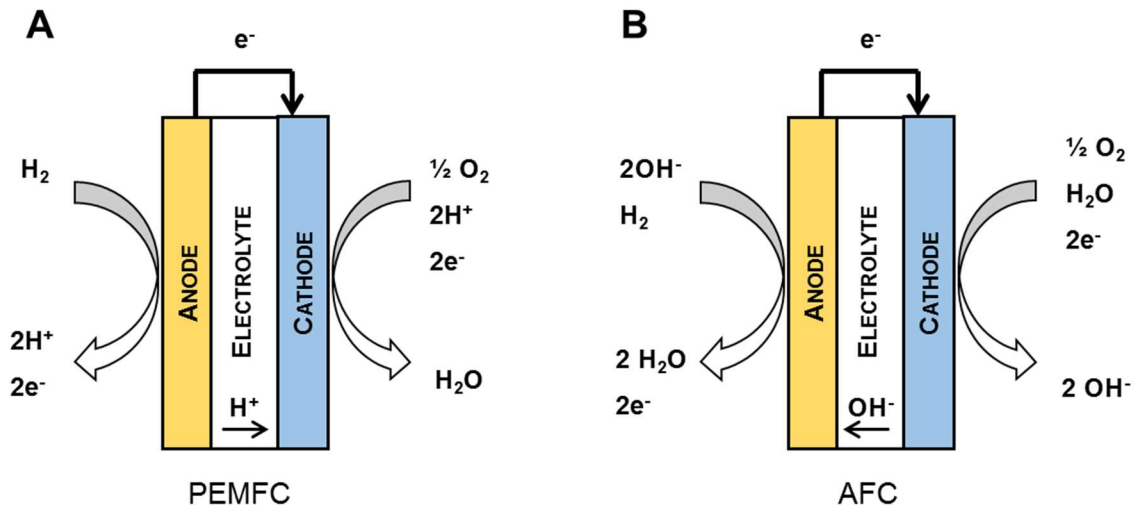
Figure 1: Schematics of a proton exchange membrane fuel cell (A), and an alkaline fuel cell (B) with corresponding anodic and cathodic reactions.

The materials presented in this study are tested in both acidic and alkaline and are meant to be used as catalysts for the oxygen reduction reaction occurring at the cathode of both proton exchange membrane fuel cells (PEMFC) and alkaline fuel cells (AFC).

PEMFCs use a thin polymer membrane as an electrolyte where protons are the charge carrier. The anode and cathode reactions in the PEMFC are described by **Equation (1)** and **(2)**, respectively:

$$Anode: \quad H_2 \rightarrow 2H^+ + 2e^- \quad\quad\quad (1)$$

$$Cathode: \quad \frac{1}{2}O_2 + 2H^+ + 2e^- \rightarrow H_2O \quad\quad\quad (2)$$
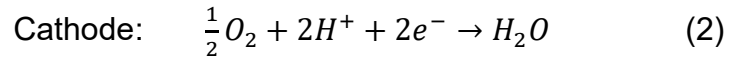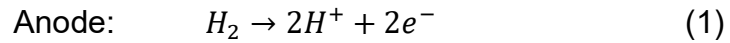
PEMFCs offer several advantages such as of the highest power densities in fuel cells, and low temperature applications (80°C) making them suitable for portable power applications. However, some of the main disadvantages are the high cost of platinum catalysts and proton exchange membranes, a sluggish oxygen reduction reaction (ORR) and the need to use pure fuels due to the sensibility to contaminants such as sulfur and carbon monoxide [1].

In contrast to PEMFCs, AFCs usually use an aqueous KOH electrolyte where the charge carrier (OH⁻) goes from the cathode to the anode. The anode and cathode reactions in the AFC are described by **Equations (3)** and **(4)**, respectively:

$$Anode: \quad H_2 + 2OH^- \rightarrow 2H_2O + 2e^- \quad\quad\quad (3)$$

$$Cathode: \quad \frac{1}{2}O_2 + 2e^- + 2H_2O \rightarrow 2OH^- \quad\quad\quad (4)$$
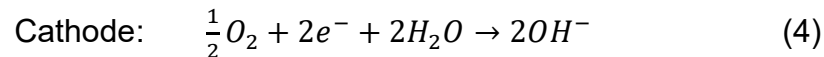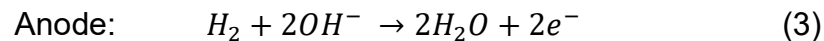
Some of the advantages of AFCs include faster ORR kinetics and an advantageous range of relatively inexpensive materials which are not only active but have been shown to perform as well or better than platinum[2, 3]. Additionally, AFCs allow the use of cheaper materials for fuel cell stacks and a wide choice of

fuel (H_2, hydrazine hydrate [4, 5], *etc.*). Some of their disadvantages include poor electrolyte stability and sensibility to CO_2 [1].

1.2. The Oxygen Reduction Reaction

The electrocatalytic reduction of oxygen in aqueous electrolytes is defined by the following equations:

Acidic	**Alkaline**	**Equation**
$O_2 + 4H^+ + 4e^- \rightarrow 2H_2O$	$O_2 + 2H_2O + 4e^- \rightarrow 4OH^-$	(5)
$O_2 + 2H^+ + 2e^- \rightarrow H_2O_2$	$O_2 + H_2O + 2e^- \rightarrow HO_2^- + OH^-$	(6)
$H_2O_2 + 2H^+ + 2e^- \rightarrow 2H_2O$	$HO_2^- + H_2O + 2e^- \rightarrow 3OH^-$	(7)
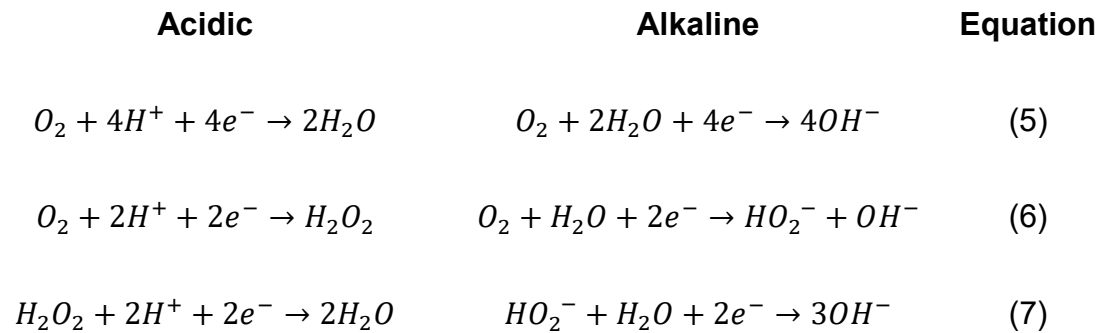
The reaction occurs ideally following the four-electron pathway described by **Equation (5)**. However, more often than not, the reduction of oxygen proceeds in parallel via two two-electron reactions defined by **Equations (6)** and **(7)**. The ORR performance of a catalyst is defined by its activity, its selectivity towards the four-electron reduction of oxygen, and, more importantly, by its half-wave potential ($E_{1/2}$), which is a descriptor of the limiting current density and onset potential (E_{onset}) of the catalyst. The thermodynamic reversible potential ($E°$) of oxygen reduction at 25°C is 1.23 V versus the reversible hydrogen electrode (RHE). Any additional potential required to drive the ORR is called the overpotential (η). High-performing ORR catalysts are characterized by low η, high E½, high selectivity values for four-electron transfer and higher limiting current.

1.3. PGM-free electrocatalysts

Platinum (Pt) based catalysts are the state-of-the-art for the ORR in terms of activity, selectivity, and durability [6]. However, PGM-free materials synthesized from earth-abundant elements via heat treatment of transition-metal (M), nitrogen (N), and carbon (C) precursors have garnered considerable interest especially in electrocatalysis as a potential replacement for costly PGM catalysts [7-10]. In that context, nitrogen-modified carbons have been more intensively investigated as heteroatom-modified carbon catalysts for the ORR than their counterparts modified with boron[11-15], fluorine[16], phosphorus [15, 17-19], and sulfur [20, 21]. M-N-C catalysts are the most promising PGM-free catalysts in acidic and alkaline electrolytes. They are traditionally prepared by pyrolysis of carbon supported, nitrogen precursors and metals salts in presence of ammonia or inert gas [22-30]. This synthesis leads to active electrocatalysts displaying very different heterogeneous morphologies

I spite of the great improvements in ORR activity that have been achieved with PGM-free catalysts, the exact nature of the active site(s) created during the heat treatment remains the subject of intense investigation in the field [2, 31-35]. To this date, it is unknown whether the transition metal participates in the active site or simply catalyzes its formation. Additionally, it is unknown how the location of the active sites e.g., in-plane, edge, subsurface influences the performance and the stability of the system. In all cases, the presence of nitrogen species embedded within the carbon structures is critical to the performance. Further advances in oxygen catalysis require a fundamental understanding of the active site structure.

This suggests that a focused, science-based effort can yield significant gains in catalyst understanding and most importantly in performance. In this project, controlled functionality of PGM-free catalysts for clean energy will be achieved through an investigation of graphene-based model systems yielding highly active, selective, and durable catalysts.

1.4. Graphite and graphene

The origin of the word graphite comes from the Greek word "*graphein*" which means to write [36]. In fact, graphite has been used to write and to draw since the beginning of history. In the 18th century, it was demonstrated that graphite was an allotrope of carbon. It's one of the most common forms of carbon that can be found in the earth's crust. It is formed by layers of sp^2 hybridized carbons arranged in a two-dimensional honeycomb structure. The interatomic bonds (σ) between sp^2 carbons are strong, which makes single layers, called graphene, resistant to chemical attacks and mechanical deformation. The interlayer bonds (π) are much weaker and allow the graphene sheets to be exfoliated, mechanically or chemically [37, 38]. Graphite has been the interest of a variety of electro-chemical applications thanks to its high purity, electrical and thermal conductivity, specific surface properties [39], and also its attractive price/performance ratio [40].

1.5. Graphene oxide

One of the many interests in developing PGM and PGM-free catalysts based on graphene and its analogs comes from its excellent electronic properties [37, 41] combined with a superior resistance to corrosion which is a problem often encountered with previously described PGM-free catalysts.

The conventional approach to synthesize resilient N-doped graphitic catalysts involve the exfoliation and functionalization of graphite using strong oxidizing agents [42-46], leading to graphene oxide (GO), a highly defective 2D structure [37, 47, 48], highly dispersible in polar solvents [49-52]. Following the synthesis, GO can be chemically [53-55] or thermally reduced at high-temperatures either in inert environment [56-58] or in an ammonia environment facilitating nitrogen incorporation [59]. Several alternatives to ammonia treatment exist, more specifically by pyrolysis and reduction of graphene oxide in presence of nitrogen-rich compounds [60-64].

1.6. Graphite intercalated compounds

GICs are a unique class of lamellar materials formed by the insertion of atomic or molecular species between the planes of graphite. Electrical, thermal and magnetic properties can be varied by intercalation of alkali metals, halogens and metal halides, making these materials interesting technologically [65-70]. GICs have been investigated for electrochemical applications in batteries or as electrodes [71]. So far, they have not been tested for the electrochemical reduction of oxygen. Their facile synthesis, the relatively simple structure and the presence of metals establish GICs as an ideal model for PGM-free catalyst.

1.7. Modelling of PGM-free catalysts

Several attempts have been made to model the behavior of PGM-free electrocatalysts for the ORR by highlighting the importance of N species bound to carbon [72], identify stable M-N-C compounds [73-77], explain the importance of the binding energy between the active sites and the reactants [78]. Additionally,

modelling studies have been conducted to elucidate the impact of the electrode structure on the ORR performance of PGM-free catalysts which is much thicker and more susceptible to water management issues [79, 80].

2. Research objectives

We propose a combined experimental and modeling approach to elucidate ORR active sites, which will be used to guide the design of highly efficient, low-cost electrocatalysts. The emphasis will be placed on N-doped graphitic systems and metal-ligand bonding structures as primary active sites. Simulation of these sites will give insight into the physicochemical processes involved in the ORR. The reaction mechanisms and active site structures will be used to design and synthesize advanced ORR catalysts with high activity, selectivity and durability.

2.1. Model catalyst systems on graphene-based supports

Current heterogeneous catalysts are exceedingly difficult to study using standard analytical techniques. We propose to use well- defined model systems based on graphitic systems such as graphite and graphene oxide. These extensively characterized materials are relatively simple to model, making them ideal platforms for understanding catalytic active sites. Different transition metals and nitrogen species will be incorporated into the graphene substrate to mimic the existing PGM-free catalysts. These model systems will enable, for the first time, direct observation and correlation between M-N-C structure and catalytic performance.

2.2. Modeling active site structure and catalyst interface

Our theoretical approach to modeling active sites has two key areas of innovation: (i) Identification of active-site features that control the three essential characteristics: ORR kinetics, structural stability and reaction selectivity. Descriptors will be gleaned from the electronic and geometric properties of the active sites and correlated with ORR activation barriers and formation energies.

We anticipate a distribution of candidate active sites for each model system (i.e. Fe-N$_4$ vs. Fe-N$_3$, edge vs. vacancy), and the overall strength of each system will be determined by a weighted average. (ii) Mesoscale models that couple molecular-level kinetics with mass- transport and mesoscale structure through DFT simulations.

2.3. Guided materials synthesis

The key aspect of the proposed research is to use the understanding of the active-site and optimal mesoscale structures gained in the project to design next-generation advanced catalysts. This effort will focus on the following innovative synthesis targets: modification of graphitic systems by incorporation of defects, transition metals and nitrogen doping.

2.4. Technical impact

Research in this project will advance fundamental electrocatalysis of oxygen electrochemistry, as well as develop novel materials and concepts for oxygen reduction and evolution reactions, the most important pair of electrochemical reactions today, in aqueous and nonaqueous media. Successful completion of the proposed research will lay a solid foundation for sustainable, high- energy-density, and low-cost electrochemical energy storage and conversion systems.

2.5. Synthesis of a model catalyst.

Previous studies have shown that active PGM-free catalysts are synthesized via heat treatment of M-N-C precursors. The understanding of the active site structure is a challenge given the heterogeneous nature of these catalysts. N-doped graphene is known to be an active ORR electrocatalysts [59, 81-87] and shows

many similarities to more complex catalysts while retaining a simpler structure, making it an ideal model catalyst to elucidate the electrocatalytic active sites. Thus, we propose to synthesize model electrocatalyst systems based on graphitic systems functionalized with non- precious metals that will be characterized using spectroscopic and imaging tools to identify the most active reaction sites.

2.6. Solvent-free route to the synthesis of PGM-free catalysts for ORR.

Graphite is an excellent starting material for the synthesis of PGM-free catalysts for its well-defined structure but also its excellent conductive and mechanical properties. Additionally, the intercalation of compounds between the graphitic sheets has been thoroughly studied to synthesize materials such as superconductive materials [65, 66, 68-70, 88, 89]. The synthesis of M-N-C catalysts requires several steps and the use of numerous solvents to yield a relatively small amount of catalyst. In this context, we propose a novel synthesis technique to yield large amounts of active materials for ORR. To achieve this, using metal halides, the synthesis of M-C compounds can be achieved with different degrees of stacking. The synthesis is done at high temperature (> 380 °C) to allow the evaporation of the alkali metals and allowing for the intercalation in graphite. Following the synthesis, these materials can be modified using different processes (functionalization, exfoliation, N-doping) to create M-N-C materials that are sought for the synthesis of PGM-free catalysts.

2.7. Modelling of the ORR active sites.

The electrochemical activity of PGM-free is highly coupled to the mesoscale structure of the catalyst: unlike PGM catalysts there is no distinction between

catalyst and support in PGM-free. Catalytic activity is, thus, multiscale, and requires theory to bridge the nano- and mesoscales. The graphitic systems described previously will be modeled using density functional theory (DFT) calculations to assign experimental spectra and to probe active-site geometry and electronic structure. Based on the understanding obtained from DFT, modifications to the graphitic systems will be made to test particular aspects of the theory. Thus, this will allow the development of a scientific framework critical for optimization of PGM-free electrocatalysts for clean energy production/storage.

2.8. <u>Rational Design and Synthesis of Next-Generation PGM-free.</u>

Previous results have identified ORR catalysts derived from non-precious metal, nitrogen and carbon precursors [26, 90-94] which are structurally similar to the model graphene catalytic systems we propose to study. Based on work derived from studies of the model graphene electrocatalysts, as well as past results, we propose to design, synthesize and optimize new non-precious metal electrocatalysts.

Ultimately, the proposed research is expected to answer key questions in PGM-free electrocatalysis, including (i) the effects of structure and morphology on catalyst activity and durability; (ii) the interaction between active sites and the carbon matrix; and (iii) catalyst degradation mechanism. This work will create a solid foundation for next generation PGM-free systems.

3. <u>Experimental Methods</u>

3.1. <u>Catalyst synthesis</u>

3.1.1. Graphite catalysts

Graphite, a compact stack of layers of sp^2 hybridized carbons arranged in a two-dimensional honeycomb structure [36], is extremely hydrophobic [95], and usually requires treatment under oxidative conditions such as strong acids [42, 43, 95, 96] to introduce defects and functionalities. The main interest being the development of a solvent-free synthesis route, other methods will be explored such as ball milling with various precursors to introduce mechanical defects while reducing the particle size, followed by a high temperature treatment to create and stabilize active sites. Exfoliation methods were also used to increase the surface area of graphite by high temperature treatment of graphite intercalation compounds.

3.1.2. Graphite Intercalation Compounds

Graphite Intercalation Compounds (GIC) are compounds intercalated between the sheets of graphite in a solvent-free, high temperature environment. GICs exist for alkali metals as well as metal halides and halogens.

Historically, they have been synthesized for their superconductive properties. In this work, we use metal halides iron chloride to synthesize novel PGM-free catalysts. This approach allows the incorporation of transition metals in graphite that are progressively modified to incorporate nitrogen compounds and bind the M-N-C elements.

3.1.3. Nitrogen-doped graphene oxide

Synthesis of graphene oxide (GO): GO was synthesized using a modified Hummers method [96]. Graphite is oxidized in presence of concentrated sulfuric acid and potassium permanganate. This synthesis method allows for the incorporation of metal traces (Mn) while introducing a high defect density and functional moieties, *i.e.*, carboxyl, hydroxyl and epoxy groups which facilitate nitrogen incorporation.

Solvent treatment of GO: GO undergoes an optional step of solvent treatment. Solvents are chosen based on Hansen's solubility parameters, offering a wide range of properties: dispersion, δd, hydrogen bonding, δH, and polarity, δp; as well as water miscibility, and boiling point. Excess water is removed from the precursors by high r.p.m centrifugation and solvents are mixed with the centrifugate. The slurry is dried before the final nitrogen-doping step.

Nitrogen doping of GO films: Nitrogen-doped GO (NrGO) was obtained by simultaneously reducing the catalyst while incorporating nitrogen in the system in a high temperature ammonia atmosphere. This method allows a 4-7 wt.% nitrogen incorporation in the graphene oxide material.

3.2. Structural characterization techniques

3.2.1. Scanning Electron Microscopy

Scanning electron microscopy (SEM) is a very powerful tool for imaging nanostructures. In the microscope, electrons are emitted from a tungsten filament at accelerated voltages ranging from 2 to 30 keV. The beam is focused through a series of lenses and swept across a small area of the sample. The material

irradiated by the electron beam interacts by elastic (without electronic excitation) and inelastic scattering (electronic excitation). The beam emits signals in the form of secondary electrons, backscattered electrons, photons and characteristic X-rays such as described by **Figure 2** below:
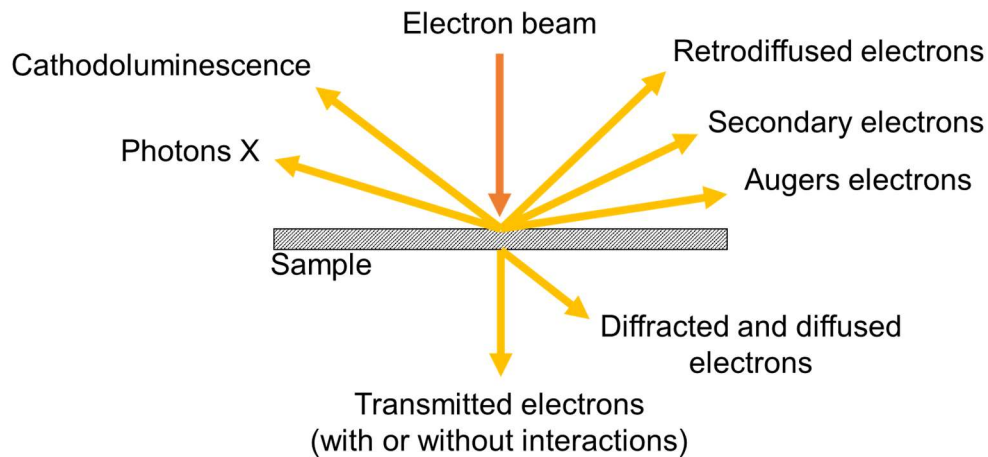
Figure 2: Schematic of the sample-ion beam interactions and different types of electrons.

Images referenced in various publications are obtained using secondary and backscattered electrons while characteristic X-rays provide useful information about the bulk composition of the studied material.

One unique feature of the graphitic model systems is that individual sheets of carbon can be manipulated at the macroscale; making them ideally suited for electron microscopy. We use SEM to characterize the defect sites that have been incorporated into the graphitic systems.

3.2.2. Transmission electron microscopy

Another microscopy technique, the transmission electron microscopy (TEM) differs from SEM by the fact that the beam of electrons is transmitted through and

interacts by elastic or inelastic scattering with an ultra-thin material. As a consequence of the interaction of the electrons transmitted through the material (**Figure 2**), an image is formed, magnified, and focused onto an imaging device, such as a fluorescent screen, a layer of photographic film, or detected by a sensor, such as a CCD camera. TEM devices allow high resolution imaging of nanomaterials and can obtain imaging of crystal structures, defect, and atomic rows.

A conventional TEM usually operates at a voltage of 100 to 300 kV. The column of the microscope constitutes of an electron cannon, an accelerator, two or three magnetic lenses that form a condenser, an objective lens, one or two intermediate lenses, a projection lens and a chamber of observation and recording of the image. The inside of the column is under a vacuum of approximately 10^{-3} to 10^{-5} Pa.

In this work, using the latest in analytical TEM technology, we resolve the model systems into their atomic components and study how the structure of the carbon lattice near a nitrogen/metal defect is altered.

3.2.3. XRD

X-Ray Diffraction (XRD) is a scattering technique used to provide essential structural information of a material using X-ray beams. Interference occurs when the X-ray beams with wavelengths similar to the spacing between atoms interact with the atomic planes of a crystal. This interference causes a diffraction of incoming x-rays which are collected by a detector at controlled angles. The diffraction pattern will be unique to the elements constituting the crystal and will be used to distinguish the different phases present in the material.

To obtain the diffractograms, the X-ray beams are emitted by x-ray tubes with a wavelength specific to the type of source material utilized. In this work, a Cu Kα radiation source was utilized with a wavelength of 1.5418 Angstroms.

The main objective for collecting XRD patterns in our carbon materials is to study the crystallinity as well as the changes occurring during the synthesis with the addition of metals, defects or the change of phases.

3.2.4. X-ray photoelectron spectroscopy

X-ray photoelectron spectroscopy (XPS) is a common technique to determine the elemental composition of materials. It is often referred to as a surface-sensitive technique but the information obtained is not limited to the sample surface (down to 6 nm). In the case of PGM-free catalysts, it can determine the type and relative amount of nitrogen functionalities doped into carbon as well as the valence state of metals in catalysts.

3.2.5. Raman spectroscopy.

Raman spectroscopy is a characterization tool that provides information about the vibration states of a material, a property that is characteristic of the chemical bonds and molecular symmetries present. A monochromatic light, usually in the form of a laser interacts with the electron clouds and molecular bonds of the sample, causing the molecules to shift to a more energetic vibration state. When relaxing, the molecules will return to an energy level slightly higher than in their initial state and will emit a photon with a frequency shift characteristic of this vibration state change providing a characteristic spectrum of the material. In this study, Raman spectroscopy is used to monitor structural deviations of graphite, graphene oxide,

and graphene. The spectra of carbon are affected by the ratio of sp^2/sp^3 bonds, crystallite size, bond-angle disorder, bond-length disorder, heteroatoms, etc. Characteristic peaks are located at 1300-1400 cm^{-1} corresponding to the D-band and the disorder-induced band; also, at 1560-1600 cm^{-1} corresponding to the G-band, originating from graphite like sp^2 hybridization of carbon. The D band is inversely proportional to the crystallite size. The ratio of I_D/I_G is often used to measure the degree of disorder in the graphene layer.

3.3. Electrochemical characterization

3.3.1. Voltamperometric techniques

3.3.1.1. Cyclic Voltammetry

In a cyclic-voltammetry (CV) experiment, the working electrode potential is continuously and linearly varied in time between two set limiting potentials. When CV reaches a set potential, the working electrode potential ramp is inverted. This inversion can happen multiple times during a single experiment. The rate of the potential variation is defined by the scan rate, expressed in V/s or mV/s. The current flowing through the working electrode (i) is plotted versus the applied potential (E), yielding a cyclic voltammogram as shown in **Figure 3**. CV is generally used to study the electrochemical properties of catalysts in solution.
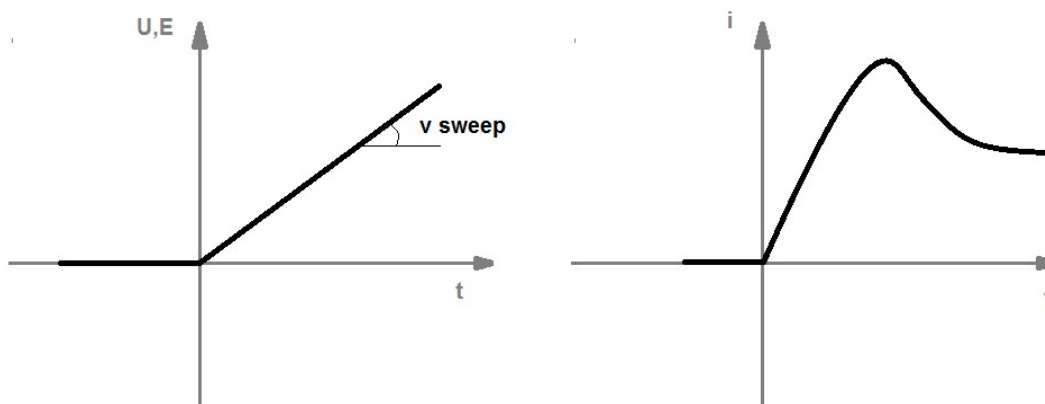
Figure 3: Description of cyclic voltammetry with the imposed voltage (left) and the current response (right). Inspired by [97]

Typically, the current increases as the potential reaches the reduction/oxidation potential of the electroactive species, but then falls off as the concentration of the analyte is depleted close to the electrode surface. If the electrochemical reaction is reversible, then when the applied potential is reversed, the products of initial can oxidize/reduce to re-create the original species.

The utility of CVs highly depends on the nature of the studied electroactive species. The species need to be electroactive within the potential window used.

3.3.1.2. Chronoamperometry

Chronoamperometry is an electrochemical technique in which the potential of the working electrode is stepped and the resulting from the potential step is measured as a function of time as described in **Figure 4**.
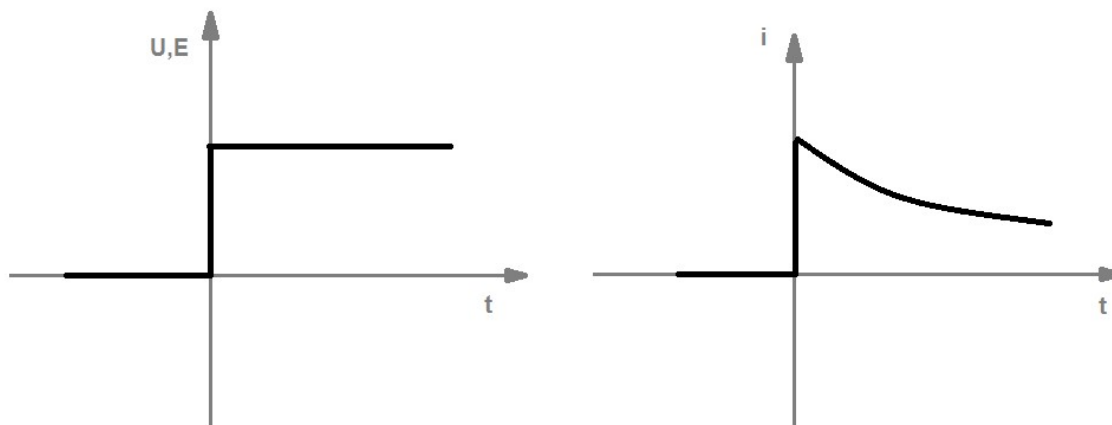
Figure 4: Description of chronoamperometry with the imposed voltage (left) and the current response (right). Inspired by [97].

Since the current is recorded over relatively longer time intervals, chronoamperometry gives a better signal to noise ratio in comparison to other amperometric techniques. After a certain period, the experiment reaches a steady state when current does not change with time. This condition is useful to analyze the behavior of electrochemical systems.

3.3.1.3. Staircase voltammetry

Staircase voltammetry is a combination of the two previous techniques. The potential is varied in voltage steps that are held for a certain time. This allows the study of the reaction in a quasi-steady state, allowing a more precise study of the electrochemical reaction. In the data presented in this study, the voltage steps are 30 mV held for 30 seconds. Only the last 50% of the step current is recorded for more accuracy.

3.3.2. Half-cell experiment

Electrochemical characterization was conducted using a rotating ring disk electrode (RRDE), a sensing electrode that typically operates in a three-electrode system under well-defined hydrodynamic conditions.
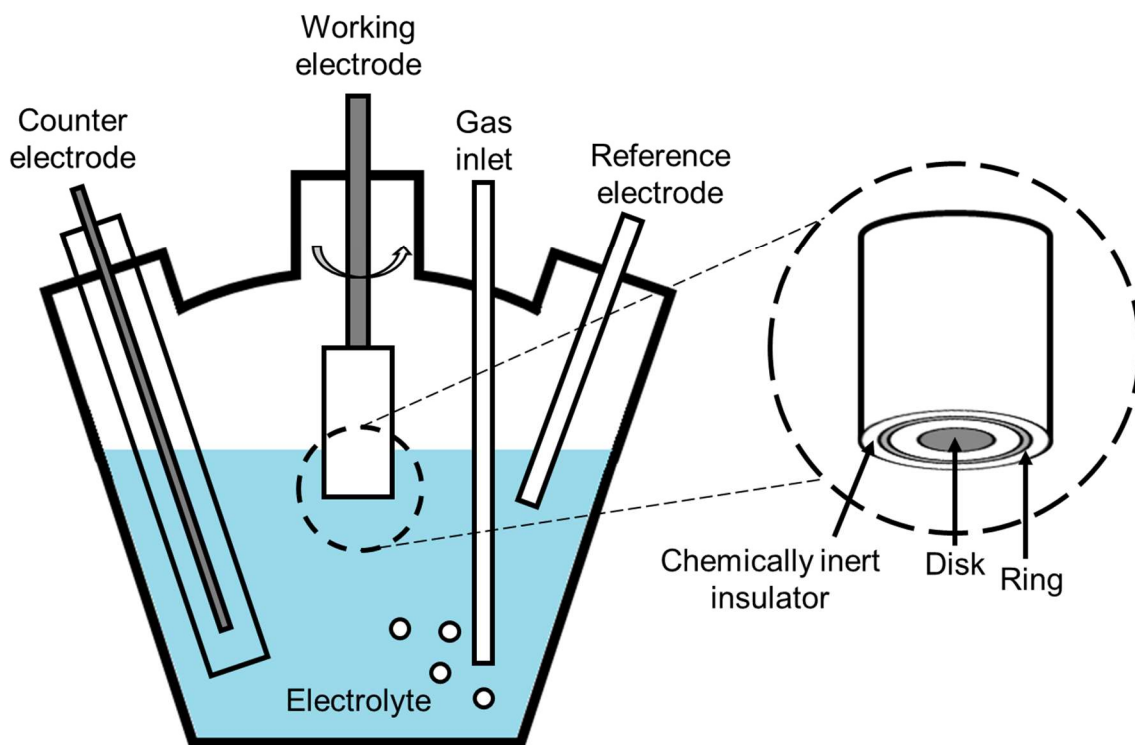
Figure 5: Schematic of a RRDE setup with corresponding working electrode.

The three-electrode system consists of a working electrode, a reference electrode and a counter electrode as described in **Figure 5** above:

(i)   The working electrode is the electrode at which the reaction of interest is occurring. Typically, it is made of inert metals such as gold, silver or platinum or inert carbons, such as glassy carbon. In the case of the study of PGM-free catalysts, we use glassy carbon electrodes to avoid any contamination of precious metals to the catalyst of interest. Additionally,

a ring can be used to monitor secondary reactions such as the reduction of peroxides into water as a byproduct of the reduction of oxygen into water.

(ii)   The reference electrode is an electrode that has a stable, measurable and well-known potential. The high stability of the electrode potential is usually reached by employing a redox system with constant concentration (activity) of reagents in the redox reaction. Out of many reference electrodes the most commonly used ones are the hydrogen, calomel silver/silver chloride, as well as normal, standard, and reversible hydrogen electrodes.

(iii)   The counter (or auxiliary) electrode is needed in systems generating currents. The counter and working electrodes together make up an electrical circuit, in which the current is either generated or forced to flow. The counter electrode prevents ohmic losses from affecting the value of the working electrode potential measured against a known reference electrode. The auxiliary electrode, usually a platinum wire or a graphite rod, may be isolated from the working electrode using a glass frit.

The electrodes are immersed in a glass cell containing 0.5 M H_2SO_4 or 0.1 M NaOH for acidic and alkaline testing, respectively. Rotation of the working electrode forces a controlled flux of electroactive species to the electrode, at which they undergo reduction or oxidation. Different rotation speeds were employed (600, 900,1200, and 1500 rpm) and all testing were carried out at room

temperature (*ca*. 25°C). RRDE is used in electrochemical studies of the rates and mechanism of redox processes on solid electrodes.
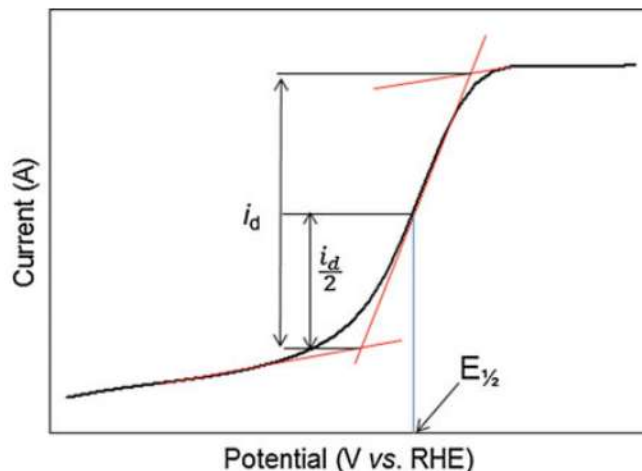
Figure 6: Example of an ORR polarization plot, highlighting the E_{onset}, $E_{1/2}$ and limiting current.

The ORR polarization plots of a catalyst were obtained in an O_2 -saturated medium, running a step-voltammetry measurement from 1.2 V to 0 V vs. RHE. While the ORR is occurring at the disk, the rotation of the electrode sweeps away the reactants. The Pt ring is held at a potential such as any peroxide radicals produced during the ORR is oxidized. An example of an ORR polarization plot is shown in **Figure 6**.

The performance of a catalyst toward the ORR is defined by:

    i.   The onset potential (E_{onset}) of the catalyst, i.e., the potential at which the catalyzed ORR current starts to appear

    ii.   The limiting current density and the half-wave potential ($E_{1/2}$)

    iii.   Its selectivity towards the four-electron reduction of oxygen determined by the following equations:

$$\%_{peroxides} = \left(1 - \frac{i_d - \left(\frac{i_r}{N}\right)}{i_d + \left(\frac{i_r}{N}\right)}\right) * 100 \qquad (8)$$

$$n = 4 * \frac{i_d}{i_d + \frac{i_r}{N}} \qquad (9)$$

With i_d being the current measured at the disc, i_r the current at the ring, N the efficiency of the Pt ring (in our experiments, N=37%).

The thermodynamic reversible potential (E°) of oxygen reduction at 25°C is 1.23 V versus the reversible hydrogen electrode (RHE). Any additional potential required to drive the ORR is called the overpotential (η). High-performing ORR catalysts are characterized by low η, high E½, high selectivity values for four-electron transfer and high limiting current.

The Koutecky-Levich equation is used to investigate kinetics of the ORR using the polarization plots described in **Figure 6**. The current density observed can be broken down following **Equation (10)**:

$$\frac{1}{i} = \frac{1}{i_k} + \frac{1}{i_d} \qquad (10)$$

With i being the total current density, i_k is the kinetically limited current density, and i_d is the diffusion limited current density. At high overpotentials, i_k will be very large and this term will become negligible. i_d depends on the electrode rotation speed (ω) and can is expressed mathematically by **Equation (11)**:

$$i_d = 00.62 \, n \, F \, C_{O2} \, D_{O2}^{\frac{2}{3}} \, v^{-\frac{1}{6}} \, \omega^{\frac{1}{2}} \qquad (11)$$

Where n is the average number of electrons transferred in the reaction, F is Faraday's constant, C_{O2} is the concentration of oxygen in the electrolyte, D_{O2} is the diffusion coefficient of oxygen in the electrolyte, and v is the viscosity of the solution. ω being the only variable, the other values are constants and can be combined into a single constant B as described by **Equation (12)**:

$$\frac{1}{i} = \frac{1}{i_k} + \frac{1}{B\,\omega^{\frac{1}{2}}} \qquad\qquad (12)$$

A Koutecky-Levich plot is displayed as i^{-1} as a function of ω^{-1} and shows a linear behavior with a y-intercept of i_k^{-1} and a slope of B^{-1}. It allows the determination of the number of electrons transferred per molecule of oxygen and thus its selectivity towards the more efficient 4 electron reduction process.

4. **A green approach to the synthesis of graphite-based materials active towards the Oxygen Reduction Reaction in alkaline medium**

4.1. Introduction

The study of novel materials and their activity towards the oxygen reduction reaction (ORR) is being critical to the development of a variety of electrochemical devices such as metal-air batteries, electrolyzers and fuel cells [98-101]. State-of-the-art ORR catalysts are based on costly platinum group metals (PGM) that have limited the distribution and commercialization of such devices. As an alternative, PGM-free catalysts are synthesized from earth-abundant elements via heat treatment of transition-metal (M), nitrogen (N), and carbon (C) precursors [13, 22, 23, 25-31, 86, 90-92, 102-112] and have the potential to generate clean energy through the efficient reduction of oxygen. Despite the promising progress that PGM-free electrocatalysts have demonstrated, they have also shown limits that need to be addressed:

i) The state-of-the-art PGM-free catalysts, regardless of their initial performance, have shown an insufficient durability for the current electrochemical applications.

ii) The development of high-performing materials active towards the ORR suffers from a lack of understanding of the exact nature of the active site(s) and remains to this day the subject of intense discussions in the field [2, 31-35].

iii) The synthesis of such electrocatalysts for the ORR is often a complex process involving heterogeneous precursors, numerous synthesis steps

as well as the use of hazardous solvents such as strong acids and yields more often than not a very small fraction of usable material [22, 91].

Graphitic materials [99, 113-117] are widely utilized as catalyst supports for fuel cells [108, 118], and ORR electrocatalysts [27, 90, 119] but graphite itself has not been fully investigated as an active material to reduce oxygen. Although a relatively simple material, it can be used as a model system to mimic many of the structural and functional properties found in the more complex and high performing PGM-free catalysts. Furthermore, the nature of its 2D sp^2-bonded carbon sheets, mechanically and chemically resistant to corrosion, makes it an ideal candidate for highly durable ORR performance.

Since recent studies suggest that the removal of water is the key to the design of the next generation of PGM-free catalysts [87], we have chosen a green synthesis route to modifying graphite using few-steps processes while involving no solvents. Although some efforts were made to reduce waste by choosing a green and cost-effective route [120], none were able to successfully remove solvent from the synthesis steps. Our efforts aim at the total elimination of generated waste and the implementation of sustainable processes to generate cheap, high yielding, efficient and durable ORR electrocatalysts.

Firstly, we synthesized graphite intercalation compounds (GICs) to incorporate metal halides in a well-ordered graphite structure. GICs are a unique class of lamellar materials formed by the insertion of atomic or molecular species between the planes of graphite. They have been investigated for electrochemical applications in batteries or as electrodes [71]. So far, they have not been tested

for the electrochemical reduction of oxygen. Their facile synthesis, the relatively simple structure and the presence of metals establish GICs as an ideal model for PGM-free catalyst. Secondly, graphite was modified by reducing the crystal structure while introducing N and M elements *via* a two-step ball-milling and pyrolysis process in a solvent-free environment. Each synthesis step induces changes in morphology and elemental composition that are carefully characterized using electron microscopy as well as spectroscopic techniques such as XPS.

Ultimately, this work allows the development of a new, green and sustainable synthesis route for active electrocatalysts while providing a better understanding of the active site formation and reaction mechanism in alkaline medium that is a crucial step in developing superior catalysts.

4.2. <u>Materials and Methods</u>

4.2.1. Synthesis of catalysts

The green catalyst approach involves the need to decrease the numbers of chemical steps while reducing the use of solvents and corrosive materials to eliminate the excess waste during the synthesis of active ORR electrocatalysts.

GICs were synthesized by mixing graphite with $FeCl_3$ with a mass ratio of 1:5 in a pressure vessel under inert atmosphere to prevent the presence of water and oxygen. The vessel was placed in an oven at 380°C for 4 hours and then cooled down to room temperature.

Nitrogen-doped GICs (NGICs) were synthesized by thermal reduction and nitrogen incorporation using high-temperature ammonia gas treatment. GIC powders were

placed in an alumina crucible inside a quartz furnace tube. The tube was first vented with UHP Ar gas (100 sccm flow) for 60 minutes. Ammonia gas was then introduced at 60 sccm and the temperature was increased to 850°C at a rate of 1°C/min. The furnace temperature was maintained 850°C for 180 minutes and then slowly cooled to room temperature.

Graphite was ball milled in presence of nitrogen precursors (urea, 1:5 molar ratio) and / or metal precursors (phenantrholine, iron chrloride, 1:1 molar ratio) to reduce the particle size while ensuring a homogenous mix of the carbon and the precursors . The resulting material was then placed in a ceramic crucible within a quartz furnace tube. The tube was purged with 100 sccm of UHP Ar for 15 minutes and afterwards the temperature was increased to 900°C at a rate of 30°C/min. This temperature was maintained for 3 hours and slowly cooled down to room temperature.

4.2.2. Physical characterization

XRD spectra were obtained using a Siemens D5000 diffractometer with Cu Kα radiation (1.5418 Å) and a graphite diffracted beam monochromator. The spectra were analyzed using JADE XRD analysis software (Materials Data Inc.). All measurements were done at room temperature.

The structure and the morphology were studied using electron microscopy. Scanning electron microscopy (SEM) images were taken at 5 kV with a FEI Quanta 400 ESEM.

4.2.3. Electrochemical characterization

Rotating ring disc electrode (RRDE) measurements of the oxygen reduction reaction were performed in a conventional three-electrode cell at a rotating disk speed of 900 r.p.m., at room temperature, using a VMP3 potentiostat (Bio-Logic). The catalyst loading was 0.6 mg cm^{-2}. A platinum wire was used as a counter electrode, while an Hg/HgO (1.0 M KOH, 0.880 V *vs*. RHE) was used as a reference electrode. ORR steady-state polarization curves were recorded in an O$_2$-saturated 0.1 M NaOH electrolyte with a 30 mV step held for 30 seconds. The Platinum ring was held at a constant potential of 1.3 V *vs.* RHE.

4.3. Results and Discussion
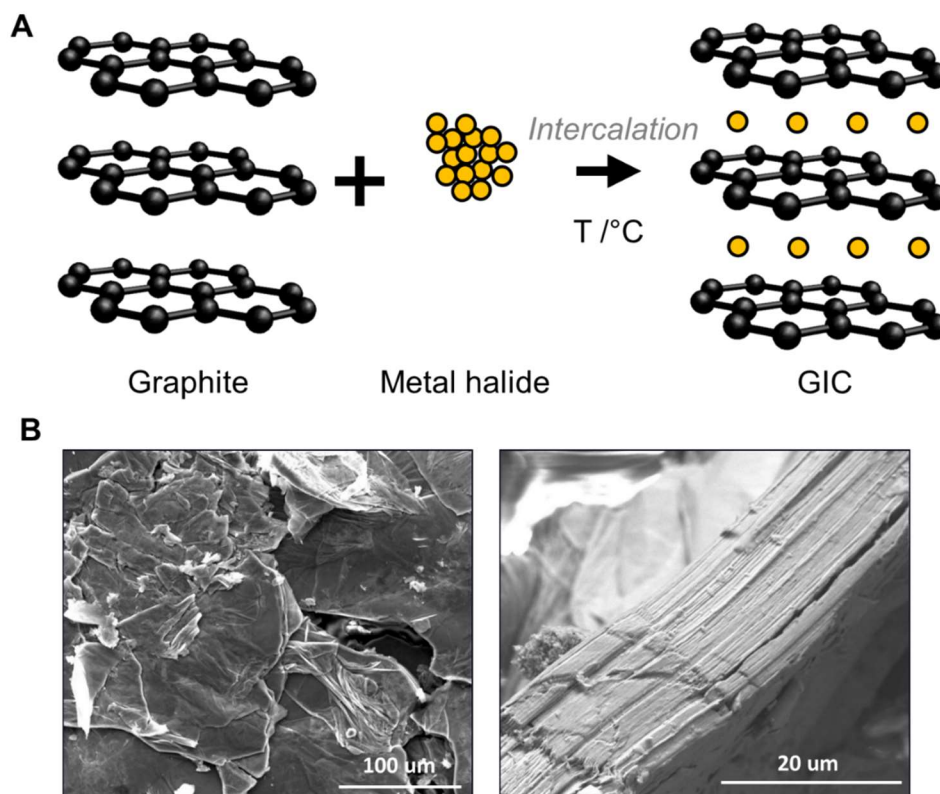
Figure 7: (A) Schematic of the synthesis process of graphite intercalated compounds and (B) SEM images of the resulting material.

The incorporation of M and N functionalities to graphite is a crucial step to synthesizing PGM-free catalysts. Graphite, a compact stack of sp^2 hybridized carbon sheets with an interplanar distance of 3.4 Å, is enclosed in presence of a metal halide ($FeCl_3$) in a pressurized vessel in inert atmosphere *via* a well-described process shown in **Figure 7 A**. The SEM images of GICs (**Figure 7 B**) show no significant morphological changes as opposed to graphite. The structure appears lamellar and ordered with no significant amount of impurities such as excess $FeCl_3$ visible, suggesting that the intercalation reaction was complete.
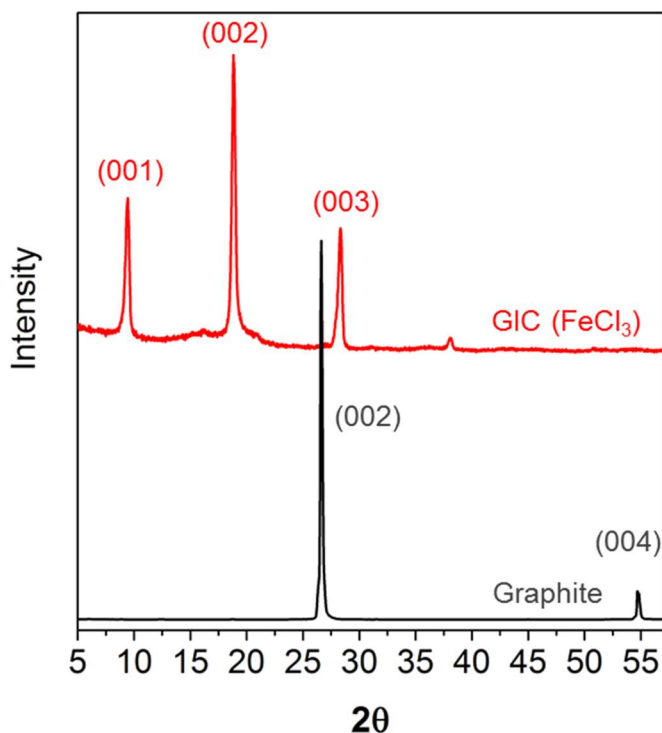
Figure 8: XRD patterns of graphite compared with GIC ($FeCl_3$)

The crystalline structure of GIC ($FeCl_3$) is confirmed by XRD analysis (**Figure 8**). Pristine graphite shows two peaks with an (002) and (004) index corresponding to an ordered periodic structure with a interlayer spacing of 3.4 Å. the intercalation

with $FeCl_3$ generates new peaks at 9.5°, 18.9°, 28.3°, 38.1° and 58.4° with an interlayer spacing of 9.4 Å which agree well with the pattern of a stage 1 structure of GIC($FeCl_3$)[121]. The XRD spectra show no peaks that can be attributed to graphite, $FeCl_3$, Fe_2O_3 or Fe_3O_4, or in quantities too small to be detected by XRD, which suggest that the reaction was complete.
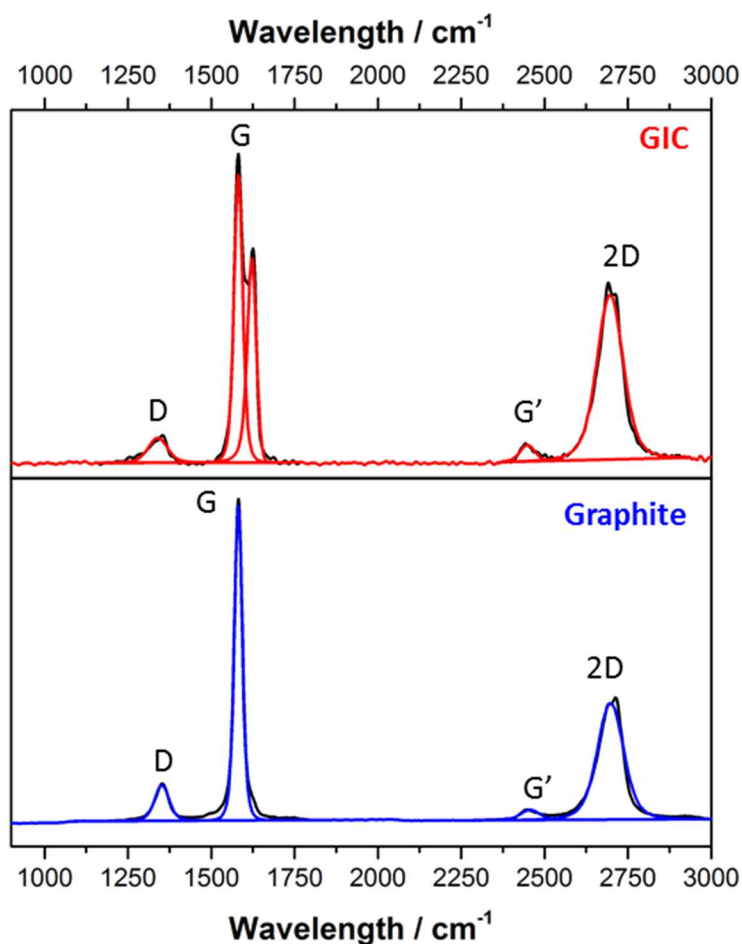
Figure 9: Raman spectra of graphite compared with GIC ($FeCl_3$)

Raman spectroscopy performed on graphite and GIC (FeCl3) is shown in **Figure 9**. All spectra show the presence of a peak at 1300-1400 cm^{-1} corresponding to the D-band, the disorder-induced band, as well as a peak at 1560-1600 cm^{-1}

corresponding to the G-band, originating from graphite like sp^2 hybridization of carbon. While both spectra show a low D/G ratio which determines a highly ordered, pristine graphitic material, the GIC spectra exhibits a splitting of the G band towards higher wavelength values (1625 cm^{-1}). This upward shift, due to the change in the Fermi level, is specific to the intercalation of p-type compounds[89]. Additionally, the spectra show a strong, broad peak at 2670 cm^{-1} corresponding to the 2D band and a weaker peak at 2450 cm^{-1} corresponding to the G'. Both 2D and G' peaks are specific to multilayered graphene sheets[122].
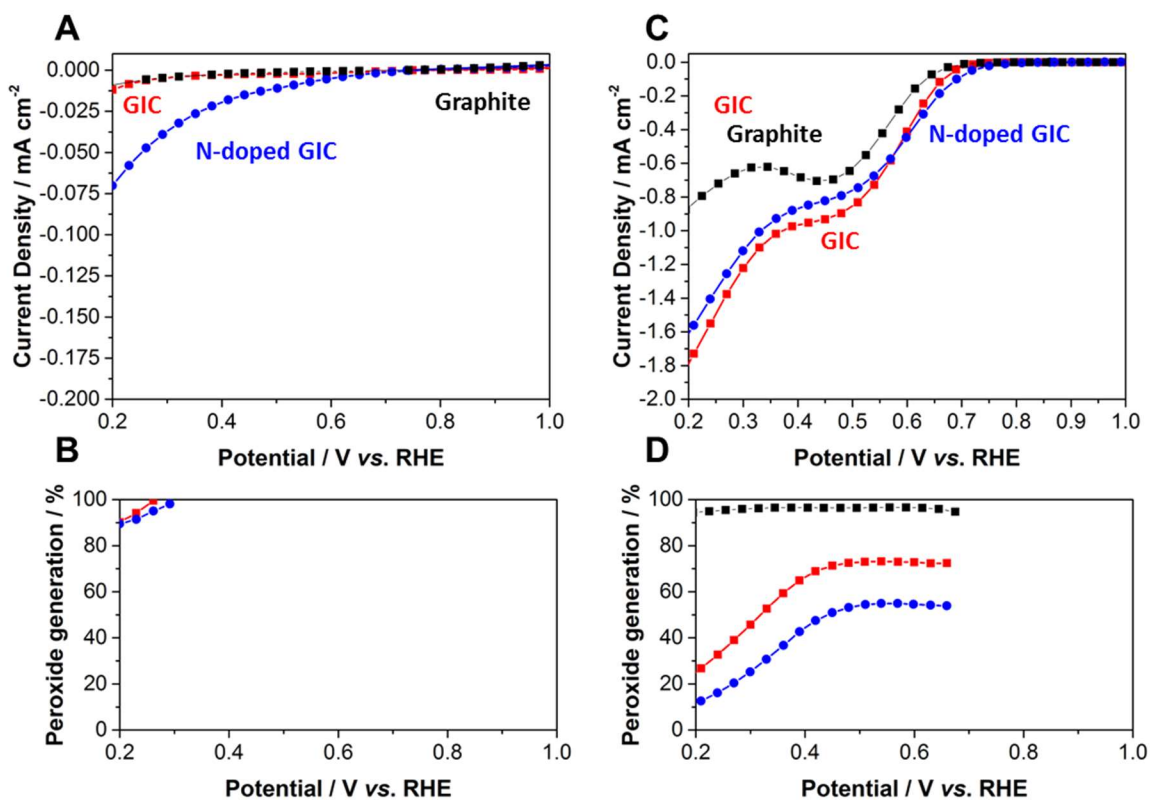
Figure 10: Electrocatalytic performance and selectivity of GIC and nitrogen-doped GIC compared to graphite; (A) ORR performance in 0.5 M H_2SO_4 with (B) corresponding H_2O_2 yield; (C) ORR performance in 0.1 M NaOH with (D) corresponding HO_2^- yield.

The electrocatalytic ORR activity and selectivity of the GIC (FeCl₃) electrocatalyst, as prepared and nitrogen-doped, was measured using a rotating-ring disc electrode (RRDE) in O₂-saturated 0.5 M H₂SO₄ and 0.1 M NaOH electrolyte (**Figure 10**). Selectivity of the ORR was determined according to **Equation (8)**:

$$\%_{peroxides} = \left(1 - \frac{i_d - \left(\frac{i_r}{N}\right)}{i_d + \left(\frac{i_r}{N}\right)}\right) * 100 \qquad (8)$$

In acid and alkaline environments, the ORR ideally proceeds via a four-electron pathway according to **Equation (5)**:

Acidic	**Alkaline**	

$$O_2 + 4H^+ + 4e^- \rightarrow 2H_2O \qquad\qquad O_2 + 2H_2O + 4e^- \rightarrow 4OH^- \qquad (5)$$

However, it can also proceed via a 2+2 electron reaction according to **Equations (6)** and **(7)**:

Acidic	**Alkaline**	

$$O_2 + 2H^+ + 2e^- \rightarrow H_2O_2 \qquad\qquad O_2 + H_2O + 2e^- \rightarrow HO_2^- + OH^- \qquad (6)$$

$$H_2O_2 + 2H^+ + 2e^- \rightarrow 2H_2O \qquad\qquad HO_2^- + H_2O + 2e^- \rightarrow 3OH^- \qquad (7)$$
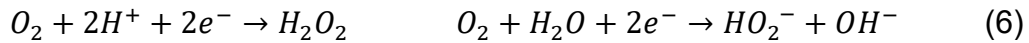
In acid conditions, the ORR polarization of graphite and GIC show very little performance and selectivity towards the 4e⁻ reaction with very low E_{onset} at 0.40 V *vs*. RHE *i.e.*, the potential at which the catalyzed ORR current starts to appear, an average of 100% H₂O₂ yield at 0.5 V *vs*. RHE and no limiting current. The ORR

performance of the nitrogen-doped GIC (NGIC) offer a small improvement with an E_{onset} of 0.75 V.

In alkaline conditions, the ORR polarization plot of graphite is a perfect study case of a hydroperoxyl generating catalyst, reducing water mostly via **Equation (6).** It shows a low E_{onset} at 0.70 V *vs*. RHE *i.e.*, the potential at which the catalyzed ORR current starts to appear, an average of n=2 electrons exchanged per molecule of oxygen at 0.5 V *vs*. RHE and no limiting current. The ORR performance of the GIC and nitrogen-doped GIC (NGIC) offer a small improvement with an E_{onset} of 0.73 V and 0.77 V *vs*. RHE for GIC and NGIC, respectively. Similarly to graphite, they show a clear 2+2 electron pathway with an average of n=2.5 and n=2.9 electrons exchanged per molecule of oxygen at 0.5 V *vs*. RHE for GIC and NGIC, respectively and no limiting current. The increase in the number of electrons (n) per molecule of oxygen suggest that some of the hydroperoxyl species generated in **Equation (6)** are being reduced to OH- following **Equation (7)**. Although the incorporation of metal between the graphite sheets was successful, this process was not able to successfully bind M and N to the carbon structure. Therefore, it is necessary to create more defects to the carbon structure to facilitate the incorporation of M and N to carbon.
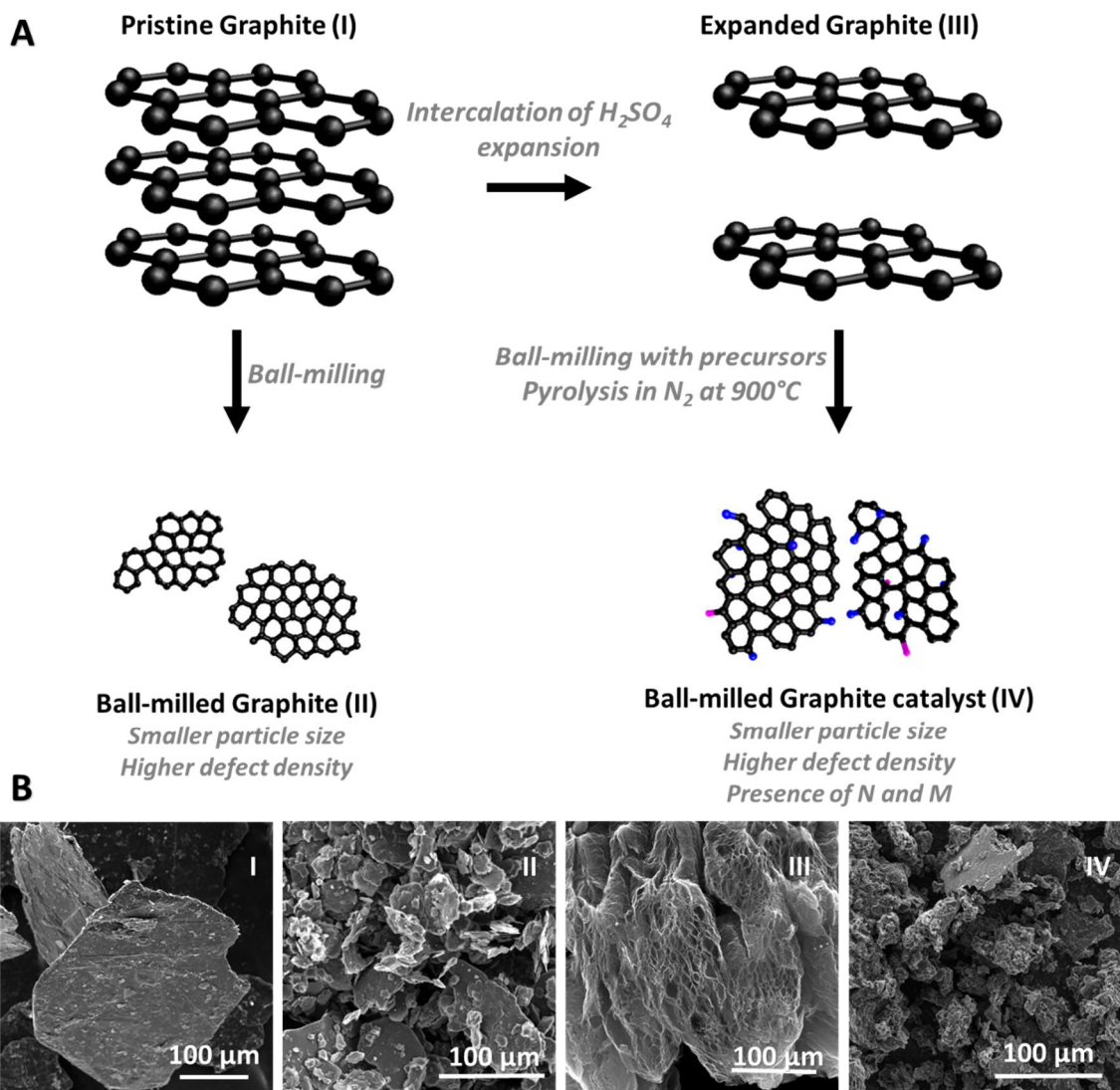
Figure 11: (A) Schematic of the synthesis process of graphite with M and N precursors and (B) SEM images of the resulting material.

The alternative approach described in **Figure 11 A** is to use ball milling to create more defects, both in plane and edge that will be used as anchor points for M and N precursors. The starting material, graphite was ball milled to understand the effect of ball milling on the material. Further, GIC was synthesized using concentrated sulfuric acid and then expanded by a brief microwave treatment. The expanded graphite was then ball milled in presence of M and N precursors in an

inert atmosphere. The resulting mix was then subjected to high temperature treatment in N_2 to successfully bind the M and N elements to carbon. The SEM images shown in **Figure 11 B** reveal significant differences between sample: (I) graphite is made of mostly wide sheets of 300 μm with very few defects exposed. (II) The ball milling process reduces the particle size to 30-50 μm and consequently increases the edges exposed. The short microwave treatment caused an increase in temperature and the expansion of graphite which gives graphite the accordion-like morphology shown in (III). Finally, the final products in (IV) show a smaller particle size with a very defective aspect, closer to a porous type of carbon.
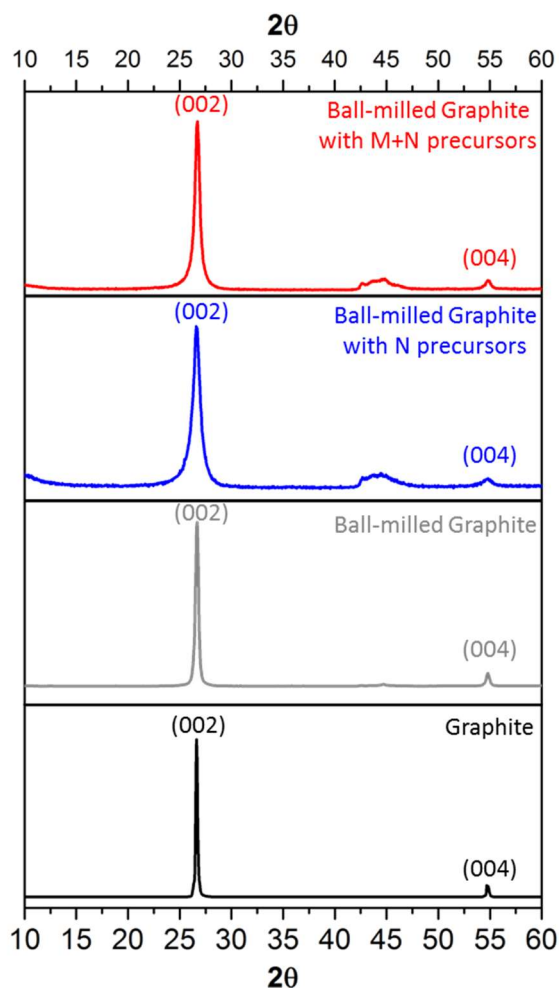
Figure 12: XRD patterns of graphite synthesized graphite-based electrocatalysts.

While the nature of the materials doesn't vary between steps with the (002) and (004) peaks located at 26.6° and 54.7°, the different morphologies witnessed using SEM are confirmed by XRD spectra. In fact, the ball milling treatment significantly reduced the particle size whereas urea, a known N-precursor and pore-forming agent, increased the strain in the material while reducing the particle size. The summary of the XRD analysis is shown in **Table 1** below.

Table 1: Analysis of crystallite size, lattice strain and d-spacing of the graphite-based materials

Parameters	Graphite	Ball-milled Graphite	Ball-milled Graphite with N precursors	Ball-milled Graphite with M+N precursors
Peak position	26.63	26.67	26.61	26.7
FWHM	0.215	0.379	1.069	0.664
Cristallite size / nm	39.71	22.53	7.99	12.86
d-spacing / Å	3.347	3.342	3.349	3.339
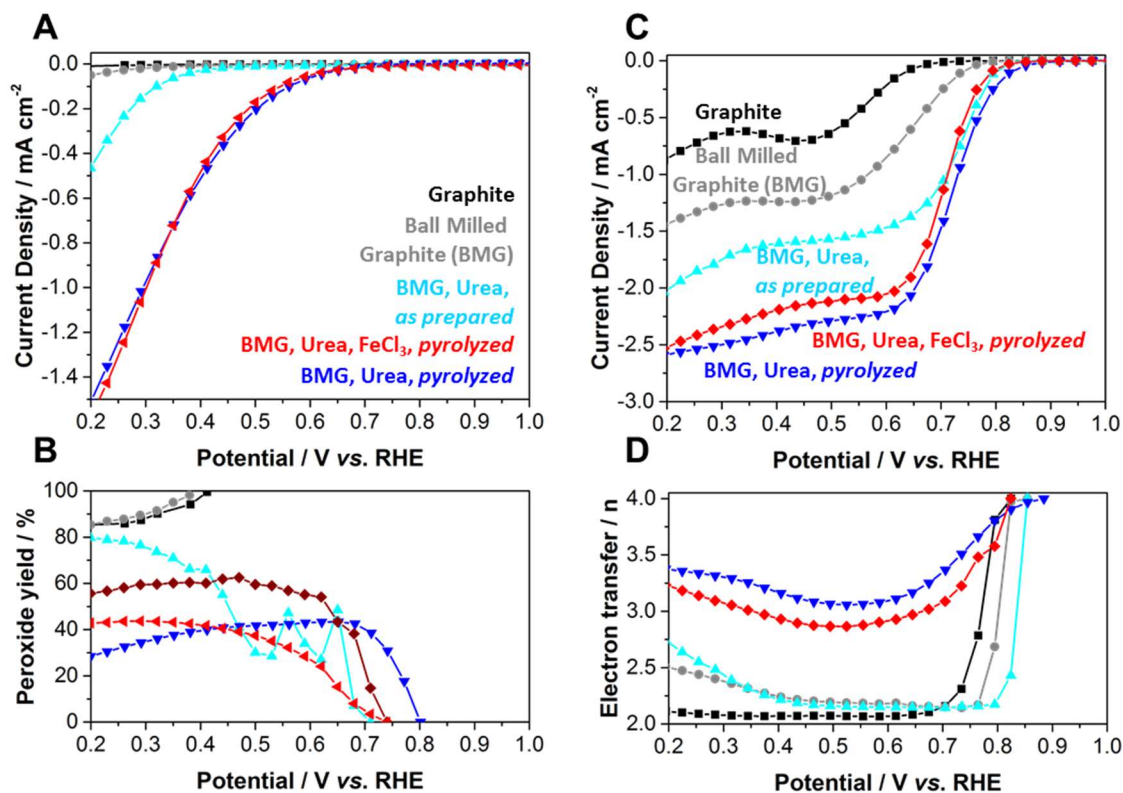
Figure 13: Electrocatalytic performance and selectivity of the synthesized graphite-based electrocatalysts compared to graphite. (A) ORR performance in 0.5 M H_2SO_4 with (B) corresponding H_2O_2 yield; (C) ORR performance in 0.1 M NaOH with (D) corresponding number of electron, n.
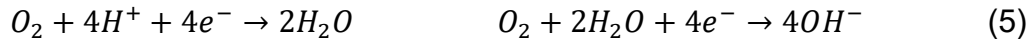
In acid conditions (**Figure 13 A-B**), the ORR polarization of graphite and GIC show very little performance and selectivity towards the $4e^-$ reaction with very low E_{onset} at 0.40 V *vs*. RHE, an average of 100% H_2O_2 yield at 0.4 V *vs*. RHE and no limiting current. The ball milling of graphite has not changed the nature of active sites significantly but rather has increased the edges exposed that leads to an improved E_{onset} at 0.42 V *vs*. RHE, 100% H_2O_2 yield at 0.4 V *vs*. RHE and no limiting current. Ball-milling expanded graphite with urea with no pyrolysis increase the E_{onset} to 0.52 V *vs*. RHE, 60% H_2O_2 yield at 0.4 V *vs*. RHE and higher currents drawn with,

however, no limiting current. The last two samples, both ball-milled with urea, with only one containing a M precursor ($FeCl_3$) highlight the importance of pyrolysis in the process of making more efficient catalysts. The ORR performance of the N and N+M containing ball-milled graphite materials offer a significant improvement with an E_{onset} of 0.80 V and 0.82 V vs. RHE, respectively. Additionally, they show a better selectivity for the 4-electron reaction with an average of 40% H_2O_2 yield for both samples. Finally, these catalysts present the same characteristics as the previous ones with no limiting currents observed.

In alkaline conditions (**Figure 13 C-D**), the ORR performance of the graphite-based materials highlights the consequences of all the synthesis steps. Our reference material, graphite, shows a poor ORR performance with an E_{onset} at 0.70 V vs. RHE, an average of n=2 electrons exchanged per molecule of oxygen at 0.5 V vs. RHE and no limiting current. The ball milling of graphite has not changed the nature of active sites significantly but rather has increased the edges exposed that leads to an improved E_{onset} at 0.79 V vs. RHE, n=2.1 electrons exchanged per molecule of oxygen at 0.5 V vs. RHE and no limiting current. Ball-milling expanded graphite with urea with no pyrolysis increase the E_{onset} to 0.82 V vs. RHE, n=2.1 electrons exchanged per molecule of oxygen at 0.5 V vs. RHE and higher currents drawn with, however, no limiting current. The last two samples, both ball-milled with urea, with only one containing a M precursor (phenanthroline) highlight the importance of pyrolysis in the process of making more efficient catalysts. The ORR performance of the N and N+M containing ball-milled graphite materials offer a significant improvement with an E_{onset} of 0.89 V and 0.82 V vs. RHE, respectively.

Additionally, they show a better reduction of hydroperoxyl species (**Equation (7)**) with an average of n=3.1 and 2.9 for the N and N+M containing ball-milled graphite, respectively. Finally, these catalysts are steadily reaching limiting currents of 2.5 mA cm^{-2} which was not observed for the previous materials. This can be explained by the fact that at high temperature, urea decomposes in ammonia and isocyanic acid as described in **Equation (8)** below:

$$(NH_2)_2CO\ (s)\ \rightarrow\ NH_3\ (g)\ +\ HNCO\ (g) \qquad\qquad (8)$$
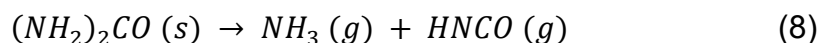
The high temperature treatment of materials in an NH$_3$ environment is a crucial step to incorporate N into the carbon structure and to obtain high performing electrocatalysts[2, 9, 13, 60, 63]. Although it is expected that the ORR performance would benefit from the presence of iron, it is likely that iron acted as a catalyst for the decomposition of ammonia[123, 124] and allowed only a partial incorporation of N in the carbon material.

4.4. Conclusion

In summary, we demonstrate that a green, solvent-free and sustainable synthesis route to create active ORR electrocatalysts based on graphite is possible. The simple ball milling of expanded graphite in presence of metal and nitrogen precursors followed by a pyrolysis step can create more active and more selective catalysts towards the ORR. Further advances in catalytic performance should be obtainable by varying the nature of the M and N precursors miscibility, and creating smaller particle size. The fundamental understanding obtained from our new aqueous-free approach has the potential to establish the path to green synthesis directed to PGM-free electrocatalysts.

5. **Critical role of intercalated water for electrocatalytically active nitrogen-doped graphitic systems**

5.1. Introduction

Graphitic materials [99, 113-117] are widely utilized for a variety of energy conversion and storage devices such as electrodes in Li-ion batteries, supercapacitors [98, 125], catalyst supports for fuel cells [108, 118], and oxygen reduction reaction (ORR) electrocatalysts [27, 90, 119]. Nevertheless, further development of carbon materials for energy-related applications suffers from a limited understanding of the design factors that control the formation of high-performing materials. This is mainly due to their complex heterogeneous character. In an effort to address this critical issue, numerous studies have focused on the use of ordered graphitic carbon materials [113-117, 125, 126]. Typically, reduced graphene oxide (GO) is used for energy-related applications because it can be produced in sizable quantities and heteroatoms (N, B, S) and transition metals (Fe, Ni, Co) can be readily incorporated into the graphene lattice [90, 102, 127]. Despite the fact that GO is synthesized and processed in aqueous environments, the role of intercalated water in the resulting structure and chemical composition for energy-related processes is rarely discussed [18, 27, 84, 114, 117, 119]. Particularly, the role of water and its impact on structure, morphology and catalytic activity during reduction of GO is not well understood [128].

Here, we demonstrate for the first time, the critical role of the removal of intercalated water from within graphene nanosheets in the formation of functional graphitic materials. Removal of intercalated water is achieved using a solvent

drying technique based on Hansen's solubility parameters (dispersion, δ_d, hydrogen bonding, δ_H, and polarity, δ_p), leading to dramatic impact in the graphene oxide physical structure decreasing the interlayer d-spacing as well as changing the concentration of functional groups. The decrease in interlayer spacing leads to emergence of structured water (similar to that observed in ice) at room temperature. Further, as a practical example, we demonstrate the applicability of this phenomenon in the formation of ORR active GO catalysts. In sharp contrast with previous reports demonstrating ORR performance of GO catalysts only in alkaline media, we report a catalyst that possess highest activity reported to date in acidic media, a technologically relevant pH environment. More importantly, our findings suggest that removal of water is the key to the design of next-generation carbon nanomaterials to realize their full potential for energy applications.

5.2. Materials and Methods

5.2.1. Synthesis of graphene oxide.

Graphene oxide (GO) was synthesized via a modified version of the Hummers method [129]. In brief, 4g of graphite powder (Bay Carbon Inc.) were dispersed in 500 ml of 98% H_2SO_4 using a mechanical stirrer. A total of 16g of $KMnO_4$ were added to the mixture over a period of 4 days (4g/day). The reaction mixture was then quenched with 500 ml of ice-cooled DI H_2O, slowly added. About 4 ml of 30% H_2O_2 were added to the mixture dropwise until the slurry turned yellow. The slurry was then centrifuged until the supernatant became clear. The supernatant was decanted and the precipitated GO was resuspended in H_2O. The washing process

was repeated 3x, followed by 2x washes in 10% HCl and a final wash in DI H_2O. The final product was resuspended in H_2O for further use.

5.2.2. Solvent treatments of GO

Prior to any solvent treatment GO-H_2O suspension was centrifuged to remove excess water. Centrifuged GO was then rinsed with 30 ml aliquots of solvents: water, ethanol, and diethyl ether. The GO-solvent solution was mixed with a vortex mixer. Solvent-treated GO was then centrifuged at 4000 rpm for 30 minutes, discarding the supernatant. Solvent-treated GO was then poured onto a vacuum filter funnel (0.2 μm PTFE filter) and allowed to dry for 5 days. After filtering, the final dried GO film was further dried in a vacuum oven at 40℃ for 48 hrs.

5.2.3. Nitrogen doping of GO films.

Nitrogen-doped reduced GO (NrGO) materials were obtained via the simultaneous thermal reduction and nitrogen incorporation using high-temperature ammonia gas treatment. Dried GO films were placed in an alumina crucible inside a quartz furnace tube. The tube was first vented with UHP Ar gas (100 sccm flow) for 60 minutes. Ammonia gas was then introduced at 60 sccm and the temperature was increased to 850°C at a rate of 1°C/min. The furnace temperature was maintained 850°C for 180 minutes and then slowly cooled to room temperature.

5.2.4. Physical and chemical characterization of GO.

XRD patterns were measured using a Siemens D5000 diffractometer with Cu Kα radiation (1.5418 Å) and a graphite diffracted beam monochromator. The spectra were analyzed using JADE XRD analysis software (Materials Data Inc.). Infrared spectra were obtained using a Fourier-transform infrared spectrometer (Vertex 80,

Bruker) combined with an infrared microscope (Hyperion, Bruker), which is equipped with a 15x objective and a liquid N_2-cooled MCT (mercury-cadmium-telluride) detector. 400 scans with 16 cm^{-1} resolution were averaged for both background and sample spectra. Size of aperture used in transmission measurements was 100 x 100 µm. All measurements were done at room temperature.

The morphology and structural properties were studied using electron microscopy. Scanning electron microscopy (SEM) images were taken at 5 kV with a FEI Quanta 400 ESEM. High-resolution scanning transmission electron microscopy (HR-STEM) images were taken using an aberration corrected Nion STEM (Nion UltraSTEM 200) operated at 60 kV and equipped with Gatan Enfinium dual EELS. XPS measurements were performed using a Kratos Axis Ultra DLD X-ray photoelectron spectrometer with a monochromatic Al Kα source operating at 150 W with no charge compensation. The survey and high-resolution C 1s and N 1s spectra were acquired at pass energies of 80 and 20 eV, respectively. Three areas per sample were analyzed. Data analysis and quantification were performed using the CASAXPS software. A linear background was used for C 1s, N 1s, and O 1s spectra. Quantification utilized sensitivity factors that were provided by the manufacturer. A 70% Gaussian/30% Lorentzian line shape was used for the curve-fits.

5.2.5. Electrochemical characterization

Rotating disc electrode (RDE) measurements of the oxygen reduction reaction were performed in a conventional three-electrode cell at a rotating disk speed of

900 rpm and room temperature using a VMP3 potentiostat (Bio-Logic). The catalyst loading was 0.6 mg cm^{-2}, except for the catalyst loading studies, which ranged from 0.08 to 0.6 mg cm^{-2}. A graphite rod was used as a counter electrode, while an Ag/AgCl (3.0 M NaCl, 0.230 V vs. RHE) was used as a reference electrode. ORR steady-state polarization curves were recorded in an O_2-saturated 0.5 M H_2SO_4 electrolyte with a 30 mV per 30 s potential step.

5.2.6. Modeling of GO structures

The GO system was modeled as a 24.6 Å x 42.6 Å graphene sheet comprised of 400 C atoms with 100 O atoms distributed randomly with 50 on each side of the sheet, thus generating a structure with 25% O coverage. Two such layers are generated and initially separated by 10.8 Å in a 3-D periodic box that is 21.6 Å high generating two inter-GO gallery spaces with the same initial volume. Packmol [130, 131] is used to randomly initialize 100 molecules of water and 2 solvent molecules (in the case of ethanol and ether simulations) in the gallery spaces between GO layers for a total of 200 water molecules and 4 solvent molecules (if included). An equal number of molecules are distributed between layers such that each gallery space has an equal initial solvent density. With an assumed excluded volume due to the GO, the water and solvent combined density is roughly half that of bulk water, representing the "dried" state of each sample.

Simulations of the relaxed structures are obtained through the use of the dispersion/CHONSSi-lg reactive force field potential as implemented in ADF. This force field has graphite as a fitting structure and includes dispersion forces, which makes it a good candidate potential set for studying GO/solvent interactions. Each

initially generated structure model is relaxed for 40 000 MD time steps of 0.25 fs

(total simulated time of 10 ps) using a Velocity Verlet + Berendsen algorithm with

a set temperature of 298 K using the ReaxFF module of the ADF molecular

modeling suite. Longer time relaxations did not significantly change the relaxed

structures. After relaxation, the average spacing as reported in the main text is

calculated by finding the average z component of the C atoms in each layer and

taking the difference between the two averages.

5.3. Results and Discussion

GO is synthesized in aqueous solutions and even "dry" GO films contain a

substantial amount of intercalated water which organizes between the oxygen-

functionalized nanosheets [128, 132-134]. Here we employ a simple solvent drying

technique based on Hansen's solubility parameters to obtain "dry" GO films with

high degree of ORR catalytic activity.
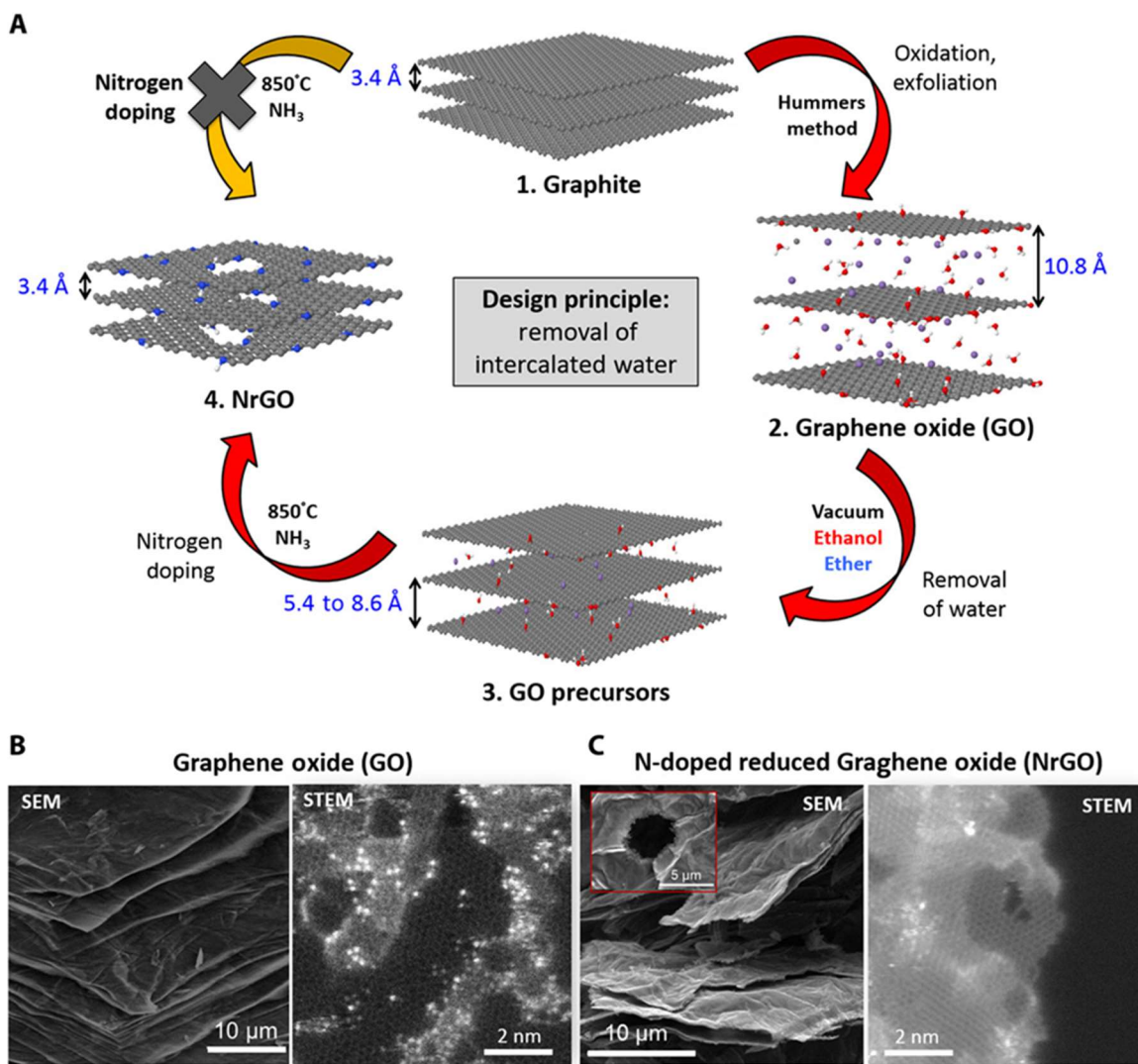
Figure 14: Synthesis of nitrogen-doped reduced GO (NrGO) catalysts.

The drying process is shown in **Figure 14 A**. The process involves rinsing of GO nanosheets with solvents of similar δ_d, but lesser δ_p and δ_H character than water (*e.g.* ethanol and diethyl ether, see **Table 2** for δ values), followed by vacuum drying to obtain compacted, partially reduced GO.

Table 2: Table of Hansen solubility parameters of selected solvents.

Solvent	Dispersion cohesion parameter, δ_d	Polarity cohesion parameter, δ_p	Hydrogen bonding cohesion parameter, δ_H
Water	15.5	16.0	42.3
Ethanol	15.8	8.8	19.4
Diethyl Ether	14.5	2.9	5.1
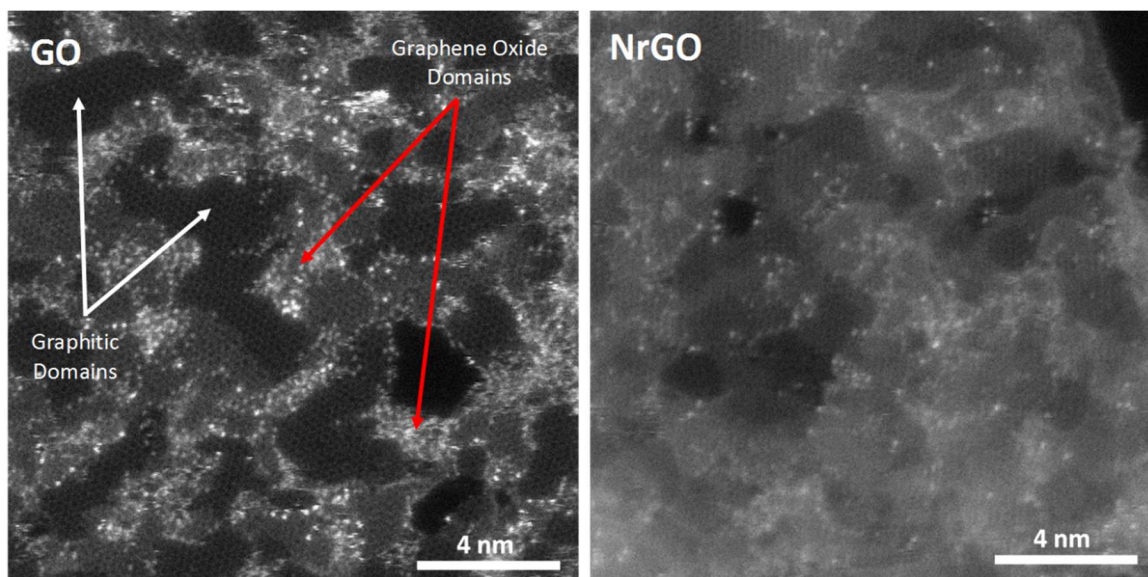
Figure 15: High-resolution STEM images of ether-treated GO and NrGO materials. Highlighting graphitic vs. graphene oxide domains in graphene oxide.

The resulting films are then annealed at 850°C in ammonia to induce nitrogen heteroatoms and simultaneously reduce GO to obtain nitrogen-doped reduced GO (NrGO) (**Figures 14 B** and **14 C).** Scanning transmission electron microscopy (STEM) images of GO (**Figure 14 B** and **14 C**) show the presence of intermixed graphitic (dark region) and functionalized domains (bright), while STEM images of

NrGO (**Figure 14 C** and **Figure 15**) reveal the presence of largely graphitic domains suggesting effective removal of oxygen and formation of sp^2 network [135, 136].
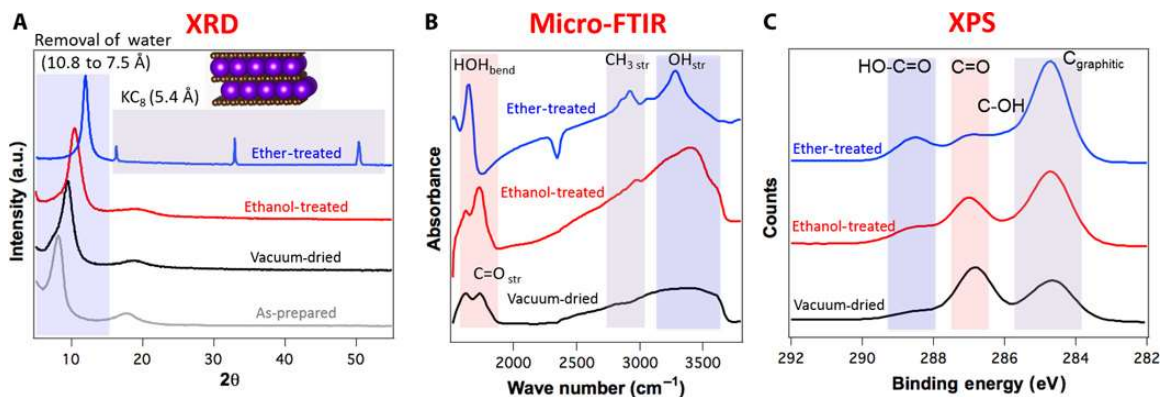
Figure 16: Structural and chemical characterization of solvent-treated GO.

Intercalated water leads to expansion of spacing between the GO nanosheets which can be readily monitored using X-ray diffraction. Exfoliation and functionalization of graphite to graphene oxide increases the interlayer graphene spacing from 3.3 Å to 10.8 Å (**Figure 16 A**), due to the formation of oxygen-containing functional groups on the graphene basal plane and simultaneous intercalation of water (**Figure 17**).
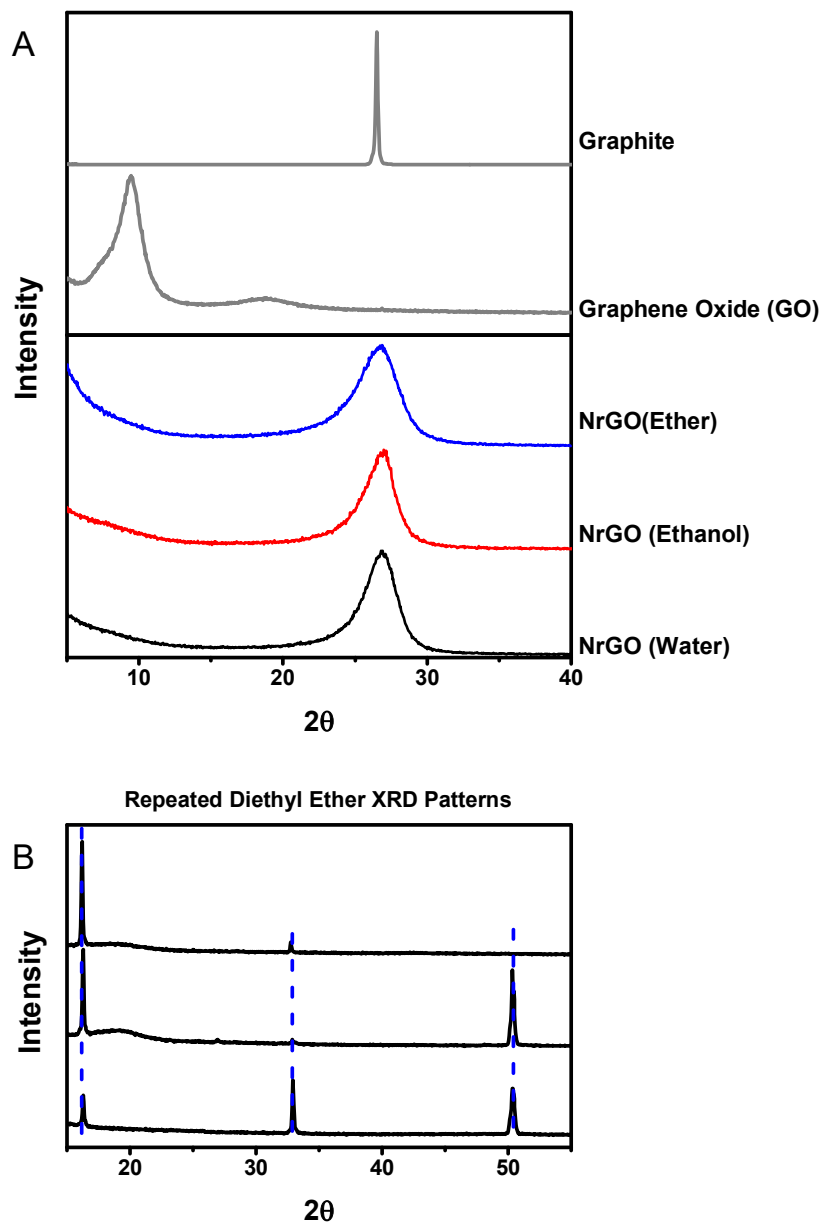
Figure 17: XRD spectra of starting, intermediate, and end products. (A) Graphite, graphene oxide (GO), and nitrogen-doped graphene oxide (NrGO) catalysts and (B) repeated diethyl ether-treated GO precursors.

Removal of water via vacuum drying results in the decrease of d-spacing to 8.6 Å

(**Figure 16 A**). We observed that immersing the as-prepared GO in ethanol or

diethyl ether followed by vacuum drying further decreased the interlayer d-spacing

to 7.8 Å and 7.5 Å, respectively. Thus, solvent drying effectively removes loosely

bound intercalated water from GO. In addition to the decreased interlayer distance, well-defined diffraction peaks appeared at *2θ* values of 16.3º, 32.8º, and 50.3º in the ether-treated GO samples corresponding to a d-spacing of 5.4 Å, with 2nd and 3rd order reflections at 32º and 51º, respectively. The presence of higher order peaks suggest that a significant fraction of the dried GO material possesses substantial long range order [135]. The 5.4 Å spacing in "dry" GO matches exactly that of aqueous free KC_8 [137]. Potassium is most likely intercalated during the synthesis of GO using the modified Hummers method that utilizes potassium permanganate. Further water removal characterization was carried out via thermogravimetric analysis.
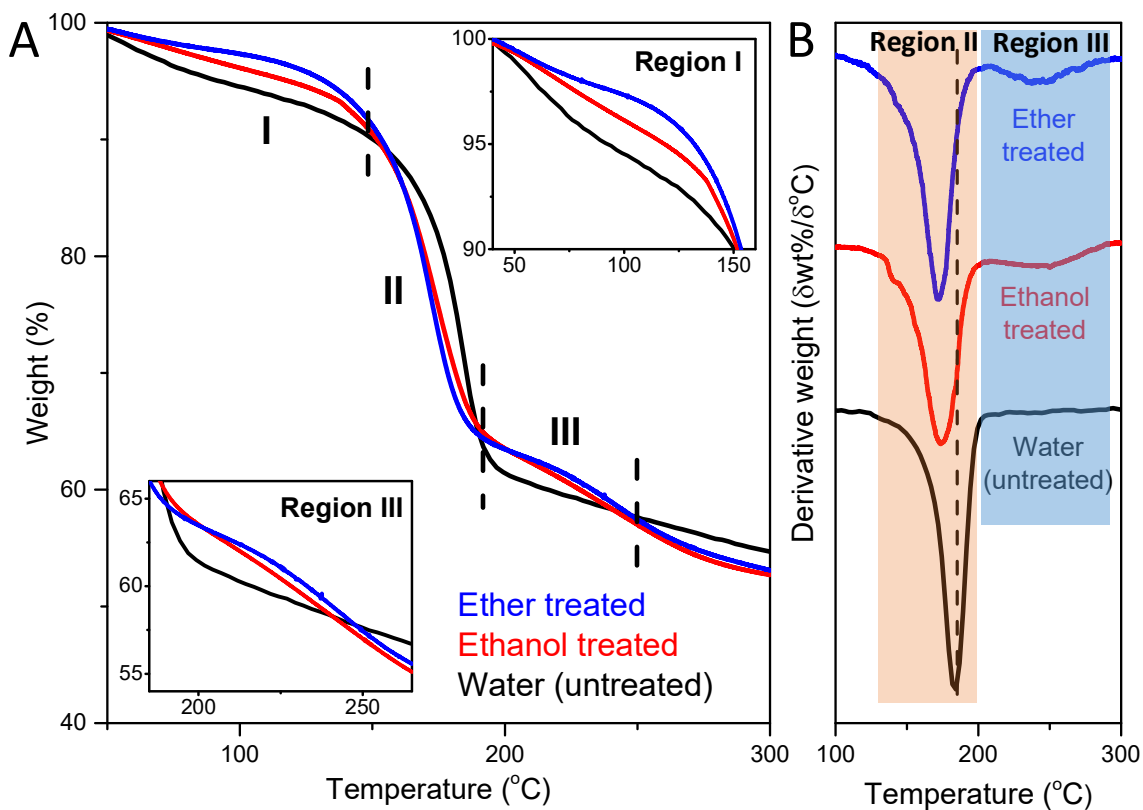
Figure 18: Thermogravimetric analysis (TGA) of solvent treated graphene oxide samples. B, Calculated derivative weight of the TGA curves (δwt.%/δ°C).

Figure 18 shows the weight loss as a function of temperature under a N_2 atmosphere for all GO samples. Few reports have already discussed three main regions of temperature-dependent weight loss for GO [52, 138]. Region I (temperatures below *ca*. 130°C) corresponds to weight loss due to the evaporation of adsorbed water. The greatest weight loss observed for region I was for that of the untreated GO sample (water-untreated) with ca. 8% loss, ethanol-treated showed ca. 6% loss, while ether-treated GO showed the least weight loss at ca. 3% loss; there results are consistent with our observation that solvent treatments results in effective removal of water. Region II ranging from 130°C to 190°C shows the highest change in weight loss. This weight loss has been attributed to the release of trapped CO and CO_2, where intercalated water plays a key role in the formation of gases [52]. Further important comparison for regions I and II are the lower onset (T_{onset}) and maximum rate of weight loss (T_{max}) temperatures observed for ethanol- and ether-treated GO: $T_{onset} \approx 110°C$, $T_{max} \approx 170°C$; while for the untreated GO samples T_{onset} and T_{max} were higher: ca. 130°C and 185°C, respectively. This difference could be attributed to the partially reduced states observed from XPS results (**Figure 16 C**). Region III (190-270°C) is assigned to the reduction of labile oxygen functional groups in GO as well as the removal of strongly bound water, *i.e.* intercalated water [138]. Thus, comparison within region III might give an insight into the differences of intercalated water among all solvent treated GO samples. Untreated GO shows a constant rate change ($\delta wt\%/\delta°C$) once the weight loss reaches 61% as observed from the calculated derivative weight loss shown in **Figure 18 B**. Conversely, ethanol- and ether-treated GOs

show another region of increase in weight loss rate change in region III starting at around 200°C. Acik *et al.* [52] as well as Eigler *et al.* [138] have characterized via infrared and thermogravimetric studies the weight loss process occurring within region III. Their findings indicate the removal of intercalated water via the evolution of CO_2 gas. Thus, the two-step release (region II → region III) of CO and CO_2 gases observed for ethanol- and ether-treated GO samples could possibly be caused by the trapping of intercalated water due to reduced interlayer spacing (XRD, **Figure 16 A**) observed upon solvent treatment. These striking differences in all the three regimes clearly indicate the importance of water removal in graphene oxide and its critical role in the formation of active graphene oxide catalysts upon nitrogen doping.

Micro-FTIR (**Figure 16 B**) and X-ray photoelectron spectroscopy (XPS, **Figure 16 C**) were used to corroborate the XRD observations and further understand the structural and chemical configuration of solvent-treated GO. A broad IR peak extending from ~2500 cm^{-1} to 3700 cm^{-1} is assigned to the combination of C-H and O-H stretching modes for as-prepared GO [57]. Ethanol-treated and vacuum-dried GO shows a slight sharpening of the vibrational modes in the same region. However, IR spectra of GO treated with ether and subsequent vacuum drying displays a well-defined and sharp O-H stretching mode shifted to 3280 cm^{-1}. The shift and sharpness of the peak is consistent with that of confined water, and in fact consistent with the structure of ice (**Figure 19** below) [139-141].
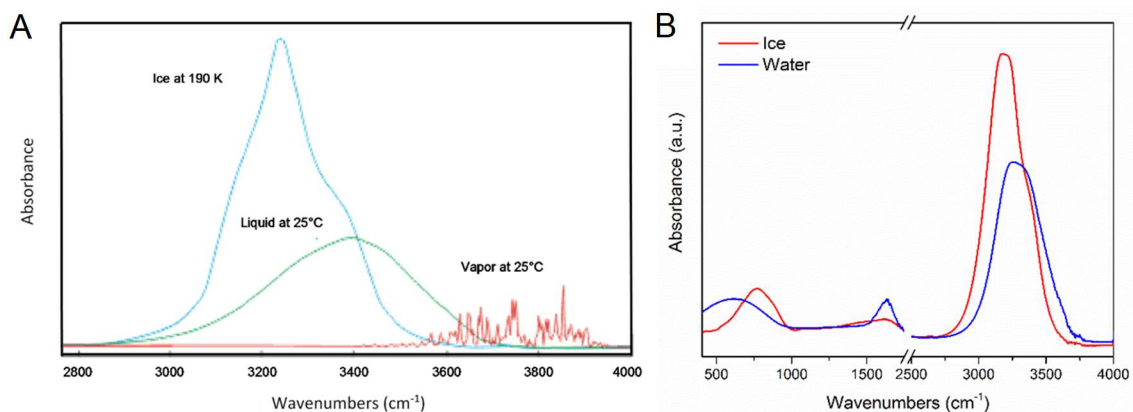
Figure 19: FT-IR ATR spectra of water and ice. (A) Adapted from literature [142] and (B) experimental. O-H stretch vibrations (3000-3800 cm^{-1}), H-O-H bend (~1650 cm^{-1}).

Furthermore, XPS data (**Figure 16 C**) reveals a significant increase in sp^2 C content (284.6 eV), which is correlated to a decrease in C=O fraction (286.8 eV) with decreasing d-spacing in XRD. The C$_{gr}$/C=O ratio increases from 0.8 for vacuum dried GO to 4 for ether-treated/vacuum dried GO (**Figure 16 C** and **Figure 20**).
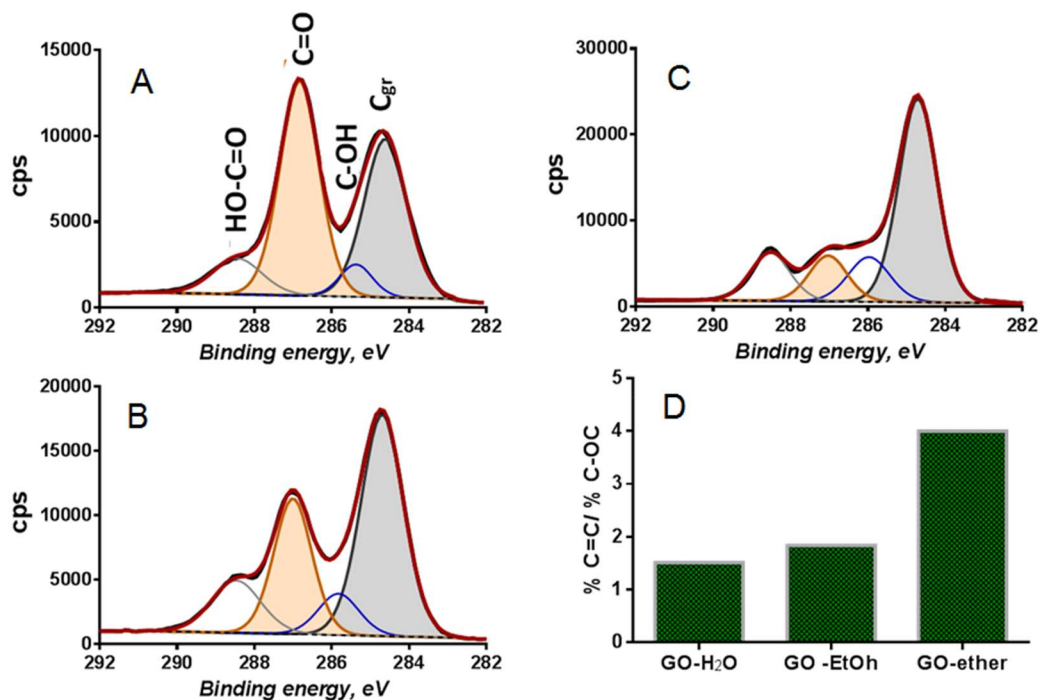
Figure 20: High resolution C 1s XPS spectra for treated GO precursors. A, GO-water, B, GO-ethanol, and C, GO-ether. D, C=C/C-OC ratio from C 1s spectra.

Molecular dynamics models with reactive force field potentials [143, 144] were used to find relaxed GO structures with intercalated water, water with ethanol, and water with ether (**Figure 21**).
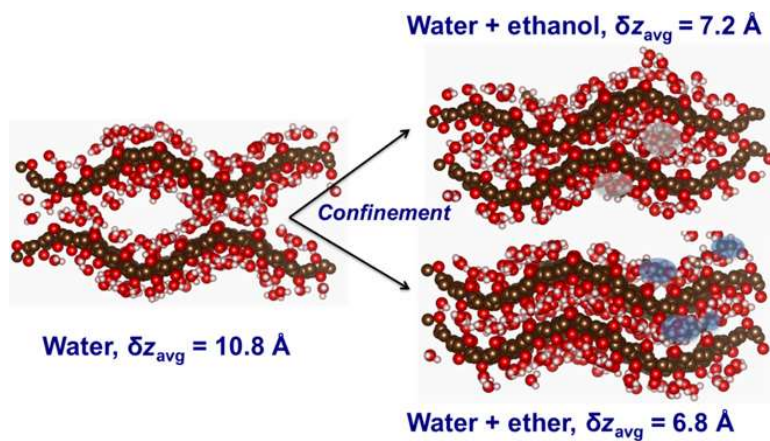
Figure 21: Theoretical models of solvent-treated GO structures.

Molecular dynamics models with reactive force field potentials were previously used to demonstrate the structural and mechanical properties of water intercalated GO. This work suggested that a change in GO functionalization is likely to alter the GO properties via a shift in the hydrogen bonding network. Such a shift is also likely to occur with the addition of a non-water solvent as well. To test this theory, we have utilized similar molecular dynamics models of GO with intercalated water, water with ethanol, and water with diethyl ether and calculated the change in average d-spacing that resulted from inclusion of the solvents.

In the relaxed water and water with ethanol simulations (**Figure 21**), the d-spacing is non-uniform, leading to formation of small pockets that enclose the solvents. However, in the water with ether model, the spacing between layers is fairly uniform. This uniform spacing and the subsequent confinement of water to a 2-dimensional surface that results is a likely explanation for shift in the IR water peak (**Figure 16 B**) observed only in the case of water with ether. Additionally, though not explicitly shown here, the pockets formed in the water and water with ethanol models would likely contain solvated potassium ions left over from the synthesis process (Hummers method) in real materials. In the water with ether model, with no such pockets, the potassium would likely be constrained close to the KC_8 d-spacing leading to the reduction of GO functional groups and formation of KC_8 domains explaining the observed ordered 5.4 Å peak in the XRD data (**Figure 16 A**).

Wrinkling of GO, which has previously been observed via AFM and STM for GO deposited on HOPG [145], was found in all three models. The average d-spacing

values between GO sheets were calculated to be 10.8 Å, 7.2 Å, and 6.8 Å for the water, water with ethanol, and water with ether models, respectively. These values are in good agreement with the decreasing d-spacing trend observed from our experimental XRD data for the respective systems (**Figure 16 A**), supporting our hypothesis that solvents can substantially alter the structure of water-intercalated GO. Further, the symmetric wrinkling phenomenon and the resulting small d-spacing of the graphene planes was found in only the ether-treated GO providing a path to form KC_8 domains in the ether-treated samples.

Nitrogen doping of solvent-rinsed and vacuum dried GO was achieved by high-temperature ammonia treatment, resulting in the formation of nitrogen doped reduced graphene oxide (NrGO) (**Table 3**).

Table 3: Summarized XPS data showing differences in atomic ratio of elements for ether-treated and untreated catalysts.

	Mn 2p (at. %)	C 1s (at. %)	N 1s (at. %)	O 1s (at. %)
NrGO (ether)	0.4	90.5	4.9	4.2
NrGO (untreated)	0.7	89.4	4.5	5.4

Overall, the two-dimensional sheet-like structure of NrGO is preserved after nitrogen incorporation, as seen by SEM (**Figure 23 A**) and STEM (**Figure 14 C** and **Figure 15**). We observed that treatments with ethanol and ether produced NrGO with large (10-20 µm) holes in the graphitic sheets. We hypothesize that the formation of holes might be caused by potassium acting as a pore-forming agent as it sublimes at ca. 759°C (**Figure 22**).
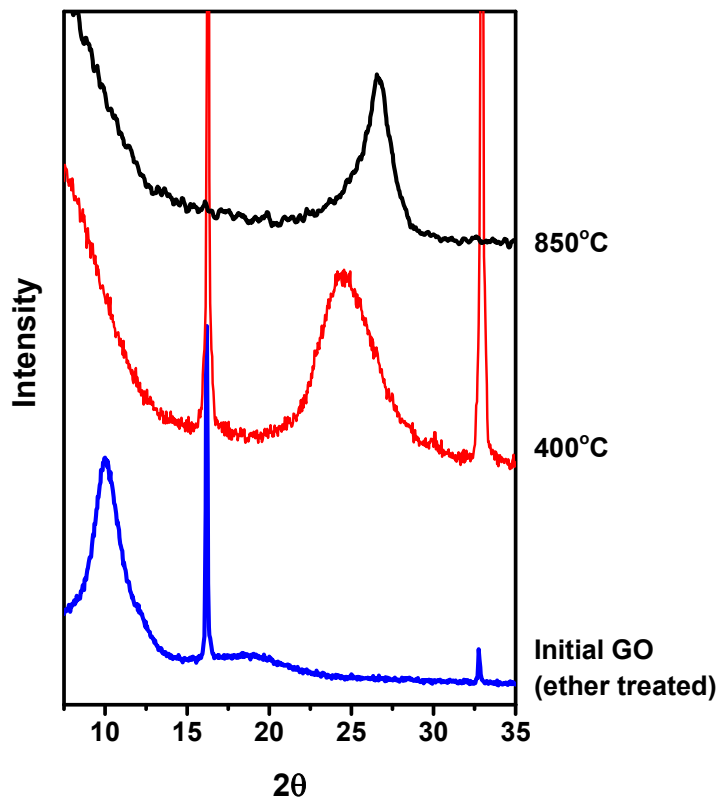
Figure 22: XRD data of ether treated GO showing presence of lamellar KC8 structure at an intermediate temperature (400°C) and disappearing at higher temperature (850°C).

Another possible hypothesis, is related to the confined water molecules. GO structures with decreased d-spacing could prevent water to escape laterally, thus, upon heating evolved trapped gases [146] could form holes perpendicular to the sheets as they escape. The presence of micron-sized holes is beneficial for electrocatalysis because they facilitate transport of reactants and products to and from the active sites throughout the material. Thus, such holey sheets address a significant challenge in using 2D materials for catalysis, *i.e.*, inaccessibility of active sites deep within the layered material.
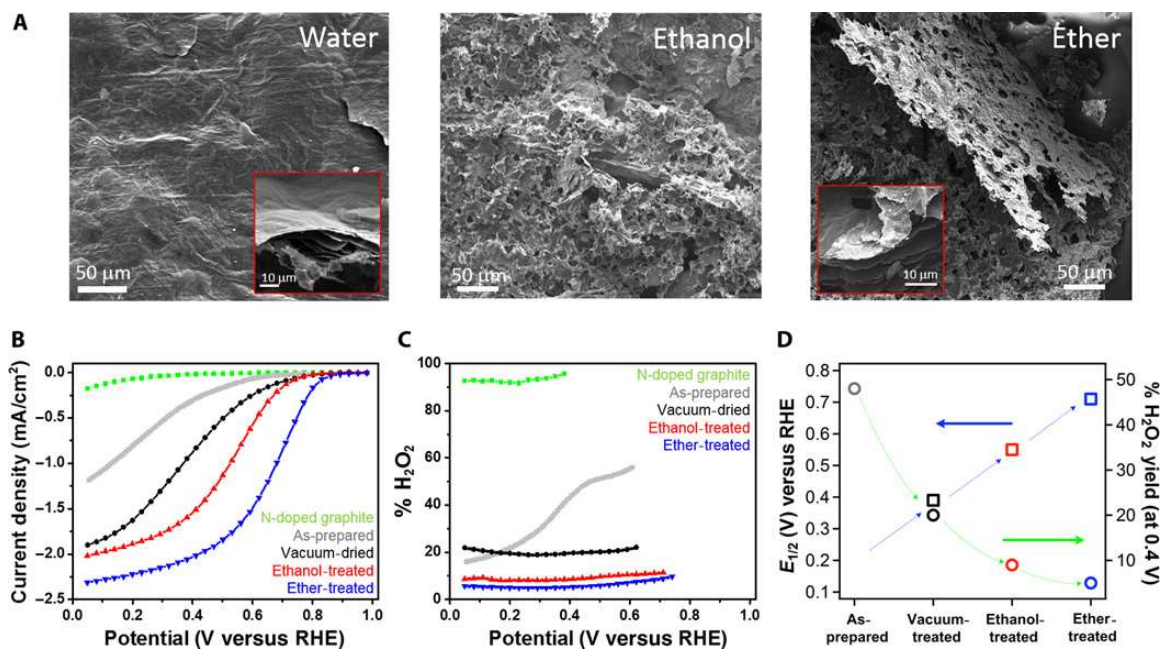
Figure 23: Morphological and electrochemical characterization of NrGO catalysts.

The ORR activity and H_2O_2 yield, as determined by rotating ring-disk electrode (RRDE) of the NrGO catalysts in an acidic electrolyte (0.5 M H_2SO_4), are presented in Figs. 4B-4D. The direct electrochemical reduction of oxygen to water proceeds through a desirable $4e^-$ transfer ($O_2 + 4H^+ + 4e^- \rightarrow H_2O$). However, a less efficient $2e^-$ reaction generating hydrogen peroxide ($O_2 + 2H^+ + 2e^- \rightarrow H_2O_2$) can also occur. Therefore, the ORR performance of a catalyst is not only defined by its activity but also its selectivity for the four-electron reduction of oxygen, and more importantly, its half-wave potential ($E_{1/2}$), which is a descriptor of the limiting current density and onset potential of the catalyst. The thermodynamic reversible potential (E^o) of oxygen reduction at 25ºC is 1.23 V *vs.* the reversible hydrogen electrode (RHE). Any additional potential required to drive the ORR is called the overpotential (η). Well-performing ORR catalysts are characterized by low η, high $E_{1/2}$, and high selectivity values for $4e^-$ transfer. In this work, the as-prepared NrGO catalysts

(without solvent or drying pre-treatments) showed a high ORR η value of 0.43 V in acidic media. This low activity was accompanied by poor four-electron selectivity, with H_2O_2 yield values greater than 50% across the studied range of electrode potentials (**Figure 23 C**). NrGO catalysts prepared from vacuum and solvent-treated samples showed much improved ORR performance, as indicated by a decrease in η, increase in $E_{1/2}$, and decrease in peroxide yield (**Figures 23 B-D**). Ether-treated GO, characterized by a long-range order and decreased d-spacing, was found to be the best oxygen reduction catalyst, with η of 0.33 V, estimated $E_{1/2}$ of 0.71 V, and selectivity for the four-electron reduction of oxygen of *ca.* 95% (5% H_2O_2 yield). **Figure 23 D** summarizes our findings highlighting the importance of the solvent-treatment process for the development of high-performing ORR GO catalysts: a 300 mV increase in $E_{1/2}$ from *ca.* 0.4 V for the vacuum dried catalyst to *ca.* 0.7 V for the ether treated catalyst, and a corresponding increase in $4e^-$ transfer selectivity from about 50% to *ca.* 95%. These results demonstrate the highest ORR activity reported to date for a NrGO electrocatalysts in acidic media. Further, a reference material, namely nitrogen-doped graphite, which showed extremely poor ORR activity demonstrate the advantage of the process developed in this work for the synthesis of active ORR GO catalysts **(Figures 23 B-C)**.
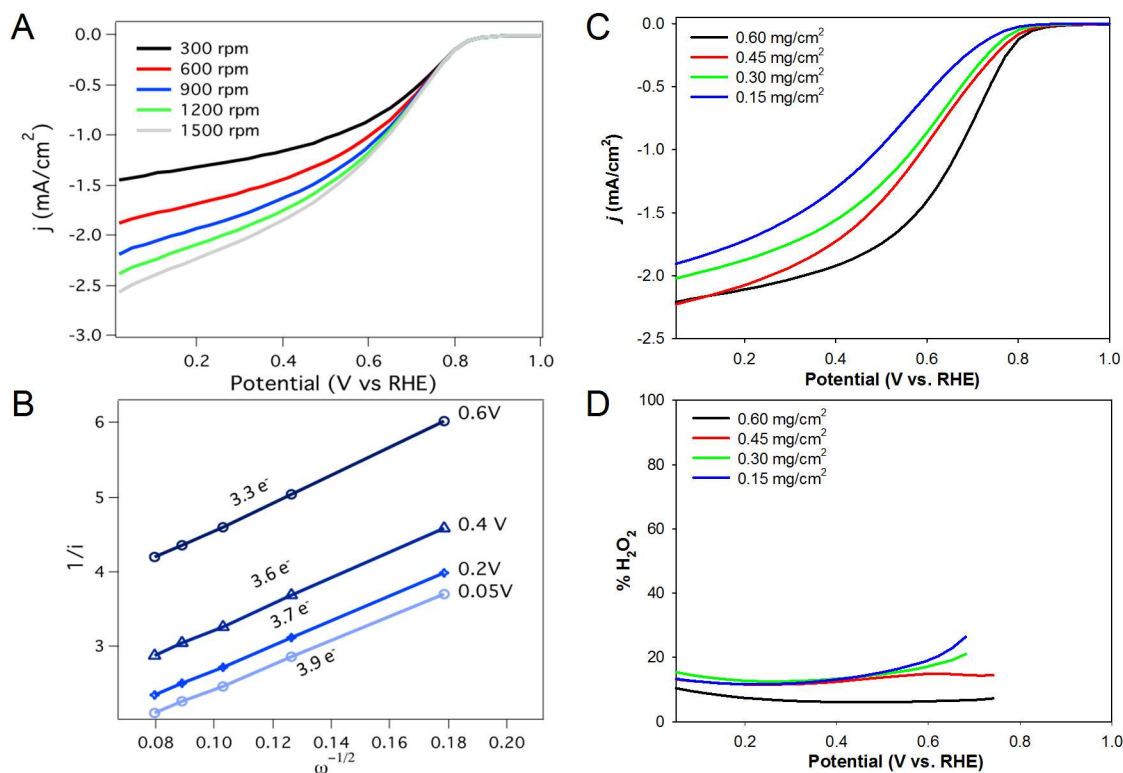
Figure 24: Koutecky-Levich and electrode loading mechanistic studies for ether-treated NrGO catalyst. Koutecky-Levich: A, Steady-state step voltammograms at different rotation speeds and B, corresponding Koutecky-Levich plot. Electrode loading studies: C, Steady-state step voltammograms at different electrode loadings and D, corresponding H_2O_2 yields.

Additional information on the ORR mechanism on ether-treated NrGO was obtained from dependence of the oxygen-reduction current on RRDE rotation rate (Koutecky-Levich relationship) and catalyst loading studies (**Figure 24**). These studies confirm the predominance of the 4e⁻ transfer in the potential range 0-0.6 V (*vs.* RHE). Determination of the active site for graphitic ORR electrocatalysts remains a conundrum. Although transition metal impurities inherent from the GO synthesis process [147] were identified from XPS analysis, these impurities were present regardless of the solvent treatment indicating that the structural and

chemical differences arising from solvent treatments are primarily responsible for the improved catalytic activity.
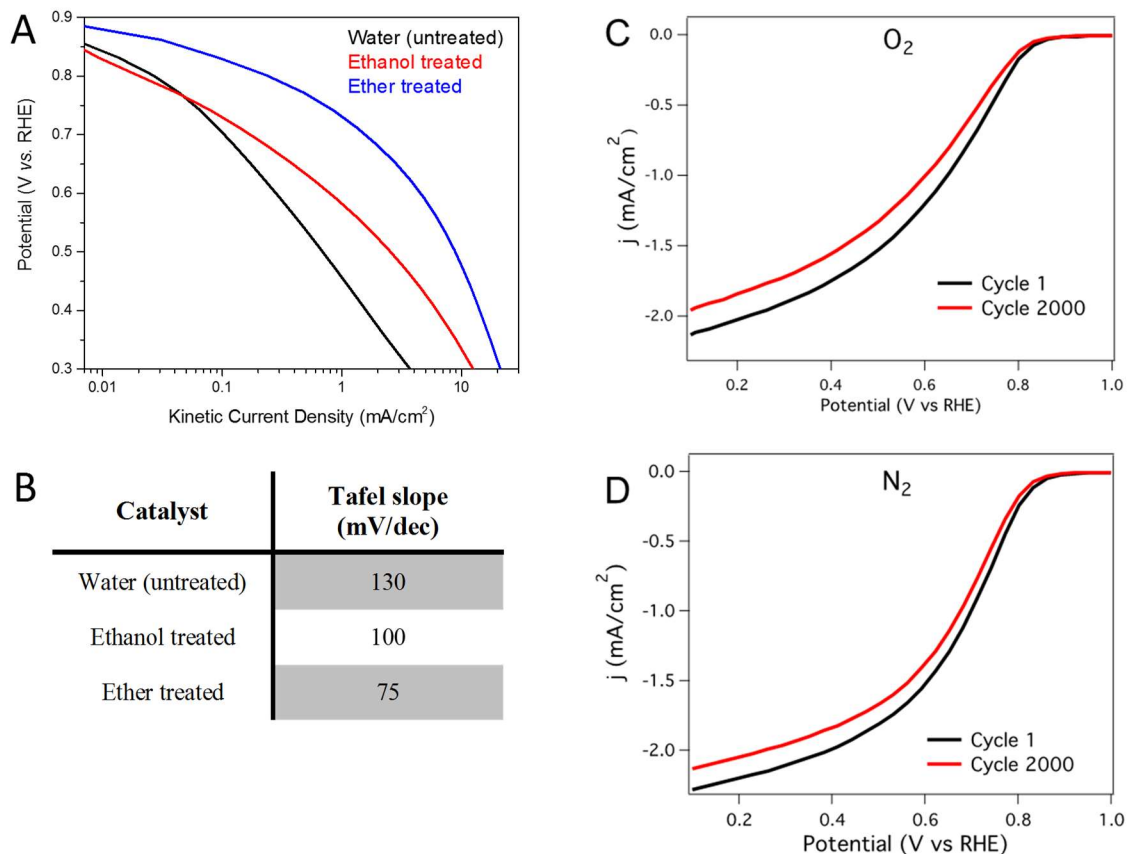
Figure 25: Tafel and accelerated durability studies for the ORR on NrGO electrocatalysts. (A) Tafel plots obtained from diffusion-corrected kinetic current densities. (B) Summarized Tafel slopes for all NrGO electrocatalysts. Accelerated durability studies of ether-treated NrGO electrocatalyst under (C) O_2 and (D) N_2 saturated electrolyte.

Lastly, accelerated durability testing showed less than 5% loss in the $E_{\frac{1}{2}}$ value in both N_2- and O_2-saturated solutions after 2000 cycles (**Figure 25**).
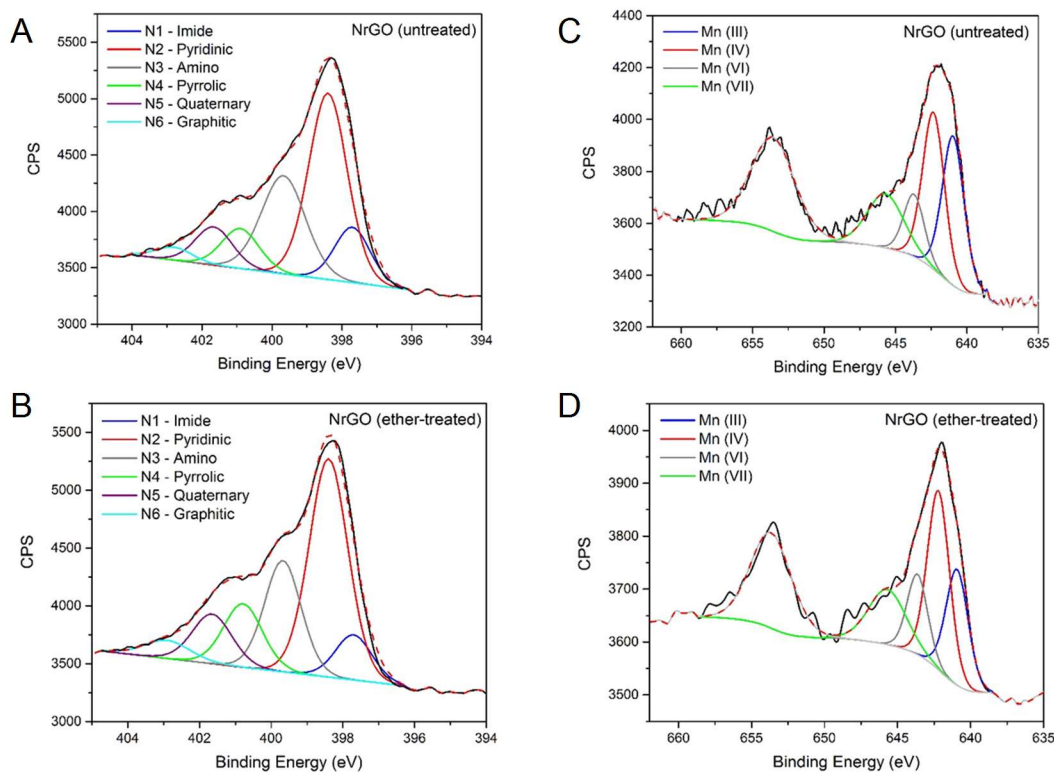
Figure 26: High resolution XPS N 1s and Mn 2p spectra for ether-treated and untreated NrGO catalysts. A-B, N 1s spectra with six peaks fitted with the same shape and constrained FWHM and C-D, Mn 2p spectra comparing differences observed between ether treated and untreated NrGO catalysts.

Table 4: Summarized XPS data showing differences in C and N speciation for ether-treated and untreated catalysts.

	C_{gr} (%)	C-N (%)	C-O (%)	C=O (%)	COOH (%)	C_{sh} (%)	N_{Imine} (%)	N_{Pyrid} (%)	N_{Amin} (%)	N_{Pyrr} (%)	N_{Quat} (%)	N_{Graph} (%)
NrGO (ether)	74.3	10.4	6.8	3.7	2.3	2.4	8.7	42.8	21.1	13.3	10.1	4.0
NrGO (untreated)	71.7	10.1	7.7	5.3	2.5	2.7	10.9	43.3	25.1	8.7	9.0	3.1

Table 5: Summarized calculated BET specific surface areas and pore volumes obtained from solvent treated NrGO catalysts.

Catalyst	BET surface area (m²/g)	Pore volume (cc/g)
Water (untreated)	122	0.16
Ethanol treated	373	0.23
Ether treated	453	0.28

Elemental analysis using XPS also showed negligible differences among NrGO catalysts after 2000 cycles (**Figure 26** and **Tables 4** and **5**).

5.4. Conclusion

In summary, we demonstrate active graphene oxide catalysts for ORR in acidic conditions through the application of simple solvent drying strategies. These strategies facilitate the efficient removal of the trapped water within the graphitic sheets, which in turn allows for controlling the macroscopic structure and morphology of electrocatalysts upon nitrogen doping. Further advances in catalytic performance from carbon-based catalysts should be obtainable by varying the polarity, miscibility, and wetting properties of solvents, as well as by developing new aqueous-free approaches. The fundamental understanding obtained from our studies should have the potential to establish the design rules for graphene and other related materials such as transition metal dichalcogenides (TMDs) and transition metal oxides.

6. A Novel Solvent Treatment for Improved ORR Activity of Nitrogen-doped Graphene Oxide Electrocatalysts

6.1. Introduction

Development of novel electrocatalysts for the oxygen reduction reaction (ORR) is crucial for a number of energy conversion and storage devices, namely metal-air batteries and fuel cells.[98-101] Many applications, *e.g.*, fuel cells for transportation, operate under highly acidic conditions, and depend on precious metal catalysts, like platinum, for both anode and cathode reactions. Conversely, State-of-the-art ORR electrocatalysts are Pt-based catalysts[6, 148]; however, their high cost and scarcity is partly responsible for the limited commercialization of, in particular, fuel cell technologies. Consequently, platinum group metal-free (PGM-free) catalysts have recently been developed as a more affordable and sustainable alternative. The motivation for studying these electrocatalysts at high pH comes from the many advantages that alkaline fuel cells (AFC) offer: alkaline conditions permit for the use of alternative non-precious metal electrocatalyts which are not only active but have been shown to perform as well or better than platinum[2, 3]. Additionally, AFC allow the use of cheaper materials for fuel cell stacks and a wide choice of fuel (H_2, hydrazine hydrate[4, 5], *etc.*).

In alkaline environments, the ORR can proceed via a two- or four-electron pathway according to the following reactions:

$$O_2 + 2H_2O + 4e^- \rightarrow 4OH^- \qquad (5)$$

$$O_2 + H_2O + 2e^- \rightarrow HO_2^- + OH^- \qquad (6)$$

$$HO_2^- + H_2O + 2e^- \rightarrow 3OH^- \qquad (7)$$
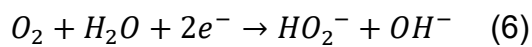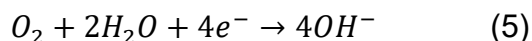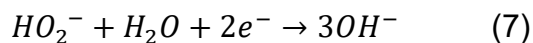
The direct four-electron reduction pathway is described by **Equation (5)**. Alternatively, O_2 can be reduced via a two-electron reaction (**Equation (6)**) producing the hydroperoxyl radical HO_2^-. Hydroperoxyl radicals are undesired as they are known to negatively affect membrane durability.[149-151] Nevertheless, it is possible to further reduce HO_2^- to OH^- according to **Equation (7)**. Hence, the successful development of highly selective catalysts, is critical for the understanding of the reduction mechanism leading either to OH^- or HO_2^- formation.

Many of the best performing PGM-free electrocatalysts have traditionally been synthesized by pyrolysis of metal and nitrogen containing precursors with porous carbons[23, 25-30, 90-92, 106, 107, 127]. However, despite the great improvements in ORR activity that have been achieved with PGM-free catalysts, the exact nature of the active site(s) remains the subject of intense investigation in the field[2, 31-35]. Further, a problem often encountered with PGM-free catalysts is their durability.

In fact, advanced spectroscopic techniques such as Raman spectroscopy and XPS were used to better understand the nature of the active site in order to improve their activity and durability[152]. Nevertheless, many of the PGM-free catalyst synthesis strategies result in materials with morphologically complex N-doped graphitic structures increasing the challenge of identifying the nature of the active site. Therefore, functionalized graphene, which is also known to be ORR active,[59, 81-87] represents a relatively simple class of materials that can be used

as a model system to mimic many of the structural and functional properties found in the more complex and high performing PGM-free catalysts.

In this paper, we have developed highly selective nitrogen-doped graphene oxide materials towards the ORR using solvent engineering and electrochemical methodology. The conventional approach to synthesize resilient nitrogen-doped graphitic catalysts involve the exfoliation and functionalization of graphite using strong oxidizing agents[42, 43], which facilitate nitrogen incorporation, typically by high-temperature treatment in an ammonia gas environment achieving between 3 to 6 atomic percent nitrogen doping[59]. However, the ORR activity of nitrogen-doped graphene oxide catalysts is lower than conventional nitrogen-doped mesoporous carbons. This behavior is due to number of factors including fewer numbers of active sites on the graphitic basal plane and the re-stacking of N-doped graphitic sheets, which forms a tightly packed film that limits the diffusion of reactants to the active sites, and a mixture of electron transfer mechanisms. Therefore, the aim of this work is to induce primarily four-electron transfer sites in functionalized graphene catalysts via solvent engineering. Solvent treatment on graphene oxide modifies the morphology of graphitic structures drastically while retaining their desired structural and electrical conductivity properties. Depending upon the solvents used, the catalysts exhibit a substantial change in morphology either by formation of holes that leads to edge defects, and enhances oxygen diffusion, or by inducing 3D structure to graphitic sheets that promote ORR. These morphological changes address the key challenges of enhancement of four-electron active sites as well as promote diffusion of reactants and products.

Secondly, post voltammetry cycling of the catalysts results in selective suppression of two-electron sites, generating a highly selective four-electron pathway catalyst. The results described in this paper provide design principles for synthesis of high performing graphitic ORR electrocatalysts as well as supports with controlled activity. Ultimately, this work provides a better understanding of the active site formation and reaction mechanism in alkaline medium that is a crucial step in developing superior catalysts.

6.2. Materials and Methods

6.2.1. Synthesis of graphene oxide

Graphene oxide (GO) was synthesized using a modified Hummers method. 5g of graphite (Sigma Aldrich) were mixed in 750 mL of concentrated sulfuric acid (98% H_2SO_4) using a magnetic stirrer. A total of 25 g of potassium permanganate, used as an oxidizing agent, were added to the solution over the period of 5 days (5g per day) while continuously stirring. The solution was placed in an ice bath and 750 mL of ice cold deionized water was slowly added to the solution. Approximately 5 mL of 30% H_2O_2 was slowly added to the mixture until it turned yellow. The mixture was left to stir vigorously for 48 hours. The slurry was then centrifuged at 5000 r.p.m. during 2 hours. The supernatant was decanted and the GO was re-dispersed in 0.5 M HCl. This washing step was repeated once with 0.5 M HCl and twice with deionized water. The obtained GO was dispersed one last time in deionized water.

6.2.2. Solvent treatment of GO

GO was centrifuged at 10000 r.p.m. for 2 hours to remove the excess of water. The obtained GO aliquot was washed with 30 mL of solvent and dispersed using a vortex mixer. The GO-solvent dispersion was then centrifuged to remove the excess solvent and filtered using a vacuum filtration funnel (0.2 µm PTFE filter). After 5 days, the dried GO film was put in a vacuum oven at 40℃ for 48 hours for complete removal of solvents.

6.2.3. Nitrogen doping of GO films

Nitrogen-doped GO (NrGO) was obtained by simultaneously reducing the catalyst while incorporating nitrogen in the system in a high temperature ammonia atmosphere. GO films were placed in a ceramic crucible within a quartz furnace tube. The tube was first purged with UHP Ar (100 sccm flow) for 60 minutes and then ammonia was introduced at 60 sccm while temperature was increased at 850°C at a rate of 1°C/min. The temperature was maintained at 850°C for 3 hours and slowly cooled down to room temperature.

6.2.4. Physical characterization

XRD spectra were obtained using a Siemens D5000 diffractometer with Cu Kα radiation (1.5418 Å) and a graphite diffracted beam monochromator. The spectra were analyzed using JADE XRD analysis software (Materials Data Inc.). All measurements were done at room temperature. The structure and the morphology were studied using electron microscopy. Scanning electron microscopy (SEM) images were taken at 5 kV with a FEI Quanta 400 ESEM.

Digital image processing of images was done in Matlab. Overall porosity (ratio of void area (pores) to total area) was calculated from thresholded images and average surface roughness Ra was calculated from the original gray scale intensity.

XPS spectra were obtained using a Kratos AXIS Ultra photoelectron spectrometer using a monochromatic Al Ka source operating at 300 W. An initial survey was completed prior to the acquisition of high resolution spectra of C1s, O1s, and N1s for all samples. The data shown are an average of 1-2 samples at 3-4 areas per sample.

The contact angle experiment was conducted at room temperature using a CAM-PLUS Contact Angle Meter. Contact angles were measured on NrGO substrates placed on a slicon wafer using a single 3 µl droplet of ultrapure water.

6.2.5. Electrochemical characterization

Rotating ring disc electrode (RRDE) measurements of the oxygen reduction reaction were performed in a conventional three-electrode cell at a rotating disk speed of 900 r.p.m. and room temperature using a VMP3 potentiostat (Bio-Logic). The catalyst loading was 0.6 mg cm^{-2}. A platinum wire was used as a counter electrode, while an Hg/HgO (1.0 M KOH, 0.880 V *vs*. RHE) was used as a reference electrode. ORR steady-state polarization curves were recorded in an O$_2$-saturated 0.1 M NaOH electrolyte with a 30 mV per 30 seconds potential step. The Platinum ring was held at a constant potential of 1.3 V *vs.* RHE.

Chronoamperometry measurements were performed in a N_2-saturated 0.1 M NaOH electrolyte. The reduction of peroxide radicals was shown by introducing 1 mMol of 30% H_2O_2 solution. The rate of consumption of peroxide radicals was calculated after 15 minutes of equilibration over a period of 12 minutes.

6.3. Results and Discussion
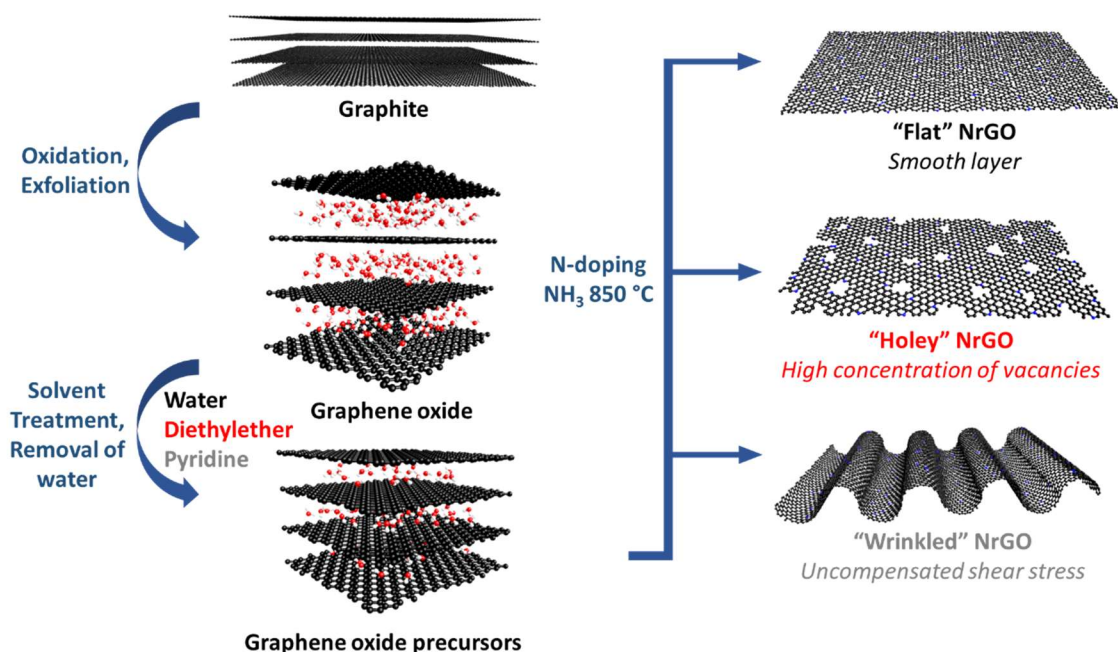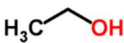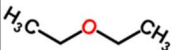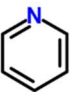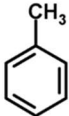
Figure 27: Schematic of synthesis process. Graphite is (i) exfoliated and oxidized into graphene oxide, (ii) treated with different solvents and dried before (iii) nitrogen doping in reactive ammonia atmosphere at high temperature (850°C). The resulting morphology of the final catalyst is dependent on the solvent used.

The solvent-engineered process and electrochemical approach to achieve selective four-electron transfer electrocatalysts is shown in **Figure 27**. Graphite, a compact stack of sp^2 hybridized carbon sheets with an interplanar distance of 3.4 Å is oxidized via a modified Hummers method[43, 96] to form graphene oxide (GO). The resulting GO nanosheets are suspended in water. Specifically, GO

nanosheets are then exposed to different solvents with various solubility parameters, *i.e.* Hansen solubility parameters. Structurally, the solvents utilized for this study are divided into two groups: non-cyclic—water, ethanol, diethyl ether; and cyclic—pyridine and toluene.

A

Structure of solvents				
Non-cyclic			Cyclic	
Water	Ethanol	Diethyl ether	Pyridine	Toluene
H_2O	H_3C—OH	H_3C—O—CH_3		CH_3

B

Solvent	Formula	Dispersion cohesion parameter, δd	Polarity cohesion parameter, δp	Hydrogen bonding cohesion parameter, δH	Solubility in H_2O (g/100g)	Boiling point (°C)
Water	H_2O	15.5	16	42.3	M	100
Ethanol	C_2H_5OH	15.8	8.8	19.4	M	78.5
Diethyl Ether	$C_4H_{10}O$	14.5	2.9	5.1	7.5	34.5
Pyridine	C_5H_5N	19	8.8	5.9	M	115.2
Toluene	C_7H_8	18	1.4	2	0.05	110.6

Figure 28: solvent properties. (A) Structure of the organic solvents used for the treatment of NrGO precursors. (B) Hansen's solubility parameters and boiling point of the organic solvents.

Their structures and solubility properties are summarized in **Figure 28** above. It is important to note that although GO has been previously dispersed in organic solvents[49, 50], their effect on structure and properties had not been completely explored[87]. Critical solvent properties investigated here include Hansen's solubility parameters (dispersion, δ_d, hydrogen bonding, δ_H, and polarity, δ_p), water miscibility, and boiling point. These properties are important to consider because the GO nanosheets are predominantly solvated by H_2O molecules, which will affect their interaction with other solvents. The dispersion parameter for all solvents

studied is similar; however, their hydrogen bonding and polarity parameters vary significantly. Moreover, the miscibility of each solvent in water also varies; while ethanol and pyridine are miscible in water, diethyl ether and toluene are only partially miscible. Following solvent treatment, GO catalyst precursors were subjected to vacuum drying.

The solvent treatment results in varying the interplanar distance between the vacuum dried GO sheets (**Figure 29**). The vacuum dried GO sheets are subjected to high-temperature ammonia treatment (850 °C), resulting in active nitrogen-doped reduced-graphene oxide (NrGO) electrocatalysts.
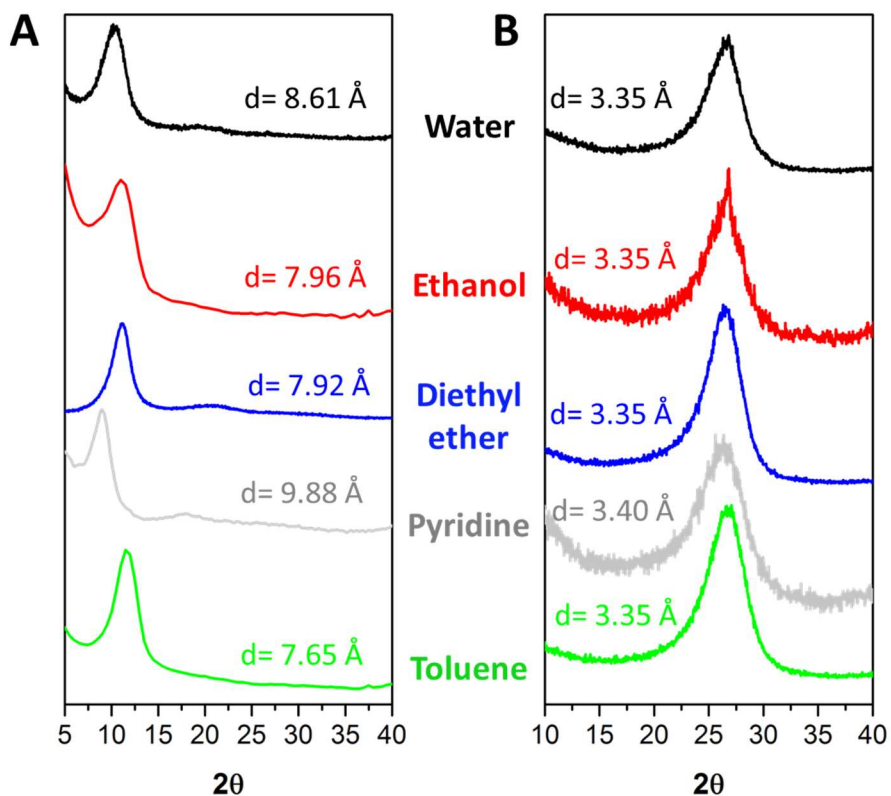
Figure 29: XRD pattern of (A) GO precursors and (B) NrGO catalysts treated with selected organic.

Structural and functional characterization on the NrGO electrocatalysts was performed using a number of different techniques including: X-ray diffraction (XRD), X-ray photoelectron spectroscopy (XPS), Raman spectroscopy, and electron microscopy (SEM). The summary results of the XRD analyses for GO precursors and NrGO catalysts are shown in **Table 6** and **7** below.

Table 6: Analysis of crystallite size, lattice strain and d-spacing of the solvent treated GO precursors.

Parameters	Water	Ethanol	Diethyl ether	Pyridine	Toluene
Peak position	10.27	11.11	11.17	8.95	11.57
FWHM	3.27	3.97	2.36	2.66	3.13
Crystallite size / nm	2.55	2.1	3.54	3.13	2.67
d-spacing / Å	8.61	7.96	7.92	9.88	7.65

Table 7: Analysis of crystallite size, lattice strain and d-spacing spacing of the solvent treated NrGO electrocatalysts.

Parameters	Water	Ethanol	Diethyl ether	Pyridine	Toluene
Peak position	26.61	26.61	26.61	26.21	26.61
FWHM	4.06	4.11	3.79	4.89	3.95
Crystallite size / nm	2.1	2.08	2.25	1.74	2.16
d-spacing / Å	3.35	3.35	3.35	3.4	3.35
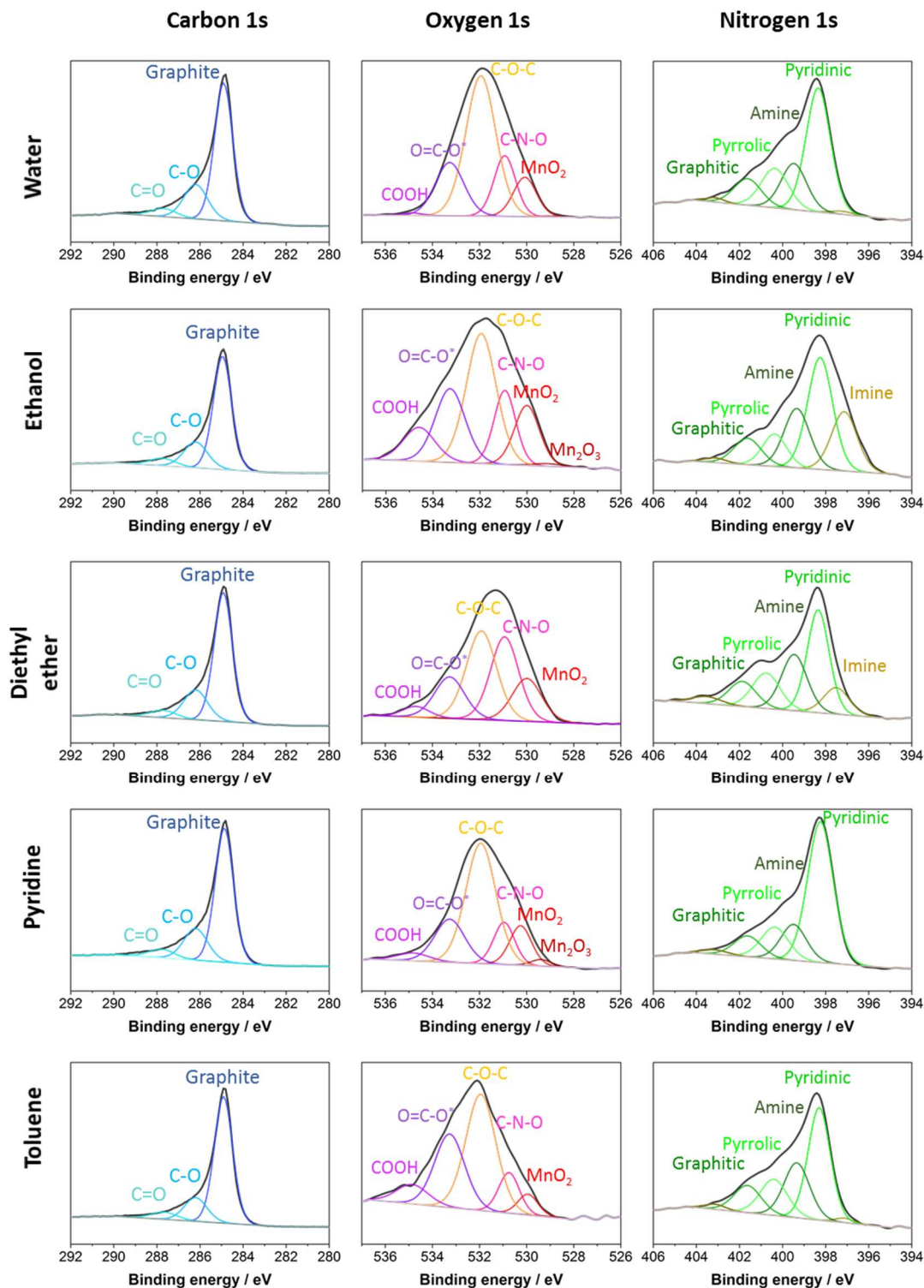
Figure 30: Experimental fit performed on Carbon 1s, Oxygen 1s and Nitrogen 1s of nitrogen-doped GO precursors treated with selected organic solvents.

Surprisingly, both XRD (**Figure 29**, **Tables 6** and **7**) and XPS (**Figure 30**) revealed only minor differences in the structure and the functional groups among the samples, whereas electrochemical activity towards ORR was drastically different. Specifically, XRD patterns indicate minimal differences in the solvent treated samples with all catalysts exhibiting a broad graphitic peak at 26° with a d-spacing of 3.4 Å, which is indicative of a very defective graphitic structure[153] (**Figure 29**, **Tables 6** and **7**).

XPS spectra show a similar C 1s spectrum (**Figure 30**), i.e., predominantly graphitic carbon (284.7 eV) with some presence of C-O (286.3 eV) and C=O species (286.3 and 287.8 eV). N 1s spectra shown in **Figure 30** show the presence of pyridinic, amine, pyrrolic, and graphitic nitrogen (respectively, 398.5 eV, 399.5 eV and 400.5 eV) along with graphitic amine groups nitrogen (401.8 eV). The pyridine and ethanol treated samples have slightly higher concentration of nitride edge sites such as imines or nitriles (397.4 eV) as shown in **Figure 30**. The total nitrogen content of all NrGO catalysts varies between 5 and 7 atomic % (**Figure 31**).
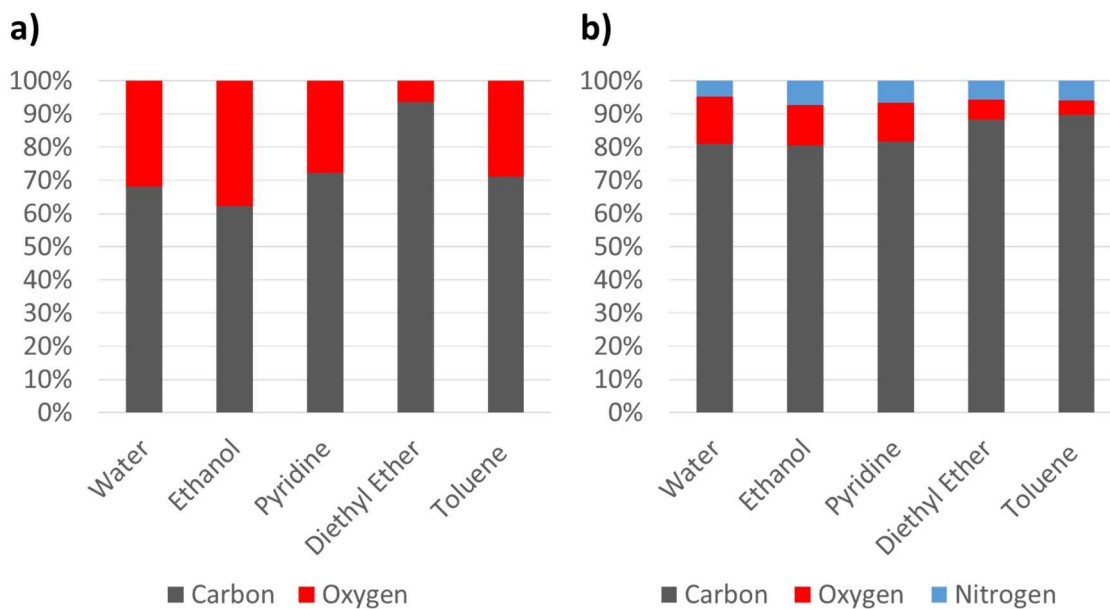
Figure 31: Elemental composition of a) GO precursors and b) NrGO catalysts treated with selected organic solvents.

Raman spectroscopy performed on water, diethyl ether and pyridine-treated samples is shown in **Figure 32**.
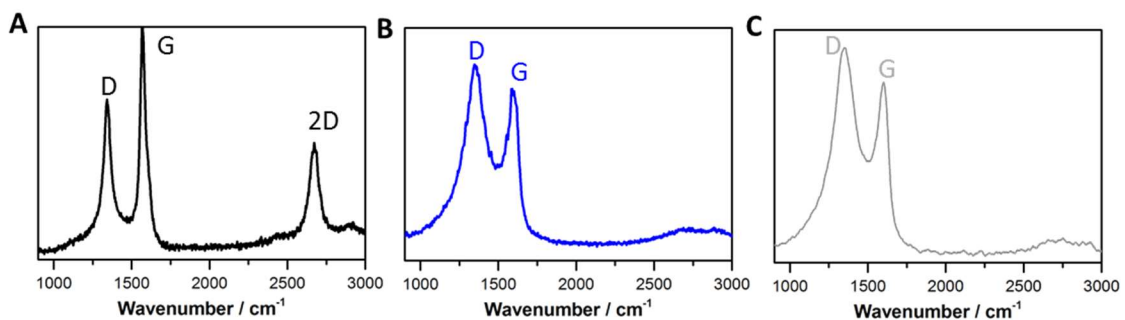
Figure 32: Raman spectra of the best performing N-doped GO precursors treated with selected organic solvents. (a) Water; (b) diethyl ether; (c) pyridine.

All spectra show the presence of a peak at 1300-1400 cm^{-1} corresponding to the D-band, the disorder-induced band, as well as a peak at 1560-1600 cm^{-1} corresponding to the G-band, originating from graphite like sp^2 hybridization of

carbon. Additionally, the water treated sample shows a strong peak at 2670 cm^{-1}

corresponding to the 2D band whereas the same peak is weakened for the diethyl

ether and pyridine treated samples. The weakened 2D peak and enhanced D peak

for the NrGO obtained from aqueous solvent are specific to single-layered reduced

graphene oxide. [154]-[155] Solvent-engineered NrGO samples have Raman

signatures specific to disordered, defected, multilayered graphene as manifested

by a change in ratio of D/G with an increased D-band width and disappearance of

2D peak, when compared to NrGO obtained from aqueous solvent. The ratio of

D/G peak was also enhanced with solvent engineering, indicating a defective

lattice structure.

While there were few differences among the materials observed in the XRD and

XPS spectra, significant morphological differences were consistently observed in

the SEM images of NrGO samples that varied based on GO solvent treatment

(**Figure 33**).
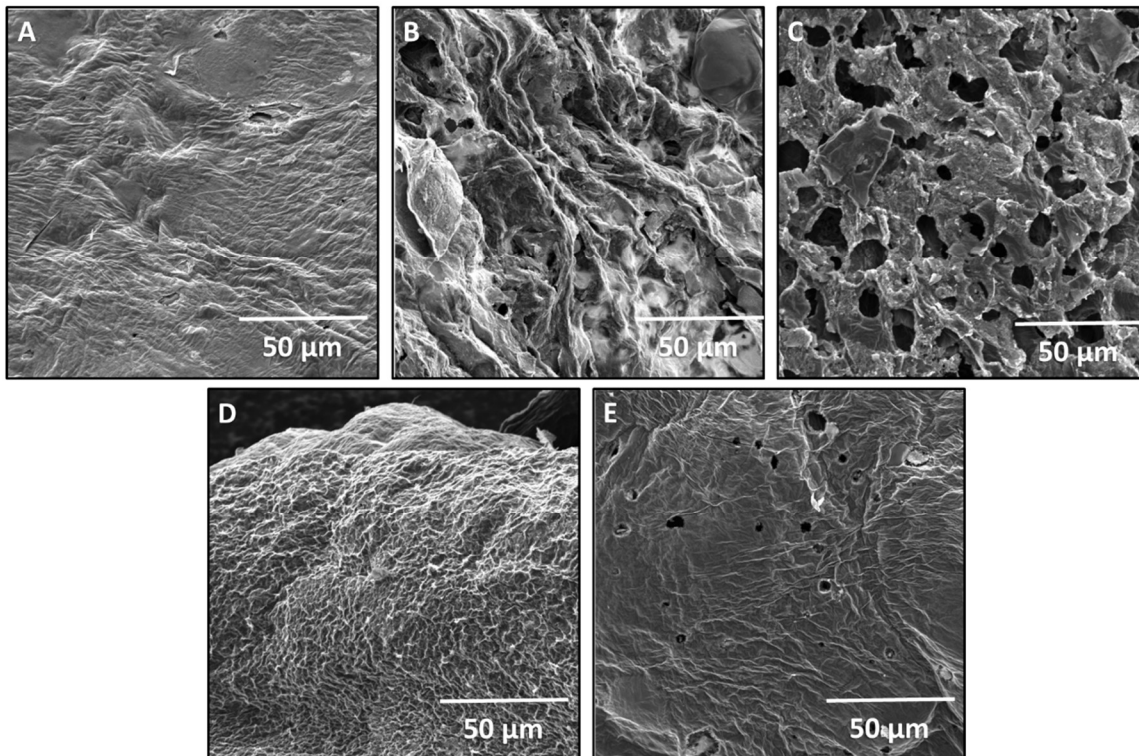
Figure 33: SEM images of nitrogen-doped GO precursors treated with selected organic solvents. (A) Water. (B) Ethanol. (C) Diethyl ether. (D) Pyridine. (E) Toluene.

The water treated sample shows a smooth surface with very few edges exposed or defects. The ethanol treated sample shows a rough and wrinkled surface, exposing edges as well as a few holes ranging from 2 to 10 μm in diameter (**Figure 33**). While the ether treated sample shows a high concentration of defects in the graphitic lattice between 5 and 20 μm in diameter ("holey" NrGO), as we have reported previously (Sci Advances paper). The pyridine treated sample shows the roughest surface (largest value of average surface roughness R_a=49.3 calculated using digital image processing[156]) amongst all samples (R_a for water and diethyl ether samples are 29.5 and 37.7, respectively), with extremely small wrinkles that cover the surface completely. Porosity calculated from images shows that diethyl-

ether treated sample has highest porosity of 14-20%, while much smaller porosity was obtained for pyridine and water-treated samples (4-7% and 1-2% respectively).
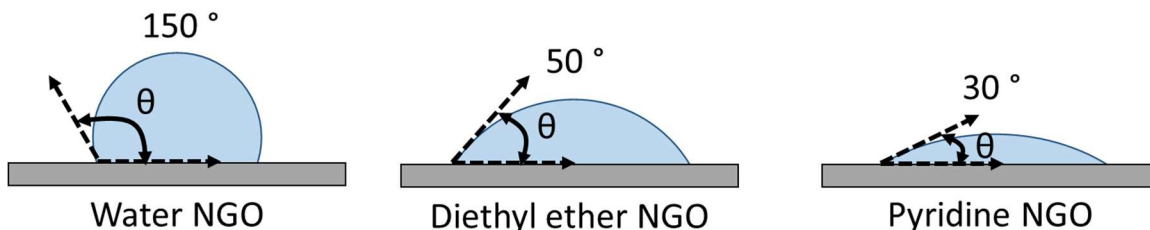
Figure 34: Schematic of the wettability of the different solvent treated NrGO catalysts.

The porosity and surface roughness can affect the wetness characteristics of the samples, which are crucial for optimizing the ORR reaction. Therefore, the impact of these morphological features on the interaction was studied using contact angle measurements (schematic **Figure 34**). The contact angle between water and a NrGO substrate was measured for the water, diethyl ether and pyridine treated samples. The contact angles with water were 150, 50 and 30 degrees, respectively, indicating that wetting characteristics are enhanced with solvent treatment. Thus, the pyridine treatment appears to allow for a triple phase boundary, (electrolyte, catalyst and gas phase reactants) ideal for ORR.
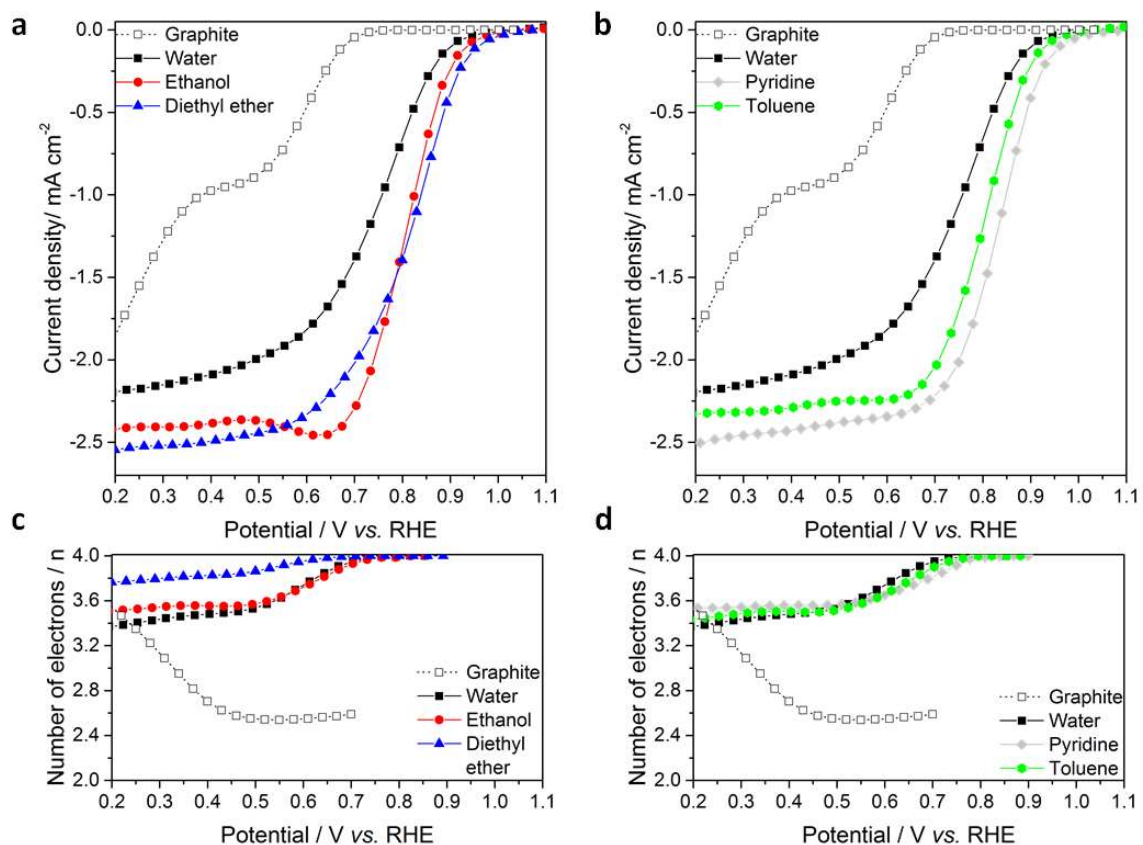
Figure 35: Electrocatalytic performance and selectivity of solvent-treated nitrogen-doped GO catalysts for the oxygen reduction reaction. (a) ORR activity and selectivity of NrGO catalysts treated with non-cyclic solvents. (b) ORR activity and selectivity of NrGO catalysts treated with cyclic solvents; NrGO-water and graphite data is added for comparison purposes.

The electrocatalytic ORR activity and selectivity of the NrGO electrocatalysts was measured using a rotating-ring disc electrode (RRDE) in O_2-saturated 0.1 M NaOH electrolyte (**Figure 35**). Selectivity of the ORR was determined according to **Equation (9)**:

$$n = 4 * \frac{i_d}{i_d + \frac{i_r}{N}} \qquad (9)$$

A four-electron selectivity refers to the selectivity of the reaction to produce four hydroxide ions according to **Equation (5)**. Additionally, an undesired alternate reaction that could also occur is the partial reduction of oxygen to a hydroperoxyl radical, shown in **Equation (6)**. The ORR performance of a catalyst is defined by its activity and its selectivity towards the four-electron reduction of oxygen, and, more importantly, by its half-wave potential ($E_{1/2}$), which is a descriptor of the limiting current density and onset potential (E_{onset}) of the catalyst, i.e., the potential at which the catalyzed ORR current starts to appear. The thermodynamic reversible potential ($E°$) of oxygen reduction at 25°C is 1.23 V versus the reversible hydrogen electrode (RHE). Any additional potential required to drive the ORR is called the overpotential (η). High-performing ORR catalysts are characterized by low η, high $E_{1/2}$, high selectivity values for four-electron transfer and high limiting current. As a reference, graphite shows an E_{onset} of 0.79 V *vs.* RHE while it does not show a limiting current for the four-electron reaction and therefore no $E_{1/2}$, due to a low concentration of active sites. The observed ORR activity and selectivity for the NrGO electrocatalysts varied depending on the solvent used to treat the graphene oxide precursor prior to N-doping. Lower performance and selectivity was observed from the water-treated NrGO with an E_{onset} of 1.01 V *vs.* RHE and an $E_{1/2}$ of 0.77 V *vs.* RHE. A similar onset potential was obtained from 1.01-1.08 V regardless of the solvent used revealing only a slight improvement in the reduction of η. However, there was a significant shift towards a more positive $E_{1/2}$ revealing an improvement of the activity of the catalyst. In the case of non-cyclic solvents, ethanol or ether treated NrGO shifted $E_{1/2}$ to 0.81 V *vs.* RHE. In the case of cyclic

solvents, the toluene treated NrGO shifted $E_{1/2}$ to 0.80 V *vs.* RHE while the pyridine treated NrGO exhibited the highest ORR activity with an $E_{1/2}$ of 0.84 V *vs.* RHE. The current generated from the oxidation of HO_2^- was also recorded during the ORR polarization curves and converted to number of electrons as shown in **Equation (9)**.

All the samples showed a combination of 2 and 4 electron reactions, with water showing n=3.3 at 0.5 V *vs.* RHE. Ethanol, diethyl ether, pyridine and toluene show n=3.5, 3.8, 3.5 and 3.4 at 0.5 V *vs.* RHE, respectively. Based on these results, diethyl ether and pyridine treated samples showed the highest selectivity and performance in alkaline electrolyte. For comparison (**Figure 35**), graphite shows respectively n=2.5 while platinum reportedly reduces oxygen *via* a four-electron[6] transfer reaction. Therefore, it is evident that solvent-treatment prior to nitrogen doping has a drastic effect on catalytic activity and more importantly leads to an increased number of electron transfer sites as indicated by the selectivity data.

Stability and durability are other important consideration for a catalyst, and studies were conducted in N_2 saturated media by cycling the catalyst 10,000 times from 0.6 to 1.0 V at 100 mV/s. Surprisingly, after 10,000 cycles, the ORR performance of the most active electrocatalyst (NrGO-pyridine) showed only a 20 mV decrease in half-wave potential (**Figure 36 A**) with an improved selectivity of the catalyst from a mixed reaction (n=3.4) at 0.5 V to a near four-electron reaction (**Figure 36 B**) . The limiting current stayed constant with a value of 2.5 mA cm^{-2}. In order to confirm the results observed from RRDE experiments, Koutecky-Levitch

plots were derived before and after cycling. These results confirm the transition from a mixed reaction to a highly selective four-electron reaction (**Figure 36 C-D**).
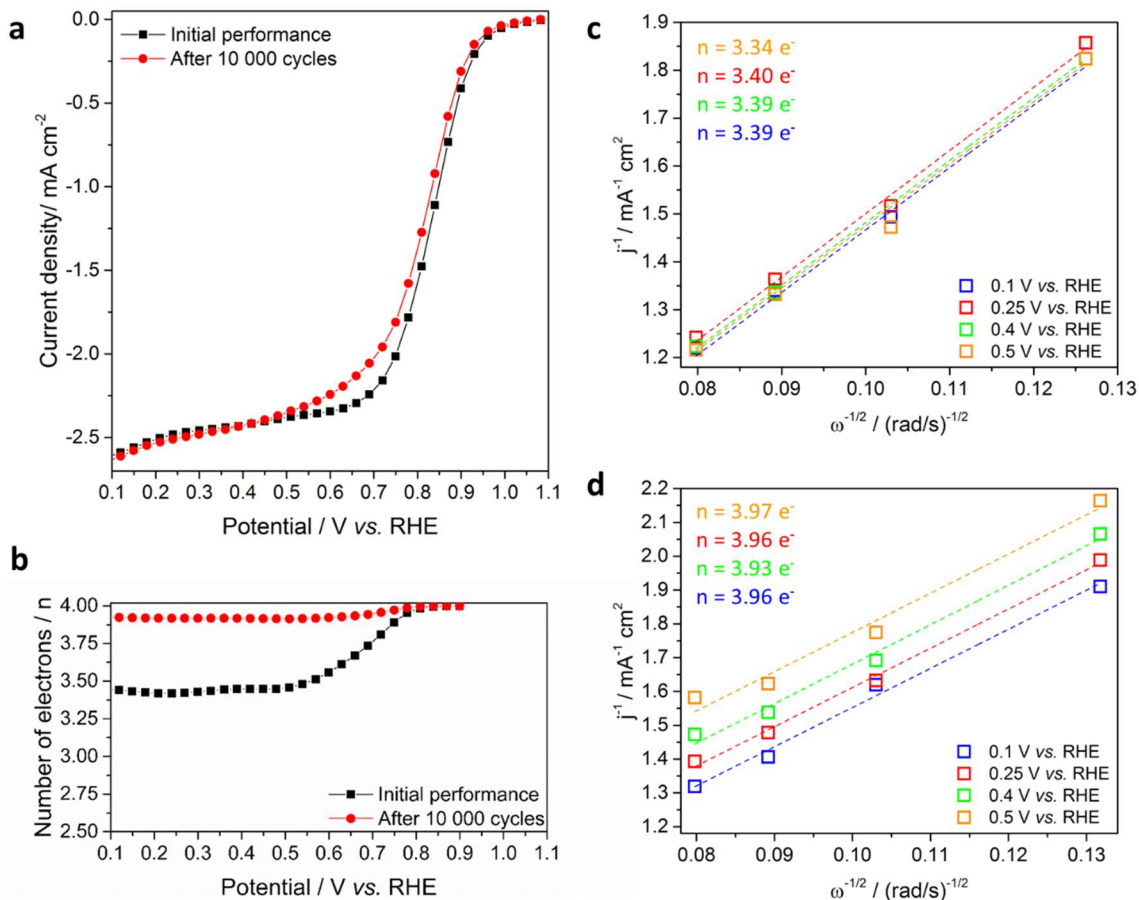
Figure 36: Selectivity, durability and kinetic activity of NrGO derived from pyridine rinsed GO. (a) RRDE measurement of ORR activity before and after 10,000 cycles in N_2. (b) Peroxide yield (in terms of number of electrons) before and after 10,000 cycles. (c) Koutecky-Levitch plot before cycling. (d) Koutecky-Levitch plot after cycling.

As mentioned previously, the ORR activity shown in **Figure 35 and 36 A** reveals an initial mixed mechanism of n=3.4 electrons per molecule of oxygen. This initial performance is the combination of different active sites, promoting either a 2 or a four-electron reaction. As we cycle the catalyst in a reductive environment, the mechanism shifts towards a more selective four-electron process despite a

minimal half-wave potential decrease and no limiting current change. This data

suggests that the reduction of oxygen initially occurs via two two-electron

reactions. Furthermore, the question arises that the cycling of the electrocatalysts

either destroys sites promoting the first reaction leading to peroxide radicals being

formed as shown in **Equation (6)** or unveils more active sites dedicated to the

reduction of peroxide radicals into hydroxides shown in **Equation (7)**.
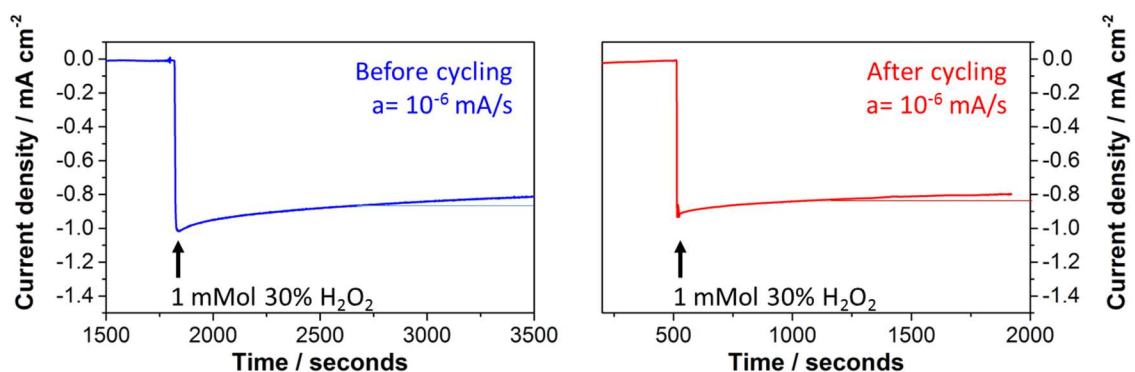
Figure 37: Chronoamperometry of the pyridine-treated NrGO catalyst before and after cycling, in a N_2 saturated solution of 0.1 M NaOH after injection of 1 mMol of 30% H_2O_2 solution.

To understand, which mechanism is responsible for a more selective catalyst,

chronoamperometry was performed while peroxide radicals were introduced in the

electrolyte. The reduction of these radicals into OH$^-$ by the catalysts is shown in

Figure 37 and clearly indicates that a reduction current appearing as 1 mMol of

peroxide radicals is being introduced in the solution. Additionally, there is no

change in current density or in slope before and after cycling. This suggests that

the rate of decomposition of peroxide radicals remains the same and therefore that

cycling the catalyst would destroy peroxide-generating active sites (**Equation 6**)

rather than unveiling new peroxide-reducing active sites.

6.4. Conclusion

In summary, we have shown that exposing GO to various solvent treatments results in electrocatalysts with very different morphology after nitrogen doping in an ammonia environment at 850 °C. These resulting morphological differences lead to materials with different ORR activity exhibiting both 2+2 and 4 electron catalytic behavior. However, after cycling the NrGO electrocatalyst rinsed in pyridine in an RRDE experiment, we found that the material shifted its ORR behavior to a predominantly 4 electron reaction, *i.e.*, it became more selective, with little loss in overall performance. The cycling of the catalysts destroys active sites promoting the reduction of oxygen to peroxide radicals. Because this observation was only found in an alkaline medium (similar experiments is shown in acid, with no selectivity changes[87]), this suggest that the active sites in acid and alkaline are likely different and that electrocatalysts should each be tailored depending on the application. Finally, the treatment of other existing PGM-free systems with organic solvents could introduce morphological changes that could lead to more active, more selective and more durable catalysts for ORR.

7. <u>Conclusion and prospects</u>

In summary, the synthesis of model electrocatalysts for the ORR based on graphite has been demonstrated through three separate studies. The main objective was to use well- defined model systems based on graphitic systems such as graphite and graphene oxide. These extensively characterized materials are relatively simple to model, making them ideal platforms for understanding catalytic active sites.

In the first study, we demonstrate that a green, solvent-free and sustainable synthesis route to create active ORR electrocatalysts based on graphite is possible. The simple ball milling of expanded graphite in presence of metal and nitrogen precursors followed by a pyrolysis step leads to large amounts of an active and selective catalyst towards the ORR. However, further advances in catalytic performance could be obtainable by varying the nature of the M and N precursors miscibility, and creating smaller particle size.

In the second study, we demonstrate active nitrogen-doped graphene oxide catalysts for ORR in acidic conditions through the application of simple solvent drying strategies. These strategies facilitate the efficient removal of the trapped water within the graphitic sheets, which in turn allows for controlling the macroscopic structure and morphology of electrocatalysts upon nitrogen doping. The resulting materials have shown exceptional performance in acidic medium.

In the third study, we have shown that exposing GO to various solvent treatments results in electrocatalysts with very different morphologies after nitrogen doping in an ammonia environment at 850 °C. These resulting morphological differences

lead to materials with different ORR activity exhibiting both 2+2 and 4 electron catalytic behavior. However, after cycling the NrGO electrocatalyst in RRDE, we show that the material became more selective towards the ORR, with little loss in overall performance. The cycling of the catalysts destroys active sites promoting the reduction of oxygen to peroxide radicals. Because this observation was only found in an alkaline medium (similar experiments are shown in acid, with no selectivity changes [87]), this suggest that the active sites in acid and alkaline are likely different and that electrocatalysts should each be tailored depending on the application.

The work presented here allowed the synthesis of model electrocatalysts that mimic the existing PGM-free catalysts. These model systems enable the direct observation and correlation between M-N-C structure and catalytic performance. The thorough characterization of these materials provides useful information indispensable for the modelling of PGM-free electrocatalysts (i) the effects of structure and morphology on catalyst activity and durability; (ii) the interaction between active sites and the carbon matrix; and (iii) catalyst degradation mechanism. This work will create a solid foundation for next generation PGM-free systems. Future work comprises:

- Further improvement of the ORR performance of electrocatalysts synthesized via the green, solvent-free route by investigating alternative M and N precursors.
- The investigation of these graphite-based materials for other applications such as carbon supports for PGM catalysts or metal-air batteries.

- The treatment of other existing PGM-free systems with organic solvents could introduce morphological changes that could lead to more active, more selective and more durable catalysts for ORR.

- The use of the information gathered through these studies such as elemental composition, surface area or synthesis steps to identify the crucial steps needed to synthesis highly active, selective and durable ORR catalysts.

References

1.   O'hayre, R., et al., *Fuel cell fundamentals*. 2016: John Wiley & Sons.

2.   Gong, K., et al., *Nitrogen-Doped Carbon Nanotube Arrays with High Electrocatalytic Activity for Oxygen Reduction.* Science, 2009. **323**(5915): p. 760-764.

3.   Liang, Y., et al., *Co3O4 nanocrystals on graphene as a synergistic catalyst for oxygen reduction reaction.* Nat Mater, 2011. **10**(10): p. 780-786.

4.   Asazawa, K., et al., *A Platinum-Free Zero-Carbon-Emission Easy Fuelling Direct Hydrazine Fuel Cell for Vehicles.* Angewandte Chemie International Edition, 2007. **46**(42): p. 8024-8027.

5.   Martinez, U., et al., *Aerosol-derived Ni 1− x Zn x electrocatalysts for direct hydrazine fuel cells.* Physical Chemistry Chemical Physics, 2012. **14**(16): p. 5512-5517.

6.   Geniès, L., R. Faure, and R. Durand, *Electrochemical reduction of oxygen on platinum nanoparticles in alkaline media.* Electrochimica Acta, 1998. **44**(8–9): p. 1317-1327.

7.   Stephan, O., et al., *Doping Graphitic and Carbon Nanotube Structures with Boron and Nitrogen.* Science, 1994. **266**(5191): p. 1683-1685.

8.   Wang, H., T. Maiyalagan, and X. Wang, *Review on Recent Progress in Nitrogen-Doped Graphene: Synthesis, Characterization, and Its Potential Applications.* ACS Catalysis, 2012. **2**(5): p. 781-794.

9.   Ayala, P., et al., *The doping of carbon nanotubes with nitrogen and their potential applications.* Carbon, 2010. **48**(3): p. 575-586.

10.   Panchakarla, L.S., et al., *Synthesis, Structure, and Properties of Boron- and Nitrogen-Doped Graphene.* Advanced Materials, 2009. **21**(46): p. 4726-4730.

11.   Zheng, Y., et al., *Two-Step Boron and Nitrogen Doping in Graphene for Enhanced Synergistic Catalysis.* Angewandte Chemie International Edition, 2013. **52**(11): p. 3110-3116.

12.   Zhao, Y., et al., *Can Boron and Nitrogen Co-doping Improve Oxygen Reduction Reaction Activity of Carbon Nanotubes?* Journal of the American Chemical Society, 2013. **135**(4): p. 1201-1204.

13. Wei, W., et al., *Nitrogen-Doped Carbon Nanosheets with Size-Defined Mesopores as Highly Efficient Metal-Free Catalyst for the Oxygen Reduction Reaction.* Angewandte Chemie International Edition, 2014. **53**(6): p. 1570-1574.

14. Yang, L., et al., *Boron-Doped Carbon Nanotubes as Metal-Free Electrocatalysts for the Oxygen Reduction Reaction.* Angewandte Chemie International Edition, 2011. **50**(31): p. 7132-7135.

15. Choi, C.H., S.H. Park, and S.I. Woo, *Binary and Ternary Doping of Nitrogen, Boron, and Phosphorus into Carbon for Enhancing Electrochemical Oxygen Reduction Activity.* ACS Nano, 2012. **6**(8): p. 7084-7091.

16. Sun, X., et al., *Fluorine-Doped Carbon Blacks: Highly Efficient Metal-Free Electrocatalysts for Oxygen Reduction Reaction.* ACS Catalysis, 2013. **3**(8): p. 1726-1729.

17. Liu, Z.-W., et al., *Phosphorus-Doped Graphite Layers with High Electrocatalytic Activity for the O2 Reduction in an Alkaline Medium.* Angewandte Chemie International Edition, 2011. **50**(14): p. 3257-3261.

18. Lai, L., et al., *Exploration of the active center structure of nitrogen-doped graphene-based catalysts for oxygen reduction reaction.* Energy & Environmental Science, 2012. **5**(7): p. 7936-7942.

19. Yang, D.-S., et al., *Phosphorus-Doped Ordered Mesoporous Carbons with Different Lengths as Efficient Metal-Free Electrocatalysts for Oxygen Reduction Reaction in Alkaline Media.* Journal of the American Chemical Society, 2012. **134**(39): p. 16127-16130.

20. Meng, Y., et al., *N-, O-, and S-Tridoped Nanoporous Carbons as Selective Catalysts for Oxygen Reduction and Alcohol Oxidation Reactions.* Journal of the American Chemical Society, 2014. **136**(39): p. 13554-13557.

21. Ma, Z., et al., *Sulfur-Doped Graphene Derived from Cycled Lithium–Sulfur Batteries as a Metal-Free Electrocatalyst for the Oxygen Reduction Reaction.* Angewandte Chemie International Edition, 2015. **54**(6): p. 1888-1892.

22. Jaouen, F., et al., *Recent advances in non-precious metal catalysis for oxygen-reduction reaction in polymer electrolyte fuel cells.* Energy Environ. Sci., 2011. **4**(1): p. 114-130.

23. Jaouen, F., et al., *Cross-laboratory experimental study of non-noble-metal electrocatalysts for the oxygen reduction reaction.* ACS applied materials & interfaces, 2009. **1**(8): p. 1623-1639.

24. Gasteiger, H.A. and N.M. Marković, *Just a Dream—or Future Reality?* Science, 2009. **324**(5923): p. 48-49.

25. Wang, B., *Recent development of non-platinum catalysts for oxygen reduction reaction.* Journal of Power Sources, 2005. **152**: p. 1-15.

26. Wu, G., et al., *High-performance electrocatalysts for oxygen reduction derived from polyaniline, iron, and cobalt.* Science, 2011. **332**(6028): p. 443-447.

27. Proietti, E., et al., *Iron-based cathode catalyst with enhanced power density in polymer electrolyte membrane fuel cells.* Nature communications, 2011. **2**: p. 416.

28. Garsuch, A., et al., *Time to move beyond transition metal — N — C catalysts for oxygen reduction*, in *Handbook of Fuel Cells*. 2010, John Wiley & Sons, Ltd.

29. Ranjbar Sahraie, N., et al., *Noble-Metal-Free Electrocatalysts with Enhanced ORR Performance by Task-Specific Functionalization of Carbon using Ionic Liquid Precursor Systems.* Journal of the American Chemical Society, 2014. **136**(41): p. 14486-14497.

30. Lee, J.-S., et al., *A Highly Efficient Electrocatalyst for the Oxygen Reduction Reaction: N-Doped Ketjenblack Incorporated into Fe/Fe3C-Functionalized Melamine Foam.* Angewandte Chemie International Edition, 2013. **52**(3): p. 1026-1030.

31. Tylus, U., et al., *Elucidating oxygen reduction active sites in pyrolyzed metal–nitrogen coordinated non-precious-metal electrocatalyst systems.* The Journal of Physical Chemistry C, 2014. **118**(17): p. 8999-9008.

32. Gupta, S., et al., *Heat-treated polyacrylonitrile-based catalysts for oxygen electroreduction.* Journal of Applied Electrochemistry, 1989. **19**(1): p. 19-27.

33. Lalande, G., et al., *Is nitrogen important in the formulation of Fe-based catalysts for oxygen reduction in solid polymer fuel cells?* Electrochimica Acta, 1997. **42**(9): p. 1379-1388.

34. Kobayashi, M., et al., *Role of residual transition-metal atoms in oxygen reduction reaction in cobalt phthalocyanine-based carbon cathode catalysts for polymer electrolyte fuel cell.* Journal of Power Sources, 2011. **196**(20): p. 8346-8351.

35. Kobayashi, M., et al., *Indirect contribution of transition metal towards oxygen reduction reaction activity in iron phthalocyanine-based carbon*

catalysts for polymer electrolyte fuel cells. Electrochimica Acta, 2012. **74**: p. 254-259.

36.   Pierson, H.O., *Handbook of carbon, graphite, diamonds and fullerenes: processing, properties and applications*. 2012: William Andrew.

37.   Geim, A.K. and K.S. Novoselov, *The rise of graphene.* Nature materials, 2007. **6**(3): p. 183-191.

38.   Lee, C., et al., *Measurement of the elastic properties and intrinsic strength of monolayer graphene.* science, 2008. **321**(5887): p. 385-388.

39.   Wissler, M., *Graphite and carbon powders for electrochemical applications.* Journal of power sources, 2006. **156**(2): p. 142-150.

40.   Inc., F.G. *Graphite 101*.   [cited 2017 4/29/2017]; Available from: http://www.focusgraphite.com/technology/.

41.   Allen, M.J., V.C. Tung, and R.B. Kaner, *Honeycomb carbon: a review of graphene.* Chemical reviews, 2009. **110**(1): p. 132-145.

42.   Hummers, W.S. and R.E. Offeman, *Preparation of Graphitic Oxide.* Journal of the American Chemical Society, 1958. **80**(6): p. 1339-1339.

43.   Dimiev, A., et al., *Pristine graphite oxide.* Journal of the American Chemical Society, 2012. **134**(5): p. 2815-2822.

44.   Schniepp, H.C., et al., *Functionalized single graphene sheets derived from splitting graphite oxide.* The Journal of Physical Chemistry B, 2006. **110**(17): p. 8535-8539.

45.   McAllister, M.J., et al., *Single sheet functionalized graphene by oxidation and thermal expansion of graphite.* Chemistry of materials, 2007. **19**(18): p. 4396-4404.

46.   Park, S. and R.S. Ruoff, *Chemical methods for the production of graphenes.* Nature nanotechnology, 2009. **4**(4): p. 217-224.

47.   Loh, K.P., et al., *The chemistry of graphene.* Journal of Materials Chemistry, 2010. **20**(12): p. 2277-2289.

48.   Dreyer, D.R., et al., *The chemistry of graphene oxide.* Chemical Society Reviews, 2010. **39**(1): p. 228-240.

49.   Paredes, J., et al., *Graphene oxide dispersions in organic solvents.* Langmuir, 2008. **24**(19): p. 10560-10564.

50. Park, S., et al., *Colloidal suspensions of highly reduced graphene oxide in a wide variety of organic solvents.* Nano letters, 2009. **9**(4): p. 1593-1597.

51. Cerveny, S., et al., *Dynamics of water intercalated in graphite oxide.* The Journal of Physical Chemistry C, 2010. **114**(6): p. 2604-2612.

52. Acik, M., et al., *The role of intercalated water in multilayered graphene oxide.* Acs Nano, 2010. **4**(10): p. 5861-5868.

53. Ambrosi, A., et al., *Chemically reduced graphene contains inherent metallic impurities present in parent natural and synthetic graphite.* Proceedings of the National Academy of Sciences, 2012. **109**(32): p. 12899-12904.

54. Stankovich, S., et al., *Synthesis of graphene-based nanosheets via chemical reduction of exfoliated graphite oxide.* carbon, 2007. **45**(7): p. 1558-1565.

55. Chen, W., L. Yan, and P.R. Bangal, *Preparation of graphene by the rapid and mild thermal reduction of graphene oxide induced by microwaves.* Carbon, 2010. **48**(4): p. 1146-1152.

56. Kumar, P.V., et al., *Scalable enhancement of graphene oxide properties by thermally driven phase transformation.* Nature chemistry, 2014. **6**(2): p. 151-158.

57. Gong, C., et al., *Graphitization of graphene oxide with ethanol during thermal reduction.* The Journal of Physical Chemistry C, 2012. **116**(18): p. 9969-9979.

58. Domínguez, C., et al., *Effect of the pyrolysis atmosphere and nature of iron precursor on the structure and activity of Fe/N based electrocatalysts for the oxygen reduction reaction.* International Journal of Hydrogen Energy, 2016.

59. Geng, D., et al., *High oxygen-reduction activity and durability of nitrogen-doped graphene.* Energy & Environmental Science, 2011. **4**(3): p. 760-764.

60. Lin, Z., et al., *Facile synthesis of nitrogen-doped graphene via pyrolysis of graphene oxide and urea, and its electrocatalytic activity toward the oxygen-reduction reaction.* Advanced Energy Materials, 2012. **2**(7): p. 884-888.

61. Stankovich, S., et al., *Synthesis and exfoliation of isocyanate-treated graphene oxide nanoplatelets.* Carbon, 2006. **44**(15): p. 3342-3347.

62. Janowska, I., et al., *Microwave synthesis of large few-layer graphene sheets in aqueous solution of ammonia.* Nano Research, 2010. **3**(2): p. 126-137.

63. Li, D., et al., *Synthesis of nitrogen doped graphene from graphene oxide within an ammonia flame for high performance supercapacitors.* RSC Advances, 2014. **4**(98): p. 55394-55399.

64. BAG, S. and C.R. RAJ, *On the electrocatalytic activity of nitrogen-doped reduced graphene Oxide: Does the nature of nitrogen really control the activity towards oxygen reduction?* Journal of Chemical Sciences, 2016. **128**(3): p. 339-347.

65. Murray, J. and A. Ubbelohde. *Electronic properties of some synthetic metals derived from graphite*. in *Proceedings of the Royal Society of London A: Mathematical, Physical and Engineering Sciences*. 1969. The Royal Society.

66. Ubbelohde, A., *Anisotropy of synthetic metals.* Nature, 1971. **232**(5305): p. 43-44.

67. Jegoudez, J., C. Mazieres, and R. Setton, *Behaviour of the binary graphite intercalation compounds KC8 and KC24 towards a set of sample organic molecules.* Synthetic Metals, 1983. **7**(1-2): p. 85-91.

68. Inagaki, M., *Applications of graphite intercalation compounds.* Journal of Materials Research, 1989. **4**(06): p. 1560-1568.

69. Dresselhaus, M.S. and G. Dresselhaus, *Intercalation compounds of graphite.* Advances in physics, 2002. **51**(1): p. 1-186.

70. Enoki, T., M. Suzuki, and M. Endo, *Graphite intercalation compounds and applications*. 2003: Oxford University Press.

71. Besenhard, J., et al., *Electrochemical applications of graphite intercalation compounds.* Synthetic Metals, 1982. **4**(3): p. 211-223.

72. Boukhvalov, D.W. and Y.-W. Son, *Oxygen reduction reactions on pure and nitrogen-doped graphene: a first-principles modeling.* Nanoscale, 2012. **4**(2): p. 417-420.

73. Holby, E.F., et al., *Metropolis Monte Carlo search for non-precious metal catalyst active site candidates.* ECS Transactions, 2013. **50**(2): p. 1839-1845.

74. Jia, Q., et al., *Experimental Observation of Redox-Induced Fe–N Switching Behavior as a Determinant Role for Oxygen Reduction Activity.* ACS Nano, 2015. **9**(12): p. 12496-12505.

75. Holby, E. and C. Taylor, *Control of graphene nanoribbon vacancies by Fe and N dopants: Implications for catalysis.* Applied Physics Letters, 2012. **101**(6): p. 064102.

76.   Holby, E.F., et al., *Structure of Fe–Nx–C Defects in Oxygen Reduction Reaction Catalysts from First-Principles Modeling.* The Journal of Physical Chemistry C, 2014. **118**(26): p. 14388-14393.

77.   Atanassov, P., et al. *Non-Platinum Group Metal Catalysts for Oxygen Reduction in Fuel Cell Applictaions*. in *Meeting Abstracts*. 2015. The Electrochemical Society.

78.   Holby, E.F. and C.D. Taylor, *Activity of N-coordinated multi-metal-atom active site structures for Pt-free oxygen reduction reaction catalysis: Role of *OH ligands.* Scientific Reports, 2015. **5**: p. 9286.

79.   Chen, L., et al., *Lattice Boltzmann Pore-Scale Investigation of Coupled Physical-electrochemical Processes in C/Pt and Non-Precious Metal Cathode Catalyst Layers in Proton Exchange Membrane Fuel Cells.* Electrochimica Acta, 2015. **158**: p. 175-186.

80.   Artyushkova, K., et al. *Integrating Non-Platinum Group Metal Catalysts into Membrane Electrode Assemblies: Chemical Interactions and Morphology of the Catalytic Layer*. in *Meeting Abstracts*. 2015. The Electrochemical Society.

81.   Jafri, R.I., N. Rajalakshmi, and S. Ramaprabhu, *Nitrogen doped graphene nanoplatelets as catalyst support for oxygen reduction reaction in proton exchange membrane fuel cell.* Journal of Materials Chemistry, 2010. **20**(34): p. 7114-7117.

82.   Lee, K.R., et al., *Electrochemical oxygen reduction on nitrogen doped graphene sheets in acid media.* Electrochemistry Communications, 2010. **12**(8): p. 1052-1055.

83.   Ozaki, J.-i., et al., *Preparation and oxygen reduction activity of BN-doped carbons.* Carbon, 2007. **45**(9): p. 1847-1853.

84.   Qu, L., et al., *Nitrogen-doped graphene as efficient metal-free electrocatalyst for oxygen reduction in fuel cells.* ACS nano, 2010. **4**(3): p. 1321-1326.

85.   Shao, Y., et al., *Nitrogen-doped graphene and its electrochemical applications.* Journal of Materials Chemistry, 2010. **20**(35): p. 7491-7496.

86.   Sheng, Z.-H., et al., *Catalyst-free synthesis of nitrogen-doped graphene via thermal annealing graphite oxide with melamine and its excellent electrocatalysis.* ACS nano, 2011. **5**(6): p. 4350-4358.

87.   Martinez, U., et al., *Critical role of intercalated water for electrocatalytically active nitrogen-doped graphitic systems.* Science Advances, 2016. **2**(3).

88.   Dimiev, A.M., et al., *Direct real-time monitoring of stage transitions in graphite intercalation compounds.* ACS nano, 2013. **7**(3): p. 2773-2780.

89.   Zhao, W., et al., *Intercalation of few-layer graphite flakes with FeCl3: Raman determination of Fermi level, layer by layer decoupling, and stability.* Journal of the American Chemical Society, 2011. **133**(15): p. 5941-5946.

90.   Bashyam, R. and P. Zelenay, *A class of non-precious metal composite catalysts for fuel cells.* Nature, 2006. **443**(7107): p. 63-66.

91.   Chung, H.T., et al., *Cyanamide-derived non-precious metal catalyst for oxygen reduction.* Electrochemistry Communications, 2010. **12**(12): p. 1792-1795.

92.   Wu, G., et al., *Synthesis–structure–performance correlation for polyaniline–Me–C non-precious metal cathode catalysts for oxygen reduction in fuel cells.* Journal of Materials Chemistry, 2011. **21**(30): p. 11392-11405.

93.   Cao, R., et al., *Recent progress in non‑precious catalysts for metal‑air batteries.* Advanced Energy Materials, 2012. **2**(7): p. 816-829.

94.   Wu, G., et al., *Titanium dioxide-supported non-precious metal oxygen reduction electrocatalyst.* Chemical Communications, 2010. **46**(40): p. 7489-7491.

95.   Kotov, N.A., I. Dékány, and J.H. Fendler, *Ultrathin graphite oxide–polyelectrolyte composites prepared by self-assembly: Transition between conductive and non-conductive states.* Advanced Materials, 1996. **8**(8): p. 637-641.

96.   Marcano, D.C., et al., *Improved Synthesis of Graphene Oxide.* ACS Nano, 2010. **4**(8): p. 4806-4814.

97.   Lefrou, C., P. Fabry, and J.-C. Poignet, *Electrochemistry: the basics, with examples*. 2012: Springer Science & Business Media.

98.   Hou, J., et al., *Graphene-based electrochemical energy conversion and storage: fuel cells, supercapacitors and lithium ion batteries.* Physical Chemistry Chemical Physics, 2011. **13**(34): p. 15384-15402.

99.   Pumera, M., *Graphene-based nanomaterials for energy storage.* Energy & Environmental Science, 2011. **4**(3): p. 668-674.

100.   Bonaccorso, F., et al., *Graphene, related two-dimensional crystals, and hybrid systems for energy conversion and storage.* Science, 2015. **347**(6217): p. 1246501.

101. Raccichini, R., et al., *The role of graphene for electrochemical energy storage.* Nature materials, 2015. **14**(3): p. 271-279.

102. Chen, Z., et al., *A review on non-precious metal electrocatalysts for PEM fuel cells.* Energy & Environmental Science, 2011. **4**(9): p. 3167-3192.

103. Kramm, U.I., et al., *Structure of the catalytic sites in Fe/N/C-catalysts for O 2-reduction in PEM fuel cells.* Physical Chemistry Chemical Physics, 2012. **14**(33): p. 11673-11688.

104. Othman, R., A.L. Dicks, and Z. Zhu, *Non precious metal catalysts for the PEM fuel cell cathode.* International journal of hydrogen energy, 2012. **37**(1): p. 357-372.

105. Serov, A., K. Artyushkova, and P. Atanassov, *Fe-N-C Oxygen Reduction Fuel Cell Catalyst Derived from Carbendazim: Synthesis, Structure, and Reactivity.* Advanced Energy Materials, 2014. **4**(10).

106. Serov, A., et al., *Templated non-PGM cathode catalysts derived from iron and poly (ethyleneimine) precursors.* Applied Catalysis B: Environmental, 2012. **127**: p. 300-306.

107. Serov, A., et al., *Highly active and durable templated non-PGM cathode catalysts derived from iron and aminoantipyrine.* Electrochemistry Communications, 2012. **22**: p. 53-56.

108. Trogadas, P., T.F. Fuller, and P. Strasser, *Carbon as catalyst and support for electrochemical energy conversion.* Carbon, 2014. **75**: p. 5-42.

109. Shui, J., et al., *Highly efficient nonprecious metal catalyst prepared with metal–organic framework in a continuous carbon nanofibrous network.* Proceedings of the National Academy of Sciences of the United States of America, 2015. **112**(34): p. 10629-10634.

110. Ma, S., et al., *Cobalt Imidazolate Framework as Precursor for Oxygen Reduction Reaction Electrocatalysts.* Chemistry – A European Journal, 2011. **17**(7): p. 2063-2067.

111. Yuan, S., et al., *A Highly Active and Support-Free Oxygen Reduction Catalyst Prepared from Ultrahigh-Surface-Area Porous Polyporphyrin.* Angewandte Chemie International Edition, 2013. **52**(32): p. 8349-8353.

112. Langmi, H.W., J. Ren, and N.M. Musyoka, *Metal-Organic Frameworks as Materials for Fuel Cell Technologies*, in *Nanomaterials for Fuel Cell Catalysis*. 2016, Cham : Springer International Publishing : Springer. p. 367-407.

113. Bonaccorso, F., et al., *Graphene, related two-dimensional crystals, and hybrid systems for energy conversion and storage.* Science, 2015. **347**(6217).

114. Li, Y., et al., *An oxygen reduction electrocatalyst based on carbon nanotube-graphene complexes.* Nature nanotechnology, 2012. **7**(6): p. 394-400.

115. Wu, G., et al., *A carbon-nanotube-supported graphene-rich non-precious metal oxygen reduction catalyst with enhanced performance durability.* Chemical Communications, 2013. **49**(32): p. 3291-3.

116. Huang, X., et al., *Graphene-based composites.* Chemical Society Reviews, 2012. **41**(2): p. 666-686.

117. Machado, B.F. and P. Serp, *Graphene-based materials for catalysis.* Catalysis Science & Technology, 2012. **2**(1): p. 54-54.

118. Gasteiger, H.a., et al., *Activity benchmarks and requirements for Pt, Pt-alloy, and non-Pt oxygen reduction catalysts for PEMFCs.* Applied Catalysis B: Environmental, 2005. **56**(1-2): p. 9-35.

119. Wu, G., et al., *High-performance electrocatalysts for oxygen reduction derived from polyaniline, iron, and cobalt.* Science (New York, N.Y.), 2011. **332**(6028): p. 443-7.

120. Zhu, C., J. Zhai, and S. Dong, *Bifunctional fluorescent carbon nanodots: green synthesis via soy milk and application as metal-free electrocatalysts for oxygen reduction.* Chemical communications, 2012. **48**(75): p. 9367-9369.

121. Qi, X., et al., *FeCl 3 intercalated few-layer graphene for high lithium-ion storage performance.* Journal of Materials Chemistry A, 2015. **3**(30): p. 15498-15504.

122. Childres, I., et al., *Raman spectroscopy of graphene and related materials.* New developments in photon and materials research, 2013: p. 1-20.

123. Arabczyk, W. and J. Zamlynny, *Study of the ammonia decomposition over iron catalysts.* Catalysis letters, 1999. **60**(3): p. 167-171.

124. Ertl, G. and M. Huber, *Mechanism and kinetics of ammonia decomposition on iron.* Journal of Catalysis, 1980. **61**(2): p. 537-539.

125. Raccichini, R., et al., *The role of graphene for electrochemical energy storage.* Nat Mater, 2014. **advance online publication**.

126. Chen, D., L. Tang, and J. Li, *Graphene-based materials in electrochemistry.* Chemical Society Reviews, 2010. **39**(8): p. 3157-3180.

127. Jaouen, F., et al., *Recent advances in non-precious metal catalysis for oxygen-reduction reaction in polymer electrolyte fuel cells.* Energy & Environmental Science, 2011. **4**(1): p. 114-130.

128. Acik, M., et al., *The role of intercalated water in multilayered graphene oxide.* ACS Nano, 2010. **4**(10): p. 5861-8.

129. Dimiev, A., et al., *Pristine graphite oxide.* Journal of the American Chemical Society, 2012. **134**(5): p. 2815-22.

130. Martínez, L., et al., *PACKMOL: A package for building initial configurations for molecular dynamics simulations.* Journal of Computational Chemistry, 2009. **30**(13): p. 2157-2164.

131. Martínez, J.M. and L. Martínez, *Packing optimization for automated generation of complex system's initial configurations for molecular dynamics and docking.* Journal of Computational Chemistry, 2003. **24**(7): p. 819-825.

132. Cong, H.-P., J.-F. Chen, and S.-H. Yu, *Graphene-based macroscopic assemblies and architectures: an emerging material system.* Chemical Society Reviews, 2014. **43**(21): p. 7295-7325.

133. Chabot, V., et al., *A review of graphene and graphene oxide sponge: material synthesis and applications to energy and the environment.* Energy & Environmental Science, 2014. **7**: p. 1564-1564.

134. Cerveny, S., et al., *Dynamics of Water Intercalated in Graphite Oxide.* The Journal of Physical Chemistry C, 2010. **114**(6): p. 2604-2612.

135. Kumar, P.V., et al., *Scalable enhancement of graphene oxide properties by thermally driven phase transformation.* Nature chemistry, 2014. **6**(2): p. 151-8.

136. Gao, W., et al., *Ozonated Graphene Oxide Film as a Proton-Exchange Membrane.* Angewandte Chemie International Edition, 2014. **53**(14): p. 3588-3593.

137. Viculis, L.M., et al., *Intercalation and exfoliation routes to graphite nanoplatelets.* Journal of Materials Chemistry, 2005. **15**(9): p. 974-978.

138. Eigler, S., et al., *Formation and decomposition of CO2 intercalated graphene oxide.* Chemistry of Materials, 2012. **24**(7): p. 1276-1282.

139. Iglev, H. and M. Schmeisser, *Ultrafast IR spectroscopy of ice–water phase transition.* Journal of Molecular Liquids, 2010. **154**(1): p. 14-17.

140. Schmeisser, M., H. Iglev, and A. Laubereau, *Maximum superheating of bulk ice.* Chemical Physics Letters, 2007. **442**(4–6): p. 171-175.

141. Devlin, J.P. and V. Buch, *Ice Nanoparticles and Ice Adsorbate Interactions: FTIR Spectroscopy and Computer Simulations*, in *Water in Confining Geometries*, V. Buch and J.P. Devlin, Editors. 2003, Springer Berlin Heidelberg. p. 425-462.

142. Buch, V. and J.P. Devlin, *Water in confining geometries*. 2013: Springer Science & Business Media.

143. Liu, L., et al., *ReaxFF-lg: Correction of the ReaxFF Reactive Force Field for London Dispersion, with Applications to the Equations of State for Energetic Materials.* The Journal of Physical Chemistry A, 2011. **115**(40): p. 11016-11022.

144. Medhekar, N.V., et al., *Hydrogen bond networks in graphene oxide composite paper: structure and mechanical properties.* ACS Nano, 2010. **4**(4): p. 2300-6.

145. Pandey, D.K., et al., *Folding and cracking of graphene oxide sheets upon deposition.* Surface Science, 2011. **605**(17–18): p. 1669-1675.

146. Eigler, S., et al., *Formation and Decomposition of CO2 Intercalated Graphene Oxide.* Chemistry of Materials, 2012. **24**(7): p. 1276-1282.

147. Ambrosi, A., et al., *Chemically reduced graphene contains inherent metallic impurities present in parent natural and synthetic graphite.* Proceedings of the National Academy of Sciences of the United States of America, 2012. **109**(32): p. 12899-904.

148. Gasteiger, H.A., et al., *Activity benchmarks and requirements for Pt, Pt-alloy, and non-Pt oxygen reduction catalysts for PEMFCs.* Applied Catalysis B: Environmental, 2005. **56**(1): p. 9-35.

149. Merle, G., M. Wessling, and K. Nijmeijer, *Anion exchange membranes for alkaline fuel cells: A review.* Journal of Membrane Science, 2011. **377**(1): p. 1-35.

150. Varcoe, J.R. and R.C. Slade, *Prospects for alkaline anion-exchange membranes in low temperature fuel cells.* Fuel cells, 2005. **5**(2): p. 187-200.

151. Kinumoto, T., et al., *Durability of perfluorinated ionomer membrane against hydrogen peroxide.* Journal of Power Sources, 2006. **158**(2): p. 1222-1228.

152. Jia, Q., et al., *Spectroscopic insights into the nature of active sites in iron–nitrogen–carbon electrocatalysts for oxygen reduction in acid.* Nano Energy, 2016. **29**: p. 65-82.

153. Some, S., et al., *High-Quality Reduced Graphene Oxide by a Dual-Function Chemical Reduction and Healing Process.* Scientific Reports, 2013. **3**: p. 1929.

154. Eda, G., G. Fanchini, and M. Chhowalla, *Large-area ultrathin films of reduced graphene oxide as a transparent and flexible electronic material.* Nature Nanotechnology, 2008. **3**(5): p. 270-4.

155. Yang, H., et al., *Comparison of surface-enhanced Raman scattering on graphene oxide, reduced graphene oxide and graphene surfaces.* Carbon, 2013. **62**: p. 422-429.

156. Artyushkova, K. and J.E. Fulghum, *Angle resolved imaging of polymer blend systems: From images to a 3D volume of material morphology.* Journal of Electron Spectroscopy and Related Phenomena, 2005. **149**(1–3): p. 51-60.

Los Alamos Unlimited Release

LA-UR-17-25969